University of Alberta

North Atlantic Finite Element Ocean Modeling

by

Praveen Veluthedathekuzhiyil

A thesis submitted to the Faculty of Graduate Studies and Research in partial fulfillment of the requirements for the degree of

Doctor of Philosophy

Department of Earth and Atmospheric Sciences

To my father

Abstract

This thesis presents a modified version of the Finite Element Ocean Model (FEOM) developed at Alfred Wegener Institute for Polar and Marine Research (AWI) for the North Atlantic Ocean. A reasonable North Atlantic Ocean simulation is obtained against the observational data sets in a Control simulation (CS) where the surface boundary conditions are relaxed to a climatology. The vertical mixing in the model was tuned to represent convection in the model, also the horizontal mixing and diffusion coefficients to represent the changes in the resolution of the model's unstructured grid. In addition, the open boundaries in the model are treated with a sponge layer where tracers are relaxed to climatology.

The model is then further modified to accept the atmospheric flux forcing at the surface boundary with an added net heat flux correction and freshwater forcing from major rivers that are flowing into the North Atlantic Ocean. The impact of this boundary condition on the simulation results is then analyzed and shows many improvements albeit the drift in tracer properties around the Gulf Stream region remains as that of the CS case. However a comparison of the vertical sections at Cape Desolation and Cape Farewell with the available observational data sets shows many improvements in this simulation compared to that of the CS case. But the freshwater content in the Labrador Sea interior shows a continued drift as that of the CS case with an improvement towards the 10^{th} model year. A detailed analysis of the boundary currents around the Labrador Sea shows the weak offshore transport of freshwater from the West Greenland Current (WGC) as one of the causes.

To further improve the model and reasonably represent the boundary currents and associated sub-grid scale eddies in the model, a modified sub-grid

scale parameterization based on Gent and McWilliams, (1990) is adopted. The sensitivity of using various approaches in the thickness diffusion parameter (K_{gm}) for this parameterization scheme is studied. This includes the use of a constant as well as a spatially varying K_{gm} and both spatially and temporally varying K_{gm} that mimics the baroclinicity of the region of interest. The final approach was able to produce a reasonable North Atlantic Ocean simulation with less drift in the freshwater content of the Labrador Sea interior compared to all the previous simulations. The results are also compared with the observational data sets.

Even though few previous studies using an idealized Labrador Sea (Spall, 2004 and Katsman *et al.,* 2004) were able to show the role of seasonal eddy transport of tracer properties into the Labrador Sea interior in setting the convection depth in the region, realistic basin scale modelling of this was still lacking. However the detailed analysis of the boundary currents in this model of the subpolar gyre were able to show the role of the boundary currents and associated eddies in transporting tracer properties across into the Labrador Sea interior and their seasonal variability in setting the convection, preconditioning and restratification phases of the Labrador Sea interior.

Acknowledgements

I am deeply indebted to my supervisor Paul G. Myers for the valuable supervision to improve my research goal as well as giving me the full freedom to do the research.

I would like to thank my supervisory committee members Andrew BG Bush and John D Wilson for the valuable suggestions through time.

Thanks to Sergey Danilov of Alfred Wegener Institute for Polar and Marine Research (AWI) for providing me the model code and Sven Harig for the initial help in debugging and compiling the model on WestGrid SGI workstation.

I would like to extend my gratitude to the University of Alberta for providing me the funding for my research through teaching assistantships and bursaries. Also to the support of Institute for Geophysical Research (IGR) at University of Alberta for providing me the travel award to present my research updates on Canadian Meteorological and Oceanic Society (CMOS) conference.

Last but not the least, I would like to thank all my colleagues especially Xianmin Hu, Qiang Wang, Laura Castro and Arjen Terwisscha van Scheltinga for their support in various occasions of my research.

Other financial support available to my supervisor Paul G. Myers through National Science and Engineering Research Council of Canada (NSERC) and Mathematics of Information Technology and Complex Systems (MITACS) were also assisting my funding.

Table of Contents

List of Tables

List of Figures

List of Symbols and Abbreviations

ϵ	Emissivity coefficient
ζ	Sea surface elevation
θ	Potential temperature in ^oC
λ	Longitude
ρ	Insitu density of the sea water in kg m^{-3}
ρ_a	Air density in kg m^{-3}
ρ_o	Mean density of the Sea water in kg m^{-3}
σ	Stefan-Boltzmann constant
σ_θ	Density anomaly $\rho - 1000$ in kg m^{-3}
$\vec{\tau}$	Wind stress tangent vector
ϕ	Latitude
Γ	Open boundary
Ω	Domain boundary
A_h	Horizontal mixing coefficient
A_v	Vertical mixing coefficient
c	First baroclinic wave speed
C	Model tracer
C_E	Bulk transfer coefficient for latent heat
C_g	Bottom drag coefficient
C_H	Bulk transfer coefficient for sensible heat
C_P	Specific heat at constant pressure for air
C_{PW}	Specific heat at constant pressure for water
C_r	Baroclinic wave speed

e_s	Water saturation pressure in Pa
f	Coriolis parameter
H	Local water depth
K_{gm}	Thickness diffusion coefficient for GM parameterization
K_h	Horizontal diffusion coefficient
K_v	Vertical diffusion coefficient
l	Baroclinic length scale
L	Latent heat of vaporization
mSv	milli Sverdrup = $1 \times 10^3 m^3 s^{-1}$
N	Brunt-Väisälä frequency
p	Pressure
PW	Petawatt = 10^{15} Watt
q^s_{clim}	Climatological saturated specific humidity of air
Q_{net}	Net heat flux
R_i	Local Richardson number
S	Salinity
S_{ref}	Reference salinity
S_x, S_y	Horizontal components of the isoneutral slopes
Sv	Sverdrup = $1 \times 10^6 m^3 s^{-1}$
T	Temperature
T_A	Air temperature at 10 m height
T^s_{clim}	Climatological sea surface temperature
u, v	Horizontal components of the velocity vector $\vec{v}$
$\mathbf{u}^*$	Bolus velocity vector
u^*, v^*	Horizontal components of the bolus velocity vector $\mathbf{u}^*$
U_{10}	Wind speed at 10 m height
w	Vertical component of the velocity vector $\vec{v}$
w^*	Vertical component of the bolus velocity vector $\mathbf{u}^*$

$AABW$	Antarctic Bottom Water
CAA	Canadian Arctic Archipelago
CFS	Flux Corrected Simulation

CS	Control Simulation
$DOME$	Dynamics of Overflow Mixing and Entrainment
$DSOW$	Denmark Strait Overflow Water
EGC	East Greenland Current
$EGIC$	East Greenland Irminger Current
EKE	Eddy Kinetic Energy
FD	Finite Difference
FE	Finite Element
FEA	Finite Element Analysis
$FEOM$	Finite Element Ocean Model
FS	Flux incorporated Simulation
FV	Finite Volume
FWC	Freshwater Content
FWT	Freshwater Transport
$GFZW$	Gibbs Fracture Zone Water
GM	Gent and McWilliams
GIN	Greenland Iceland-Norwegian Sea
HT	Heat Transport
IC	Irminger Current
$ICES$	International Council for the Exploration of the Sea
$ISOW$	Iceland Scotland Overflow Water
$JEBAR$	Joint Effect of Baroclinicity and Relief
$L.H.S$	Left Hand Side
LC	Labrador Current
$LLSW$	Lower Labrador Sea Water
$LNADW$	Lower North Atlantic Deep Water
LSW	Labrador Sea Water
MKE	Mean Kinetic Energy
MLD	Mixed Layer Depth
MOC	Meridional Overturning Circulation
$NABW$	North Atlantic Bottom Water
NAC	North Atlantic Current

$NADW$	North Atlantic Deep Water
PP	Pacanowski-Philander
$R.H.S$	Right Hand Side
SE	Spectral Element
SSH	Sea Surface Height
SSS	Sea Surface Salinity
SST	Sea Surface Temperature
$ULSW$	Upper Labrador Sea Water
WGC	West Greenland Current
WOA	World Ocean Atlas

Chapter 1

Introduction

1.1 North Atlantic Ocean

The North Atlantic Ocean plays a major role in driving our planet's climate. This includes the transport of excess heat from the subtropical Atlantic to the Arctic through Nordic seas (Lamb, 1981; Fasullo and Trenberth, 2008) and dense waters to the south as deep water. This is an important branch of the global heat energy transport budget, which keeps our planet's climate in equilibrium. According to Lamb (1981), the North Atlantic Ocean transports an annual average of $\approx 1PW$ ($1PW = 1 \times 10^{15}W$) heat transport across 15^oN compared to a global maxima of $1.2PW$ at 15^oN. Which is comparable to the global maxima of atmospheric transport of $5.9PW$ at 35^o (Fasullo and Trenberth, 2008).

The North Atlantic Ocean extends northward from the equator to the Arctic Ocean, comprises the sub-tropical gyre, subpolar gyre and the Arctic region (Worthington, 1976). The mid-latitude gyre of the North Atlantic includes a warm North Atlantic Current (NAC), a continuation of the Gulf Stream linking the subtropical and subpolar gyre and thus transporting heat from low latitudes to high latitudes (Rago and Rossby, 1987; McCartney and Talley, 1984).

The warm waters of the subtropical gyre crosses into the subpolar region near 50^oN through distinct pathways (Figure-1.1) during the process of transformation into cold dense deep waters. The majority of this warm water is converted into dense water within the Nordic and Polar Seas and flows as dense overflows across the Greenland Scotland ridge system as Denmark Strait Overflow Water (DSOW) (Worthington, 1970). The entrainment of warm water occurs south of the Nordic Seas in the overflows as they sink into deep levels through the exchange of heat.

In the Labrador Sea, the transformation of this warm water into Labrador Sea Water (LSW) is through the intense cooling in its boundary current region (Talley and McCartney, 1982) and through the process of deep convection detailed in section-1.2.2.

1.2 Labrador Sea

The western subpolar gyre largely comprises the Labrador Sea, which connects to the Arctic through the Nordic Seas and Canadian Arctic Archipelago (CAA). The region is located between the Labrador coast of Canada and the west coast of Greenland. The Labrador Sea is connected to Baffin Bay through Davis Strait and south to the subtropical gyre of the North Atlantic (Worthington, 1970; Schmitz and McCartney, 1993).

The Labrador Sea is characterized by two boundary currents, a low saline-cold Labrador current that flows southward along the Labrador coast and a West Greenland Current(WGC) which is a combination of fresh and cool waters of the East Greenland Current (EGC) and warmer and saltier waters of the Irminger Current (IC) forming a cyclonic circulation around the central Labrador Sea (Figure 1.1).

Even though an earlier study of Houghton and Visbeck (2002) showed that the dominant annual mean freshwater source (60 %) into the Labrador Sea is the Baffin Island Current (BIC) which then transfers to the Labrador current, a recent study by Schmidt and Send (2007) found that the 60% of freshwater into the Labrador Sea is coming from the WGC in late summer. In addition, Myers (2005) found a limited exchange of freshwater between the Labrador shelf and the interior of the Labrador Sea, thus playing a relatively minor role in setting the convection depth for the Labrador Sea interior.

1.2.1 Boundary currents

1.2.1.1 East Greenland Current (EGC)

The East Greenland Current (EGC) flows along the east coast of Greenland constrained to the continental margin, extending from Fram Strait to Cape Farewell via Denmark Strait. This current transports a mixture of Arctic waters and the densified Atlantic waters of the eastern subpolar gyre (Holliday *et al.*, 2007). One branch of this current flows eastward along the Jan Mayen Fracture Zone and circulates around the Greenland Sea region (Hopkins, 1991). Near Cape Farewell, the cold and fresh Arctic origin waters ($\theta \sim$ 3 - 6^oC, S $<$ 34.95) of this current meet the warm saline ($\theta \sim$ 6 - 9^oC, S $\sim$ 34.95 - 35.05) Irminger water in surface-to-intermediate depths (Holliday *et al.*, 2006), associated with Spill Jet (Pickart *et al.*, 2005) and cold dense overflow waters at depth. According to Serreze *et al.* (2006) the EGC transports 50 to 70% of the liquid freshwater and sea ice from the Arctic ocean. This major source of freshwater reaches the Labrador Sea through the West Greenland Current (WGC) system (Aagaard and Carmack, 1989; Dickson *et al.*, 1996). However a recent decadal study of mooring data across the East Greenland Irminger Current (EGIC) (part of EGC south of the Denmark Strait) shows no significant trend in the transport time series from 1992 to 2009 (Daniault *et al.*, 2011). This result brings up the importance of the following two boundary currents of the subpolar region in setting the convection depth in the Labrador Sea interior.

1.2.1.2 West Greenland Current (WGC)

The West Greenland Current (WGC), fed from the East Greenland Current(EGC) flows north along the shelf and shelf break of the west coast of Greenland (Cuny *et al.*, 2002). Near Cape Desolation, the WGC splits into two branches. One branch continues to flow along the Greenland coast and then combines with Baffin Island Current after passing through Baffin Bay (Melling *et al.*, 2001). The second branch flows westward and combines with the Labrador Current (Cuny *et al.*, 2002).

Rykova (2010) found a seasonal cycle in both the surface WGC and subsurface Irminger Current velocities primarily due to the baroclinic component of the current, which could impact the restratification of the Labrador Sea.

The analysis of the surface drifters by Schmidt and Send (2007) found that, 60% of the freshwater pulse of later summer (July to September) in the Labrador Sea is coming from the WGC.

The branch that combines with the Labrador Current shows high variability, due to the eddies near the shelf break between Greenland and Labrador (Myers *et al.*, 1989). This current also transports small ice-bergs into Baffin Bay and then to the Labrador Current, which then recirculates in the Labrador Sea. But an eddy-permitting model study with an enhanced freshwater export through Davis strait by Myers (2005) showed little effect on the freshwater content in the Labrador Sea interior.

1.2.1.3 Labrador Current (LC)

The LC is the continuation of the Baffin Island Current (cold-fresh) and the warm and more saline waters of a branch of the WGC. The Baffin Island Current flows south along Hudson Strait through the west side of Davis Strait and reaches the Labrador Current, then flows over the continental shelf and upper slope of the Labrador Sea (Lazier and Wright, 1993). This current splits into two at Hamilton-Bank as a small inshore branch (15 %) and an upper continental slope branch (85%). Over the shelf, the water is dominated by low temperature and low salinity (from the inshore branch of Baffin Island Current) compared to that of the open-ocean waters, giving rise to a high vertical shear at shelf break leading to a baroclinically unstable regime (Lazier and Wright, 1993).

Both the Baffin Island Current and the Labrador Current over the upper slope are buoyancy driven flows while the deep Labrador Current over the upper slope is found to be a part of the North Atlantic subpolar gyre. This has been shown by Lazier (Lazier and Wright, 1993) using a Joint Effect of Baroclinicity and Relief (JEBAR) term in the estimation of upper slope transport. Velocity in the baroclinic regime over the shelf and slope is modulated by the annually varying freshwater flux (caused by the river runoff and ice melt in the spring and summer) into the shelf, while the barotropic regime off shore is modulated by the annual variation in the wind stress over the subpolar gyre (Lazier and Wright, 1993). The level of the sea surface is always higher over the Labrador shelf than over the open ocean. This drives a geostrophic current.

Both the Labrador Current and the West Greenland Current show variabilities in freshwater, due to the prevalent eddies in this region. These currents also show substantial inter-annual as well as annual variability in their salinity. One such example can be attributed to the Great Salinity Anomalies of the 70's (Dickson *et al.*, 1984) and a recent low salinity anomaly in 1982 and in the Labrador Current in 1983 (Belkin *et al.*, 1998).

1.2.2 Water masses

The three main water masses in the Labrador Sea (Reynaud *et al.*, 1995) are,

1. The Denmark Strait Overflow water (DSOW) or North Atlantic Bottom Water (NABW) is formed in the Greenland Sea (densified and sinks then flows around Cape Farewell into the Labrador Sea). The large heat loss into the overlying atmosphere and brine rejection during ice formation makes this water more dense to eventually flow at densities of $\sigma_\theta \geq 27.9$ kg m $^{-3}$.

2. The North Atlantic Deep Water (NADW), formed in the Greenland Iceland Norwegian sea (GIN). It is a mixture of LSW and Lower North Atlantic Deep Water (LNADW, comprised of Gibbs Fracture Zone Water (GFZW) and DSOW) (Swift, 1984), with a small addition of southern hemisphere Antarctic Bottom Water (AABW) (Goodman, 1998), found above the DSOW ($27.8 \leq \sigma_\theta < 27.88$ kg m^{-3})

3. The Labrador Sea is one of the regions in the world's ocean where deep convection occurs in the winter as part of a huge loss of heat (average of $\sim$ 200 $W\ m^{-2}$, (Smith and Dobson, 1984), making it a primary cause) to the overlying atmosphere, which is considered as an important process in the conveyor belt theory of the global thermohaline circulation (Rahmstorf, 2000). This deep convection produces a thoroughly mixed layer of around

1000-2000 m depth (Kitauchi, 2007; Clarke and Gascard, 1983), producing weakly stratified Labrador Sea Water (LSW), which then disperses through the mid depths of the North Atlantic Ocean (Talley and McCartney, 1982). This water mass is found above NADW in the density range of $27.68 \leq \sigma_\theta \geq 27.8$ kg m^{-3}, which can be further classified into upper LSW (ULW) in the density range of $27.68 \leq \sigma_\theta \geq 27.74$ kg m^{-3} and lower LSW (LLSW) of range $27.74 \leq \sigma_\theta \geq 27.8$ kg m^{-3} (Pickart, 1992).

The recent extensive freshening in the Labrador Sea (Curry *et al.*, 2003; Curry and Mauritzen, 2005) has received considerable attention in the oceanographic community. The main sources of freshwater input into the Labrador Sea over the recent decades includes the periods of excess precipitation (Myers *et al.*, 2007; Schmidt and Send, 2007), outflow from the Arctic through Canadian Arctic Archipelago and Baffin Bay and from the East Greenland Current (EGC), flowing around the Cape of Farewell and then as West Greenland Current(WGC). Remaining sources of freshwater are from the melting of ice that drifts with the shelf and Labrador Current (LC) (Khatiwala *et al.*, 2002).

Hudson Bay runoff is not as important for the Labrador Sea fresh water annual minimum; because of the inconsistent timing (Myers *et al.*, 1990), moreover the runoff record shows a decreasing trend in the flow since 1965 (Houghton and Visbeck, 2002). Apart from the atmospheric fluxes, the thickness of this freshwater cap atop the gyre interior also determines the depth of convection in the Labrador Sea, which eventually influences the Meridional Overturning Circulation (MOC), a measure of thermohaline circulation. In support, the modelling study of (Goosse *et al.*, 1997) found a reduction in their model's overturning circulation by a factor of 10 % while opening the freshwater input through the Canadian Arctic Archipelago (CAA) passage. A similar result is obtained for other studies in this region (Wadley and Bigg, 2002; Cheng and Rhines, 2004), in contrast to an increase of 21 % in the Atlantic deep circulation found by Komuro and Hasumi (2005). However these studies often represented the CAA as a wide channel as closed instead of it's real complex morphology. Meanwhile a recent study of (Myers, 2005) shows that the freshwater export through Davis Strait from the CAA has little effect on the freshwater content in the interior Labrador Sea and LSW formation. However a recent high resolution modelling study of McGeehaan and Maslowski (2011) argues that, even though the freshwater flux anomalies entering the Labrador Sea through Davis Strait do not immediately affect the deep convection, short term eddies can move freshwater to the active convection location and impact the process.

Convection in the interior of the Labrador Sea is also found to be influenced by the strength of the cyclonic boundary currents, which brings the freshwater into the region and also facilitates the pre-conditioning (Cuny *et al.*, 2002) and restratification after deep convection (Katsman *et al.*, 2004). A major feature which is important for the communication between the interior and these boundary currents that surround the Labrador Sea are the geostrophic eddies (Khatiwala and Visbeck, 2000; Katsman *et al.*, 2004).

1.2.3 Boundary current eddies

The boundary currents of the Labrador Sea (WGC and LC) have an important role in the winter deep convection and the successive restratification in summer (Straneo, 2006*b*) of the Labrador Sea interior.

The main agent contributing to the restratification of Labrador Sea is the presence of enhanced eddies in these boundary currents (Katsman *et al.*, 2004) Also, the transport of heat into the Labrador Sea interior through the warm boundary current is essential for the balance of annual mean heat loss to the atmosphere.

One of the prominent sources of Eddy Kinetic Energy (EKE) in the WGC is derived from the instability characteristics of the current upon it's turning around the tip of Greenland. This feature is associated with the topographic features, mean flows and eddy energy (Eden and Boning, 2002). Eden and Boning (2002), argued that the annual march of EKE can be attributed to a seasonal modulation of this energy transfer, due to a seasonally varying strength of the mean WGC. In addition to this, the narrowing of the topographically guided WGC near Cape Desolation leads to locally strong horizontal shears sufficient for the occurrence of barotropic instability, leading

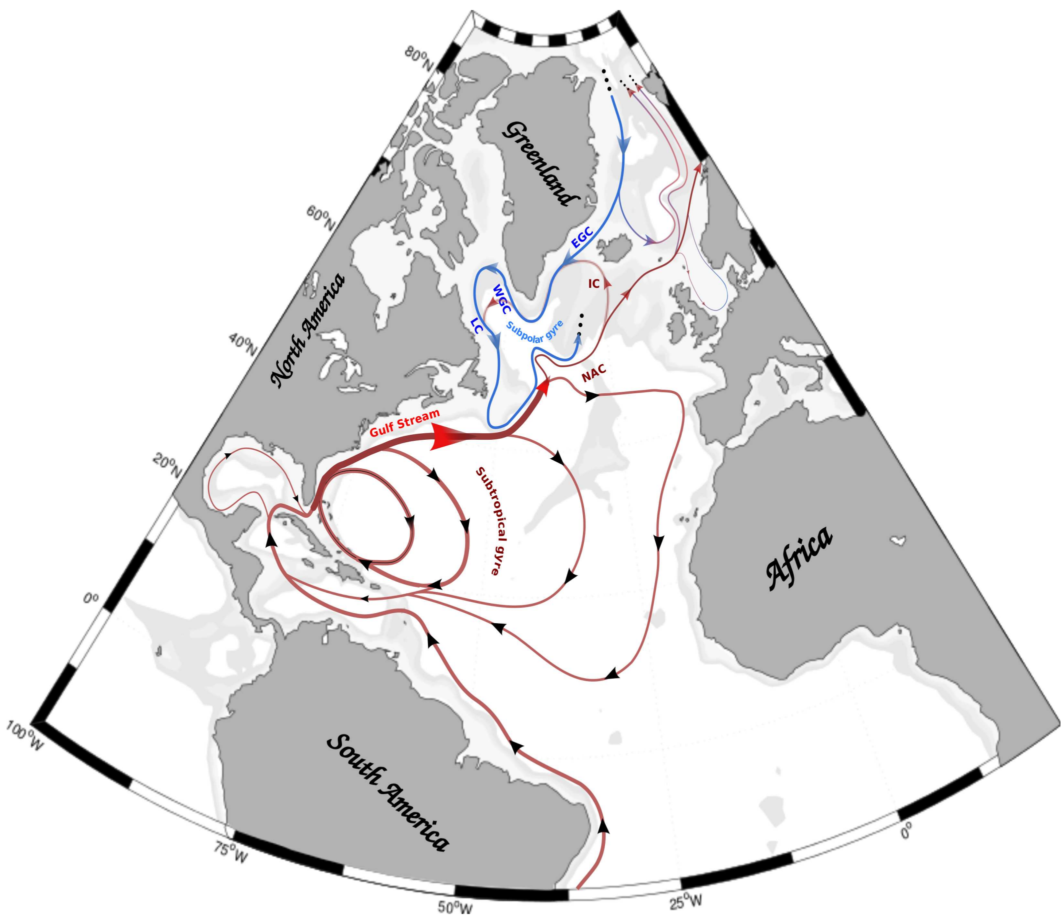

Figure 1.1: Schematic currents of the North Atlantic Ocean

to the main cause of eddies. Here the geostrophic contours tend to converge upstream of Cape Desolation, such that the topographically guided WGC narrows as well and becomes barotropically unstable. These eddies then spread from the WGC area into the areas of deep winter convection (Eden and Boning, 2002), which in turn dominates the EKE of the interior Labrador Sea. Eddies formed near the separation of the WGC off Greenland and propagating into the interior Labrador Sea are predominantly anticyclonic, with warm and saline (but lighter than the surrounding water) cores in the upper 1000 m of the water column. This can bring the stratification of Labrador Sea back into the preconvection state.

The instability processes for the production of these eddies are found to be mixed. The barotropic energy conversion rate is important in the upper water column, while the baroclinic energy conversion rate is the largest at mid-depths (Katsman *et al.*, 2004) and is governed by the topography near the west coast of Greenland. These eddies are found to be more effective than rim current (caused by the simultaneous slumping and geostrophic adjustment of the heavy mixed patch in thermal wind balance, cyclonic above and anticyclonic below (Jones and Marshall, 1997)) eddies in the restratification of the Labrador Sea (Eden and Boning, 2002).

In contrast to the WGC, baroclinic instabilities appear as the dominant source of an EKE maximum in the LC between 1000 and 2000m isobaths (Cuny *et al.*, 2002; Cuny and Rhines, 2005) , which is only moderately enhanced and seems to play a minor role in the restratification process (Eden and Boning, 2002). These eddies extract available potential energy (APE) from the large scale density field causing an overturning circulation transporting buoyant low saline water from the boundary current towards the interior and newly ventilated LSW at depth towards boundaries (Khatiwala and Visbeck, 2000).

Khatiwala (Khatiwala and Visbeck, 2000) also showed that the strength of the overturning circulation is independent of the intensity of convection, suggesting that it depends only the large scale density distribution. They also found that geostrophic eddies are the primary agents for the communication between between the interior and the boundary currents that surround the

Labrador Sea and thus play an important role in both restratification and dispersing newly ventilated water Khatiwala and Visbeck (2000).

Eden (Eden and Boning, 2002) showed that the seasonally varying eddy field is not related to a forcing by high-frequency wind variations but can be explained by a seasonally modulated instability of the West Greenland Current (WGC). The main source of EKE in the Labrador Sea came from an energy transfer due to Reynolds interaction work (barotropic instability) in a confined region near Cape Desolation where the WGC adjusts to a change in the topographic slope.

Even though the North Atlantic Ocean is the most studied region of the world ocean, the observed data in this region are still limited. Numerical models are one of the useful and alternative tools to fill this void. The scarcity of continuous oceanographic observations in the subpolar region of the North Atlantic also makes it difficult for a detailed study. In this scenario of numerical modelling, a proper representation of topography, eddy processes and freshwater input from the Canadian Arctic Archipelago and the boundary currents has crucial importance in the deep convection and restratification (Straneo, 2006*b*; Eden and Boning, 2002) of the Labrador Sea.

Numerical modeling of the subpolar North Atlantic with proper representation of the hydrography and circulation at the same time is still an issue. However an improvement in the subpolar North Atlantic circulation was observed while using the partial cell (Adcroft *et al.*, 1997) approach, where the bottom cells near the bed are partially filled with topography, providing an improved representation of the ocean bottom (Kase *et al.*, 2001; Myers, 2002). On the contrary by using this method, Myers (2002) found a significant increase in the salinity of Labrador sea in his eddy permitting model, similar to the recent comparison study of four high resolution models of the subpolar North Atlantic (Treguier *et al.*, 2005). Deacu and Myers (2005) further improved this salinity drift and also the circulation of the region by incorporating a variable eddy transfer coefficient (Visbeck *et al.*, 1997) that varies spatially and temporally in their Gent and McWilliams (GM) parameterization (Gent and McWilliams, 1990). These studies show the importance of unresolved sub-grid scale eddy process in the modelling of circulation and hydrography of the subpolar North Atlantic Ocean. An unstructured ocean model could also adopt such techniques for the better representation of the hydrography and eddies in the model.

1.3 Unstructured grid modelling in oceanography

Finite Element Analysis (FEA) was first developed by R. Courant in 1943 (Courant, 1943) to study vibration systems, which has later undergone broader improvements (Turner *et al.*, 1956). In recent years, irregular grid models are getting much attention in the ocean modelling community (Danilov *et al.*, 2004, 2005; Chen *et al.*, 2006; Wang *et al.*, 2008). Many finite difference models have adopted various techniques to achieve this goal, including the introduction of curvilinear and nested grids. Most of these techniques are costly and introduce new issues (Peggion, 1994). This makes the finite element (FE), finite volume (FV) and spectral element (SE) approaches more attractive, which has a traditional unstructured grid.

The striking advantages of these numerical methods is the ease by which one may use unstructured grids, based upon a piece-wise instead of point-wise approximation to the governing equations. The advantages of an unstructured grid are particularly important in oceanography, as one must deal with irregular coastlines, numerous islands and narrow straits. The second advantage of unstructured methods is that they allow for relatively easy grid refinement to provide high resolution in regions of interest.

Examples might be: 1) western boundary currents - important for heat transport, climate and water mass dispersal. By providing high resolution near the boundary layer, the computational effort is concentrated where needed for the flow and not elsewhere

2) regions of rapid topographic change such as along the continental shelf break where an accurate representation of upwelling is important for coupled bio-physical problems (Werner *et al.*, 1993; Allen *et al.*, 2001). Finally, the

constraint of structured grids based on geographical coordinates near the pole requiring unacceptable small time steps through the convergence of the meridians can be avoided in unstructured grids.

Furthermore, for an unstructured method such as finite elements, one can show that the method rests on a rigorous mathematical framework based on a weighted residual formulation that permits a precise definition of notions such as error, convergence rate and stability conditions (Hanert *et al.*, 2003). Boundary conditions are also treated naturally, and at least for finite elements, can be shown to enter the weak formulation of the problem directly with no further impositions or approximations (Myers and Weaver, 1995). Over the last one to two decades, interest in unstructured grid methods in oceanography has been growing. Initial applications were associated with the coastal and tidal modeling communities (Lynch *et al.*, 1996; Walters, 1992; Westernik and Gray, 1991; Provost and Vincent, 1991) where this method has continued to be used with great success (Foreman *et al.*, 2000; Han and Loder, 2003). Open ocean applications were initially associated with simplified domains (Provost, 1986; Myers and Weaver, 1995; Iskandarani *et al.*, 2003) or diagnostic problems (Myers and Weaver, 1995; Greenberg *et al.*, 1998). More recently, a number of very sophisticated models and/or modeling system based on unstructured grid methods have been developed and show great initial success (Pain *et al.*, 2001; Iskandarani *et al.*, 2003; Danilov *et al.*, 2004; Walters *et al.*, 2005; Chen *et al.*, 2006; White *et al.*, 2008). This work has been underpinned with a growing focus on the theoretical questions involved with the development of these models (Roux *et al.*, 1998; Roux and Lin, 2000; Hanert *et al.*, 2003; Dupont and Lin, 2004; Levin *et al.*, 2006).

One of the sophisticated new generation of finite element ocean general circulation model is the Finite Element Ocean Model (FEOM) developed in Alfred Wagner institute for Polar and Marine Research, Germany. This model is developed out of the diagnostic model of (Nechaev *et al.*, 2003), solving the primitive equations, as well as the advection-diffusion equations for tracers using implicit time stepping (Danilov *et al.*, 2004). A key aspect of this model (Danilov *et al.*, 2004) was the use of an irregular 3D mesh composed of tetrahedra. Tested on the North Atlantic, Danilov *et al.* (2004) argued that the model is able to integrate for 16 years with reasonable skill.

This version of the FEOM is validated at eddy-permitting resolutions (Danilov *et al.*, 2005) as well as by adding a representation of sloping bottom similar to the partial cell approach used in finite difference models (Adcroft *et al.*, 1997). Validation was done through comparison with the finite difference models of the DYNAMO project (Willebrand *et al.*, 2001). (Danilov *et al.*, 2005) argued that FEOM's circulation is well constrained by the DYNAMO models, with good agreement for the Meridional Overturning Circulation (MOC), poleward heat transport as well as mean sea surface height fields and Gulf Stream recirculation.

Recently, FEOM was modified from the 3D tetrahedral elements to a fully unstructured triangular mesh on the horizontal with prismatic elements in the vertical, which is summarized in detail in Wang *et al.* (2008). The model was used to study the overflow problem associated with the DOME (Dynamics of Overflow Mixing and Entrainment) setup (Wang *et al.*, 2008). However, the new formulation has not been tested in a full basin scale configuration, which is the focus of this thesis. Additionally, although the thesis examines the circulation issues as done by Danilov *et al.* (2005), it also considers the model's hydrography, since in some ways this is a more difficult problem, yet crucial when one wishes to have the model used for realistic oceanographic problems. As part of the goal to understand the model's hydrography, it uses a more realistic surface boundary conditions than the basic restoring to temperature and salinity used in previous studies (Danilov *et al.*, 2004, 2005).

Unstructured grid modeling also has some issues. This includes the incorrect representation of the geostrophic balance and the nonphysical wave scattering due to the change in grid spacing (Griffies *et al.*, 2000). This limited the application of FEM in the modelling of barotropic tides and wind driven ocean circulation and also in engineering and coastal oceanography (eg: Dartmouth University model QUODDY, Advanced Circulation Model (ADCIRC) etc.). However recent studies of the basin scale has shown that FEM results are comparable with that of the traditional Finite Difference (FD) models

(Danilov *et al.*, 2005) in reproducing large scale circulation and hydrography.

An evaluation of the eddy permitting Finite Element Ocean Model (FEOM) with tetrahedral discretization in vertical of (Danilov *et al.*, 2005) and the DYNAMO (Dynamics of the North Atlantic Models) inter-comparison project argued that, FEOM is capable of reproducing features of the circulation comparable to that of regular-grid models of finer resolution. However the model showed spurious upwelling around $35^o N$ associated with Gulf Stream separation. They attributed this to the lack of a better sub-grid scale parameterization like GM parameterization scheme (Danilov *et al.*, 2005). This result highlights the importance of representing sub grid scale eddy processes in a FEM as in a FD model (Deacu and Myers, 2005).

1.4 Thesis objectives and outline

The main objectives of this thesis are,

1. Present a well developed configuration of a North Atlantic finite element Ocean model to the ocean modelling community.

2. Apply modern approaches to represent the boundary conditions and mixing, analyze their impact on the simulation results.

3. Parameterize unresolved sub-grid scale eddies, examine the role of boundary current eddies in setting the convection depth in the Labrador Sea interior.

Previous studies towards the first objective are minimal and a full basin scale study using a finite element model is still lacking so that the ocean modelling community can scrutinize the benefits of this class of model. The present thesis achieves this goal for the North Atlantic Ocean using FEOM.

One of the novelties of this thesis is that, even though a few previous modelling studies of the boundary currents have shown the role of boundary current transports in setting the convection depth in the Labrador Sea interior (Spall, 2004; Katsman *et al.*, 2004; Straneo, 2006*a*), all of those studies were carried out in an idealized basin where the model density depends only on temperature. This motivated us to study the importance of these eddies in Chapter-4 for a realistic basin scale ocean by incorporating the unresolved sub-grid scale eddies into the model through a modified GM parameterization (Gent *et al.*, 1995) scheme. The conclusion on the thesis and future work in this topic are detailed in Chapter 5.

Bibliography

Aagaard, K. and E.C. Carmack (1989). The role of sea ice and other freshwater in the Arctic circulation. *Journal of Geophysical Research* **94**, 14485–14498.

Adcroft, A., C. Hill and J. Marshall (1997). Representation of topography by shaved cells in a height coordinate ocean model. *Monthly Weather Review* **125**, 2293–2315.

Allen, S.E., C. Vindeirinho, R.E. Thomson, M.G.G. Foreman and D.L. Mackas (2001). Physical and biological processes over a submarine canyon during an upwelling event. *Canadian Journal of Fisheries and Aquatic Sciences* **58**, 671–684.

Belkin, Igor M., Sydney Levitus, John Antonov and Svend-Aage Malmberg (1998). Great Salinity Anomalies in the North Atlantic. *Progress in Oceanography* **41**, 1–68.

Chen, Changsheng, Robert C. Beardsley and Geoffrey Cowles (2006). Finite-Volume Coastal Model (FVCOM) System. *Advances in computational oceanography* **19**(1), 78–89.

Cheng, W. and Peter B. Rhines (2004). Response of the overturning circulation to high-latitude fresh-water perturbations in the North Atlantic. *Climate Dynamics* **22**, 359–372.

Clarke, R. Allyn and Jean-Claude Gascard (1983). The Formation of Labrador Sea Water. Part I: Large-Scale Processes. *Journal of Physical Oceanography* **13**, 1764–1778.

Courant, R. (1943). Variational methods for the solution of problems of equilibrium and vibrations. *Bulletin of the American Mathematical Society* **49**, 1–23.

Cuny, Jerome and Peter B. Rhines (2005). Convection above the Labrador Continental Slope. *Journal of Physical Oceanography* **35**, 489–511.

Cuny, Jerome, Peter B. Rhines, Pearn P. Niller and Sheldon Bacon (2002). Labrador Sea boundary currents and the fate of the Irminger Sea Water. *J. of Phys.Ocean* **32**, 627–647.

Curry, Ruth G. and Celcilie Mauritzen (2005). Dilution of the Northern North Atlantic Ocean in Recent Decades. *Science* **308**, 1172–1174.

Curry, Ruth G., Bob Dickson and Igor Yashayaev (2003). A change in the freshwater balance of the Atlantic Ocean over the past four decades. *Nature* **426**, 826–829.

Daniault, N., H. Mercier and P. Lherminier (2011). The 1992-2009 transport variability of the East Greenland-Irminger Current at 60^oN. *Geophysical Research Letters*.

Danilov, S., G. Kivman and J. Schroter (2004). A finite-element ocean model: principles and evaluation. *Ocean Modelling* **6**, 125–150.

Danilov, S., G. Kivman and J. Schroter (2005). Evaluation of an eddy-permitting finite-element ocean model in the North Atlantic. *Ocean Modelling* **10**, 35–49.

Deacu, Daniel and Paul G. Myers (2005). Effect of a Variable Eddy Transfer Coefficient in an Eddy-Permitting Model of the Subpolar North Atlantic Ocean. *Journal of Physical Oceanography* **35**, 289–307.

Dickson, Robert, John Lazier, Jens Meincke, Peter Rhines and James Swift (1996). Long-term coordinated changes in the convective activity of the North Atlantic. *Progress in Oceanography* **38**, 241–295.

Dickson, R.R., J. Meincke, S.A. Malmberg and A.J. Lee (1984). The great salinity anomaly in the northern North Atlantic. *Progress in Oceanography* **20**, 103–151.

Dupont, Frederic and Charles A. Lin (2004). The Adaptive Spectral Element Method and Comparisons with More Traditional Formulations for Ocean Modeling. *Journal of Atmospheric and Ocean Technology* **21**, 135–147.

Eden, Carsten and Claus Boning (2002). Sources of Eddy Kinetic Energy in the Labrador Sea. *Journal of Physical Oceanography* **32**, 3346–3363.

Fasullo, T. John and E. Kevin Trenberth (2008). The annual cycle of the energy budget. part ii: Meridional structures and poleward transports. *Journal of Climate* **21**(10), 2313–2325.

Foreman, M.G.G., R.E. Thomson and C.L. Smith (2000). Seasonal current simulations for the western continental margin of Vancouver Island. *Journal of Geophysical Research* **105**, 19665–19698.

Gent, Peter R. and James C. McWilliams (1990). Isopycnal Mixing in Ocean Circulation Models. *Journal of Physical Oceanography* **20**, 150–155.

Gent, Peter R., Jurgen Willebrand, Trevor J. Mc Dougall and James C. McWilliams (1995). Parameterizing eddy-induced tracer transports in ocean circulation models. *Journal of Physical Oceanography* **25**, 463–474.

Goodman, Paul J. (1998). The Role of North Atlantic Deep Water Formation in an OGCM's Ventilation and Thermohaline Circulation. *Journal of Physical Oceanography* **28**, 1759–1785.

Goosse, H., T. Fichefet and J.M. Campin (1997). The effects of the water flow through the Canadian Archipelago in a global ice-ocean model. *Geophysical Research Letters* **24**, 1507–1510.

Greenberg, David A., Francisco E. Werner and Daniel R. Lynch (1998). A Diagnostic Finite-Element Ocean Circulation Model in Spherical-Polar Coordinates. *Journal of Atmospheric and Oceanic Technology* **15**, 942–958.

Griffies, Stephen M., Claus Boning, Frank O. Bryan, Eric P. Chassignet, Rudiger Gerdes, Hiroyasu Hasumi, Anthony Hirst, Anne-Marie Treguier and David Webb (2000). Developments in ocean climate modelling. *Ocean Modelling* **2**, 123–192.

Han, Gouqi and John W. Loder (2003). Three-dimensional seasonal-mean circulation and hydrography on the eastern Scotian Shelf. *Journal of Geophysical Research* **108**, C5,3136.

Hanert, E., V. Legat and E. Deleersnijder (2003). A comparison of three finite elements to solve the linear shallow water equations. *Ocean Modelling* **5**, 17–35.

Holliday, N. Penny, Amelie Meyer, Sheldon Bacon, Steven G. Alderson and Beverly de Cuevas (2007). Retroflection of part of the east Greenland current at Cape Farewell. *Geophysical Research Letters*.

Holliday, N. Penny, J.J. Waniek, R. Davidson, D. Wilson, L. Brown, R. Sanders, R.T. Pollard and J.T. Allen (2006). Large-scale physical controls on phytoplankton growth in the Irminger Sea Part I: Hydrographic zones, mixing and stratification. *Journal of Marine Sciences* **59**, 201–218.

Hopkins, Tom Sawyer (1991). The GIN Sea – A Synthesis of its physical oceanography and literature review 1972-1985. *Earth-Science Reviews* **30**, 175–318.

Houghton, Robert W. and Martin H. Visbeck (2002). Quasi-decadal Salinity Fluctuations in the Labrador Sea. *Journal of Physical Oceanography* **32**, 687–701.

Iskandarani, M., Haidvogel D.B. and Levin J.C. (2003). A three-dimensional sprectral element model for the solution of the hydrostatic primitive equations. *Journal of Computational Physics* **186**, 397–425.

Jones, Helen and John Marshall (1997). Restratification after Deep Convection. *Journal of Physical Oceanography* **27**, 2276–2287.

Kase, R.H., A. Biastoch and D.B. Strammer (2001). On the mid-depth circulation in the Labrador and Irminger Seas.. *Geophysical Research Letters* **28**, 3433–3436.

Katsman, Caroline A., Michael A. Spall and Robert S. Pickart (2004). Boundary Current Eddies and Their Role in the Restratification of the Labrador Sea. *Journal of Physical Oceanography* **34**, 1967–1983.

Khatiwala, Samar and Martin Visbeck (2000). An Estimate of the Eddy-induced Circulation in the Labrador Sea. *Geophysical Research Letters* **27**(15), 2277–2280.

Khatiwala, Samar, Peter Schlosser and Martin Visbeck (2002). Rates and Mechanisms of Water Mass Transformation in the Labrador Sea as Inferred from Tracer Observations. *Journal of Physical Oceanography* **32**, 666–686.

Kitauchi, Hideaki (2007). An Eddy-Resolving Labrador Sea Modeling studied by a Coupled Sea Ice-Ocean Circulation Model. In: *Annual Report of the Earth Simulator Center, Chapter-I Earth science*. pp. 57–62. University of Tokyo.

Komuro, Yoshiki and Hiroyasu Hasumi (2005). Intensification of the Atlantic Deep Circulation by the Canadian Archipelago Throughflow. *Journal of Physical Oceanography* **35**, 775–789.

Lamb, Peter J. (1981). Estimate of annual variation of Atlantic Ocean heat transport. *Nature* **290**, 766–768.

Lazier, John and D.G. Wright (1993). Annual velocity Variations in the Labrador Current. *Journal of Physical Oceanography* **23**, 659–678.

Levin, J.C., M. Iskandarani and D.B. Haidvogel (2006). To continue or discontinue: Comparisons of continuous and discontinuous Galerkin formulations in a spectral element ocean model. *Ocean Modelling* **15**, 56–70.

Lynch, D.R., T.C. Ip Justin, C.E. Naimie and F.E. Werner (1996). Comprehensive coastal circulation model with application to the Gulf of Maine. *Continental Shelf Research* **16**, 875–906(32).

McCartney, M.S. and L.D. Talley (1984). Warm-to-Cold Water Conversion in the North Atlantic Ocean. *Journal of Physical Oceanography* **14**, 922–935.

McGeehaan, Timothy and Wieslaw Maslowski (2011). Impact of Shelf-Basin Freshwater Transport on Deep Convection in the Western Labrador Sea. *Journal of Physical Oceanography* **41**, 2187–2210.

Melling, Humfrey, Yves Gratton and Grant Ingram (2001). Ocean circulation within the North Water polynya of Baffin Bay. *Atmosphere-Ocean* **39**, 301–325.

Myers, Paul G. (2002). SPOM: A regional model of the sub-polar North Atlantic. *Atmosphere-Ocean* **40**, 445–463.

Myers, Paul G. (2005). Impact of freshwater from the Canadian Arctic Archipelago on Labrador Sea Water formation. *Geophysical Research Letters* **32**, L06605.

Myers, Paul G. and A.J. Weaver (1995). A diagnostic barotropic finite-element ocean model. *Journal of Atmospheric and Oceanic Technology* **12**, 511–526.

Myers, Paul G., Simon A. Josey, Brett Wheler and Nilgun Kulan (2007). Interdecadal variability in Labrador Sea precipitation minus evaporation and salinity . *Progress in Oceanography* **73**, 341–357.

Myers, R.A., J. Helbig and D. Holland (1989). Seasonal and interannual variability of the Labrador Current and West Greenland Current. *ICES C.M* **C: 16**, 10.

Myers, Ransom A., Scott A. Akenhead and Ken Drinkwater (1990). The influence of Hudson Bay Runoff and Ice-Melt on the Salinity of the Inner Newfoundland Shelf. *Atmosphere-Ocean* **28 (2)**, 241–256.

Nechaev, Dimitri, Jens Schroter and Max Yaremchuk (2003). A diagnostic stabilized finite-element ocean circulation model. *Ocean Modelling* **5**, 37–63.

Pain, C.C., A.P. Umpleby, C.R.E. de Oliveira and A.J.H. Goddard (2001). Tetrahedral mesh optimisation and adaptivity for steady-state and transient finite element calculations. *Computational Methods in Applied Mechanics and Engineering* **190**, 3771–3796.

Peggion, Germana (1994). Numerical Inaccuracies Across the Interface of a Nested Grid. *Numerical Methods for Partial differential Equations* **10**, 455–473.

Pickart, Robert S. (1992). Water mass components of the North Atlantic deep western boundary current. *Deep-Sea Research* **39**, 1553–1572.

Pickart, Robert S., Daniel J. Torres and Paula S. Fratantoni (2005). The East Greenland Spill Jet*. *Journal of Physical Oceanography* **35**, 1037–1053.

Provost, Le (1986). On the use of finite element methods for ocean modelling. In: *Advanced Physical Oceanographic Numerical Modelling* (James J. O'Brien, Ed.). pp. 557–580. D. Reidel Publishing Company.

Provost, Le and Patrick Vincent (1991). Finite-Element Method for Modelling Ocean Tides. In: *Tidal Hydrodynamics* (Bruce B. Parker, Ed.). pp. 41–60. National Oceanic and Atmospheric Administration, John Wiley and Sons, Inc, New York .

Rago, Thomas A. and Thomas H. Rossby (1987). Heat Transport into the North Atlantic Ocean North of 32^0N Latitude. *Journal of Physical Oceanography* **17**, 854–871.

Rahmstorf, Stefan (2000). The Thermohaline Ocean Circulation: A System with Dangerous Thresholds. *Climate Change* **46**, 247–256.

Reynaud, T.H., A.J. Weaver and R.J. Greatbatch (1995). Summer Mean Circulation of the northwestern Atlantic Ocean. *Journal of Geophysical Research* **100**, 779–816.

Roux, Daniel Y. Le and Charles A. Lin (2000). A Semi-implicit Semi-Lagrangian Finite-Element Shallow-Water Ocean Model. *Monthly Weather Review* **128**, 1384–1401.

Roux, Daniel Y. Le, Andrew Staniforth and Charles A. Lin (1998). Finite Elements for Shallow-Water Equation Ocean Models. *Monthly Weather Review* **126**, 1931–1951.

Rykova, Tatiana (2010). The Seasonal and Interannual Variability of the West Greenland Current System in the Labrador Sea. PhD thesis. Massachusetts Institute of Technology and Woods Hole Oceanographic Institution, USA.

Schmidt, Sunke and Uwe Send (2007). Origin and Composition of Seasonal Labrador Sea Freshwater. *Journal of Physical Oceanography* **37**, 1445–1454.

Schmitz, William J. and Michael S. McCartney (1993). On the North Atlantic Circulation. *Reviews of Geophysics* **31**(1), 29–49.

Serreze, Mark C., Andrew P. Barrett, Andrew G. Slater, Rebecca A. Woodgate, Knut Aagaard, Richard B. Lammers, Michael Steele, Richard Moritz, Michael Meredith and Craig M. Lee (2006). The large-scale freshwater cycle of the Arctic. *Journal of Geophysical Research*.

Smith, Stuart D. and Fred W. Dobson (1984). The Heat Budget at Ocean Weather Station Bravo. *Atmosphere-Ocean* **22 (1)**, 1–22.

Spall, Michael A. (2004). Boundary Currents and Watermass Transformation in Marginal Seas. *Journal of Physical Oceanography* **34**, 1197–1213.

Straneo, Fiammetta (2006*a*). Heat and Freshwater Transport through the Central Labrador Sea. *Journal of Physical Oceanography* **36**, 606–628.

Straneo, Fiammetta (2006*b*). On the connection between dense water formation, overturning and poleward heat transport in a convective basin. *Journal of Physical Oceanography* **36**, 1822–1840.

Swift, James H. (1984). The Circulation of the Denmark Strait and Iceand-Scotland overflow waters in the North Atlantic. *Deep Sea Research* **31**, 1339–1355.

Talley, L.D. and M.S. McCartney (1982). Distribution and Circulation of Labrador Sea Water. *Journal of Physical Oceanography* **12**, 1189–1205.

Treguier, A.M., S. Theetten, E.P. Chassignet, T. Penduff, R. Smith, L. Talley, J.O. Beismann and C. Boning (2005). The North Atlantic Subpolar Gyre in Four High-Resolution Models . *Journal of Physical Oceanography* **35**, 757–774.

Turner, M.J., Ray W. Clough, H.C. Martin and L.J. Topp (1956). Stiffness and deflection analysis of complex structures. *Journal of Aeronautical Sciences* **23**, 805–823.

Visbeck, Martin, John Marshall and Tom Haine (1997). Specification of eddy transfer coefficients in coarse-Resolution ocean circulation Models. *Journal of Physical Oceanography* **27**, 381–402.

Wadley, Martin R. and Grant R. Bigg (2002). Impact of flow through the Canadian Archipelago and Bering Strait on the North Atlantic and Arctic circulation: An ocean modelling study. *Quarterly Journal of the Meteorological Society* **128**, 2187–2203.

Walters, Roy A. (1992). A three-dimensional, finite element model for coastal and estuarine circulation. *Continental Shelf Research* **12**, 83–102.

Walters, Roy A., E.M. Lane and R.F. Henry (2005). Semi-Lagrangian methods for a finite element coastal ocean model. *Ocean Modelling* **19**, 112–124.

Wang, Q., S. Danilov and J. Schroter (2008). Comparison of overflow simulations on different vertical grids using the Finite Element Ocean circulation Model. *Ocean Modelling* **20**, 313–335.

Werner, Francisco E., Fred H. Page, Daniel R. Lynch, John W. Loder, R. Gregory Lough, R. Ian Perry, David A. Greenberg and Michael M. Sinclair

(1993). Influences of mean advection and simple behavior on the distribution of cod and haddock early life stages on Georfes Bank. *Fisheries Oceanography* **2:2**, 43–64.

Westernik, Joannes J. and Willian G. Gray (1991). Progress in Surface Water Modeling. *Reviews of Geophysics, suppliment* **29**, 210–217.

White, Laurent, Vincent Legat and Eric Deleersnijder (2008). Tracer Conservation for Three-Dimensional, Finite-Element, Free-Surface, Ocean Modeling on Moving Prismatic Meshes. *Monthly Weather Review* **136**, 420–442.

Willebrand, J., Barnier B., Boning C., Dieterich C., Killworth P.D., Le Provost C., Jia Y., Molines J.M. and New A.L. (2001). Circulation characteristics in three eddy-permitting models of the North Atlantic.. *Progress in Oceanography* **48**, 123–161.

Worthington, L.V. (1970). The Norwegian Sea as a Mediterranean basin. *Deep-Sea Research* **17**, 77–84.

Worthington, L.V. (1976). On the North Atlantic circulation. *John Hopkins University Press, Baltimore* **6**, 1–110.

Chapter 2

Finite Element Model

This Chapter details the configuration and numerical principles used in the finite element model FEOM.

2.1 The model and configuration

A prismatic version (Figure-2.1) of the FEOM with triangular 2D elements and geopotential vertical coordinate is adopted. Previous versions of the same model had tetrahedral elements with a similar class of piecewise linear basis functions (Wang *et al.*, 2008). More details on configuration and formulation of this model are described in the following sub-sections.

2.1.1 Primitive equations of motion

In this study, a new prismatic version of the FEOM is applied for a North Atlantic configuration. The numerics of the model are the same as that described in Danilov *et al.* (2004) and Danilov *et al.* (2005). The major difference in this version is the use of triangular 2D elements with a z- coordinate in vertical, which makes the model prismatic in the vertical compared to the tetrahedral of the previous versions, which facilitates grid generation.

The *dynamical part* of the model solves the momentum equations under the integral continuity constraint (Danilov *et al.*, 2004).

$$\partial_t \mathbf{u} + f\left[\hat{\mathbf{k}} \times \mathbf{u}\right] + g\nabla_h \zeta - \nabla_h \cdot A_h \nabla_h \mathbf{u} - \partial_z A_v \partial_z \mathbf{u} = -\frac{1}{\rho_o}\nabla p - F_u \tag{2.1}$$

$$\partial_t \zeta + \int_{z=-H}^{z=\zeta} \nabla_h \cdot \mathbf{u}\, dz = 0 \tag{2.2}$$

$$\partial_z p = -g\rho \tag{2.3}$$

$$\partial_z w = -\nabla_h \cdot \mathbf{u} \tag{2.4}$$

where $\mathbf{u}$=(u, v) is the horizontal velocity vector in spherical coordinates (λ, ϕ), w is the vertical velocity, F_u is the non-linear advection term given by $F_u = (\mathbf{u} \cdot \nabla_h + w\partial_z)\,\mathbf{u}$. ∇_h is the horizontal gradient operator, A_h and A_v are the horizontal and vertical mixing coefficients (viscosity coefficients) respectively, ζ is the sea surface elevation, p is the baroclinic pressure, g is the acceleration due to gravity ($9.8\,ms^{-2}$), H is the local water depth, $f = 2\Omega\,\sin(\phi)$ is the Coriolis parameter, $\hat{\mathbf{k}}$ is the unit vector in z direction. ρ_o is the mean sea water density and ρ is the derived density from the equation of state proposed by Jackett and McDougall (1995). The relation can be written in general form as below,

$$\rho = \varrho(\theta, S, p) \tag{2.5}$$

which uses the potential temperature (θ) rather than the insitu temperature (T) and S is the salinity.

The equations (2.1 - 2.3) are solved in the domain (Ω) along with four types of boundaries $\partial\Omega = \cup_{i=1}^{4} = \Gamma_i$. Where Γ_1 stands for the ocean surface, Γ_2 the bottom of the ocean, Γ_3 the lateral rigid walls and Γ_4 the lateral vertical open boundaries (Danilov *et al.*, 2004). These boundary conditions are expressed as a momentum flux continuity on the surface, a bottom-drag condition on the bottom, no-slip boundary conditions on the lateral rigid walls and a sponge layer as the open boundary condition.

$$A_v \partial_z \mathbf{u} = \vec{\tau} \qquad \text{on } \Gamma_1 \tag{2.6}$$

$$p = 0 \qquad \text{on } \Gamma_1 \tag{2.7}$$

$$A_v \partial_z \mathbf{u} + A_h \left(\nabla_h \cdot H \nabla_h\right) \mathbf{u} = C_g \mathbf{u}|\mathbf{u}| \quad \text{on } \Gamma_2 \tag{2.8}$$

$$\mathbf{u} = 0 \quad \text{on } \Gamma_3 \tag{2.9}$$

where τ is the wind stress tangent vector and C_g is the bottom drag coefficient ($2.5 \times 10^{-3}\, Pa.s$). A sponge layer as explained in subsection 2.1.7 is applied on boundary Γ_4. The vertical velocity (w) is integrated from the ocean surface with the following kinematic boundary condition at the surface,

$$w = \partial_t \zeta \quad \text{on } \Gamma_1 \tag{2.10}$$

and at the bottom at depth H

$$w = -\nabla_h H \cdot \mathbf{u} \quad \text{on } \Gamma_2 \tag{2.11}$$

2.1.2 Tracer equations

The *thermodynamic part* of the model solves the tracer evolution equations for potential temperature (θ) and salinity (S) of sea water and equation of state to compute density (eq.2.5)(Danilov *et al.*, 2004).

$$\partial_t C + \mathbf{u} \cdot \nabla_h C + w\, \partial_z C - \nabla_h \cdot K_h \nabla_h C - \partial_z K_v \partial_z C = \frac{F}{\Delta z} \tag{2.12}$$

where C is the tracer, Temperature (T) or Salinity (S). K_h and K_v are the horizontal and vertical diffusion coefficients. F is the source/sink (forcing) for the tracers on boundary Γ_1 and Δz is the depth over which the F is absorbed. In the model, the Δz is selected as 10 m (the depth of first model layer). The sensitivity of the term F is studied and detailed in chapter 3.

2.1.3 Space and time discretization

2.1.3.1 $P_1^{NC} - P_1$ discretization

In this class of discretization, the sea surface height and tracers are approximated by linear conforming (P_1) shape functions and the velocities by nonlinear (P_1^{NC}) shape functions (Figure-2.1). Thus the elevation and tracers are lying on the vertices and velocities at mid-segments of the triangle. These classes of shape functions help to have continuous discrete sea surface height and tracers on every nodes whereas continuous velocity field across the triangle boundaries at mid-side nodes and discontinuous everywhere else around a triangle boundary (Hanert *et al.*, 2005).

2.1.3.2 Spatial discretization

Since the basis function in the model is not twice differentiable, the model equations 2.1-2.2 have to be reformulated into the following weak form by multiplying with an arbitrary vector field $\tilde{\mathbf{u}}$ and a scalar function $\tilde{\boldsymbol{\zeta}}$, which does not depend on z.

$$\int_{\Omega} \left[(\partial_t \mathbf{u} + f\left[\mathbf{k} \times \mathbf{u}\right] + g\nabla_h \zeta) \cdot \tilde{\mathbf{u}} + A_v \partial_z \mathbf{u} \cdot \partial_z \tilde{\mathbf{u}} + A_h \nabla_h \mathbf{u} \cdot \nabla_h \tilde{\mathbf{u}} \right] d\Omega$$
$$= \int_{\Gamma_1} \tau \cdot \tilde{\mathbf{u}} d\Gamma_1 - \int_{\Gamma_2} C_g |\mathbf{u}| \mathbf{u} \cdot \tilde{\mathbf{u}} d\Gamma_2 - \int_{\Omega} \left[(\mathbf{u} \cdot \nabla_h + w\partial_z)\, \mathbf{u} \right] \cdot \tilde{\mathbf{u}} d\Omega - \int_{\Omega} \frac{1}{\rho_0} \tilde{\mathbf{u}} \cdot \nabla p \, d\Omega \tag{2.13}$$

$$\int_{\Gamma_1} \partial_t \zeta \tilde{\boldsymbol{\zeta}} d\Gamma_1 - \int_{\Omega} \mathbf{u} \cdot \nabla_h \tilde{\boldsymbol{\zeta}} d\Omega = 0 \tag{2.14}$$

The model variables ($\mathbf{u}$ and $\boldsymbol{\zeta}$) are then expressed as linear combinations of 3D and 2D piece wise linear basis functions X_k and S_k (Danilov *et al.*, 2004),

$$\mathbf{u} = \sum_{k=1}^{N_{3D}} \mathbf{u_k} X_k, \qquad \boldsymbol{\zeta} = \sum_{k=1}^{N_{2D}} \boldsymbol{\zeta}_k S_k \tag{2.15}$$

where N_{3D} and N_{2D} are the total number of 3D nodes and 2D nodes respectively. These basis functions will have a value of 1 at the k^{th} node and linearly vanishes to 0 in the respective prismatic element so that the residuals are orthogonal to the basis functions. More details on these basis functions are given in Wang *et al.* (2008). By substituting these basis functions into the above weak equations (2.13-2.14) gives us the so-called Galerkin equations.

The nodal values of pressure are calculated (in a finite difference sense) from the hydrostatic equation (eq. 2.3) using the density derived from the equation of state (eq.2.5) and then treated as,

$$p = \sum_{k=1}^{N_{3D}} P_k X_k \tag{2.16}$$

The vertical velocity (w) is calculated from a velocity potential defined as, $w = \partial_z \Phi$. If $\Phi \in X$, then equation (2.4) can be written as (Danilov *et al.*, 2004),

$$\int_{\Omega} \partial_z \Phi \partial_z \tilde{\Phi} d\Omega = -\int_{\Omega} \mathbf{u}.\nabla_h \tilde{\Phi} d\Omega \tag{2.17}$$

The vertical velocity w is then derived from Φ as an element wise constant function (Danilov *et al.*, 2004).

The tracer equation (2.12) uses a similar approach to reach the weak form with a scalar multiplier ($\tilde{\mathbf{C}}$) as below,

$$\int_{\Omega} \left(\partial_t C\tilde{\mathbf{C}} + (\mathbf{u} \cdot \nabla_h + w\partial_z)\, C\tilde{\mathbf{C}} + K_h \nabla_h C \cdot \tilde{\mathbf{C}} + K_v \partial_z C \partial_z \tilde{\mathbf{C}} \right) d\Omega = -\int_{\Gamma_1} Q\tilde{\mathbf{C}} d\Gamma_1 \tag{2.18}$$

Where Q is the sink/source of the tracer field.

2.1.3.3 Time stepping

To allow large time steps, all the terms on the Left Hand Side (LHS) of equations (2.13) and (2.14) are treated implicitly. Whereas the pressure gradient term on the Right Hand Side (RHS) of the equation (2.13) and the momentum advection terms are computed explicitly. The equations (2.13 and 2.14) are then integrated backwards using the Euler scheme with explicit treatment of the momentum advection and hydrostatic terms, computed from the preceding time step (Danilov *et al.*, 2004).

In the tracer equation (2.12) the advection is mainly balanced with the time derivative term. So to ensure the stability in long runs, this term is treated implicitly and integrated in time with a backward Euler scheme. A time step of 3600 seconds is used in the model simulations.

2.1.4 Mixing schemes

The vertical mixing in the model is based on the Pacanowski-Philander (PP) mixing (Pacanowski and Philander, 1981) scheme, which depends on the local Richardson number (R_i) given by,

$$R_i = -\frac{N^2}{\left(\frac{\partial \mathbf{u}}{\partial z}\right)^2} \tag{2.19}$$

where N is the Brunt-Väisälä frequency given by,

$$N = \sqrt{g \frac{1}{\rho_o} \frac{\partial \rho}{\partial z}} \tag{2.20}$$

Then the vertical viscosity (Kv) and diffusivity (A_v) coefficients are given by,

$$K_v = \frac{0.01}{(1 + 5R_i)} + K_{vb} \quad , \quad A_v = \frac{0.01}{(1 + 5R_i)^2} + A_{vb} \tag{2.21}$$

Here the background viscosity coefficient is $A_{vb} = 0.02\, m^2 s^{-1}$ and the diffusion coefficient $K_{vb} = 0.0001\, m^2 s^{-1}$. The vertical mixing of tracers in the model is modified to simulate convection, where a high value of $K_v = 1\, m^2 s^{-1}$ is used when static instability is detected in the model.

In the horizontal a Laplacian mixing scheme is used, where the horizontal viscosity (A_h) decreases from $1000\, m^2 s^{-1}$ to $200\, m^2 s^{-1}$ and horizontal diffusivity (K_h) decreases from $500\, m^2 s^{-1}$ to $100\, m^2 s^{-1}$ in low to high resolution areas of the domain.

2.1.5 Sub-grid scale parameterization: Gent and McWilliams

Sub-grid scale mixing plays a major role in driving the large-scale properties of the ocean. To incorporate this mechanism into the model, the popular GM parameterization scheme is added into the model. Here an eddy induced transport is added into the tracer equation (eq.2.12) by means of a non-divergent "bolus velocity", $\mathbf{u}^*$ (u^*, v^*, w^*) (Gent *et al.*, 1995). The following divergence of advective flux is added to the R.H.S of the tracer equation (eq.2.12),

$$-\nabla \cdot C\mathbf{u}^* \tag{2.22}$$

The $\mathbf{u}^*$ is defined as a rotational stream function $\mathbf{F}^* = (F_x^*, F_y^*, 0)$.

$$\mathbf{u}^* = \nabla \times \mathbf{F}^* = \begin{bmatrix} -\partial_z \mathbf{F}_y^* \\ \partial_z \mathbf{F}_x^* \\ \partial_x \mathbf{F}_y^* - \partial_y \mathbf{F}_x^* \end{bmatrix} \tag{2.23}$$

These stream functions ($\mathbf{F}_x^*$ and $\mathbf{F}_y^*$) are expressed in terms of isoneutral slopes (S_x, S_y and S) as,

$$\mathbf{F}_x^* = K_{gm} S_y \tag{2.24}$$

$$\mathbf{F}_y^* = K_{gm} S_x \tag{2.25}$$

Where,

$$S_x = -\frac{\frac{\partial \rho}{\partial x}}{\frac{\partial \rho}{\partial z}} \tag{2.26}$$

$$S_y = -\frac{\frac{\partial \rho}{\partial y}}{\frac{\partial \rho}{\partial z}} \tag{2.27}$$

$$S = \sqrt{S_x^2 + S_y^2} \tag{2.28}$$

In the model these velocities are added in the form of a combined GM and Redi diffusion mixing tensor given by (Redi, 1982; Griffies, 1998)

$$J = \begin{bmatrix} K_h & 0 & (K_h - K_{gm})S_x \\ 0 & K_h & (K_h - K_{gm})S_y \\ (K_h + K_{gm})S_x & (K_h + K_{gm})S_y & K_h S^2 \end{bmatrix} \tag{2.29}$$

Where K_h is the horizontal tracer mixing coefficient and K_{gm} is the thickness diffusion, given either as a constant or variable in space and time. Sensitivity to this parameter is studied and detailed in Chapter 4.

2.1.5.1 Tapering

To avoid large eddy induced velocities in regions of steep isopycnals, a tapering function suggested by Danabasoglu and McWilliams (1995) is also applied to these slopes as below,

$$f_1(S) = \frac{1}{2}\left(1 + \tanh\left[\frac{S_c - |S|}{S_d}\right]\right) \tag{2.30}$$

where the cutoff slope $S_c = 4 \times 10^{-3}$ and the slope scale S_d over which the tapering is applied is 1×10^{-3}. To further reduce the spurious sub grid scale eddy fluxes near the surface, an additional tapering as suggested by Large *et al.* (1997) as a function of height (z) is applied,

$$f_2(S) = \frac{1}{2}\left[1 + \sin\left(\pi\frac{z}{D} - \frac{\pi}{2}\right)\right] \tag{2.31}$$

where $D = \frac{c}{f|S|}$ with a first baroclinic wave speed $c = 2\,ms^{-1}$ and z is the depth.

2.1.6 Mesh

The model grid has unstructured triangular 2D elements with a structured 24 geopotential levels in the vertical (prismatic). The resolution in the vertical is fine near the surface and coarsens with depth [0, 20, 40, 60, 90, 120, 170, 250, 320, 430, 600, 750, 1000, 1200, 1500, 2000, 2500, 3000, 3500, 4250, 5000, 5750, 6500, 7000]. The model domain spans 10^oS to 82^oN in latitude and 98^oW to 15^oE in longitude. The model domain along with the 2D unstructured mesh and topography is shown in Figure-2.2. For the present preliminary study we have used a simplified North Atlantic domain with a smooth coastline and removed geographic features like the Mediterranean Sea and Hudson Bay.

The mesh comprises 55815 two dimensional elements (E_{2D}) and 28542 nodes (N_{2D}) with a total of 759994 three dimensional elements (E_{3D}) and 428166 (N_{3D}) nodes. The mesh has a minimum area of $20\,km^2$ mostly along the coast, in the Gulf Stream region, subpolar gyre and in regions of steep topography and a maximum area of $4400\,km^2$ towards the open ocean with a mean of $895\,km^2$ and a median of $645\,km^2$. The mesh was created using an open-source mesh generation package called BatTri (Bilgili *et al.*, 2006), which uses the popular package 'Triangle" (Shewchuk, 1996) in it's various steps of the mesh generation and refinement (Figure-2.3).

2.1.7 Boundary conditions

Buffer zones are implemented to deal with the open boundaries of the model. Tracer fields in the buffer zones are relaxed to the climatological field with an exponentially decreasing time scale from the boundary to the edge of the buffer zone (the time scale varies between experiments as detailed in Chapter 3.). Such an approach helps to achieve a low to a gradual strong restoring to the climatology at the open boundary and thus reduces the chances of blow up of the model simulation due to discontinuities arising between the model and climatology fields near the open boundary (buffer zone). A similar increase in the viscosity coefficient is implemented in this buffer zone to dampen any unrealistic reflection of waves from the boundary edge.

The model's surface boundary is then modified to accept atmospheric fluxes (heat and freshwater) rather than a climatological relaxed surface boundary. Fresh water fluxes includes river runoff from major rivers (Amazon, Orinoco, Mississippi, St. Lawrence and Congo Figure-2.4.) that are flowing into the Atlantic Ocean. The details on the treatment of rivers in the model is described in Chapter 3. A correction scheme to the net-heat fluxes at the surface is also added based on Barnier *et al.* (1995). The scheme and the results from the sensitivity study of this surface boundary condition are detailed in Chapter 3.

2.1.8 Boundary data

Annual 3-dimensional (x, y, z) climatological temperature and salinity were prepared from the World Ocean Atlas 2005 monthly climatological data set (WOA05) (Locarnini *et al.*, 2006; Antonov *et al.*, 2006) to initialize the model. The missing data points in WOA05 were filled by a cubic interpolation from neighboring points of the respective field. Monthly fields of surface fluxes (net-heat, freshwater flux and wind stress) were created from the European Center for Medium-range Weather Forecasts-40 year reanalysis (ERA40) data sets for the period of 1958 to 2000, which are then used for an annually periodic surface forcing of the model. Monthly fields of Sea Surface Temperature (SST) and Sea Surface Salinity (SSS) were also prepared from the WOA05 data for the surface relaxation scheme. River run off data set is from the Center for Sustainability and Global Environment, University of Wisconsin-Madison, is added to the freshwater flux in the model as point sources at river mouths (Figure-2.4).

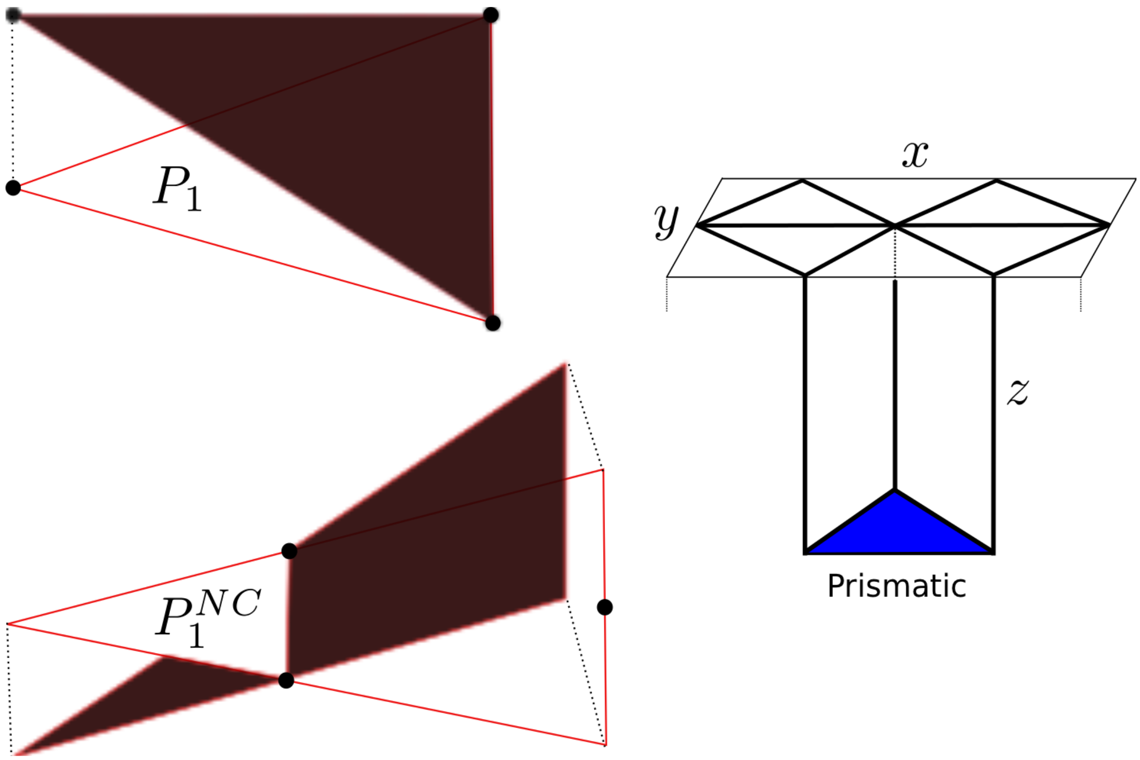

Figure 2.1: Schematic representation of P_1 and P_1^{NC} element shape functions and their prismatic view in vertical

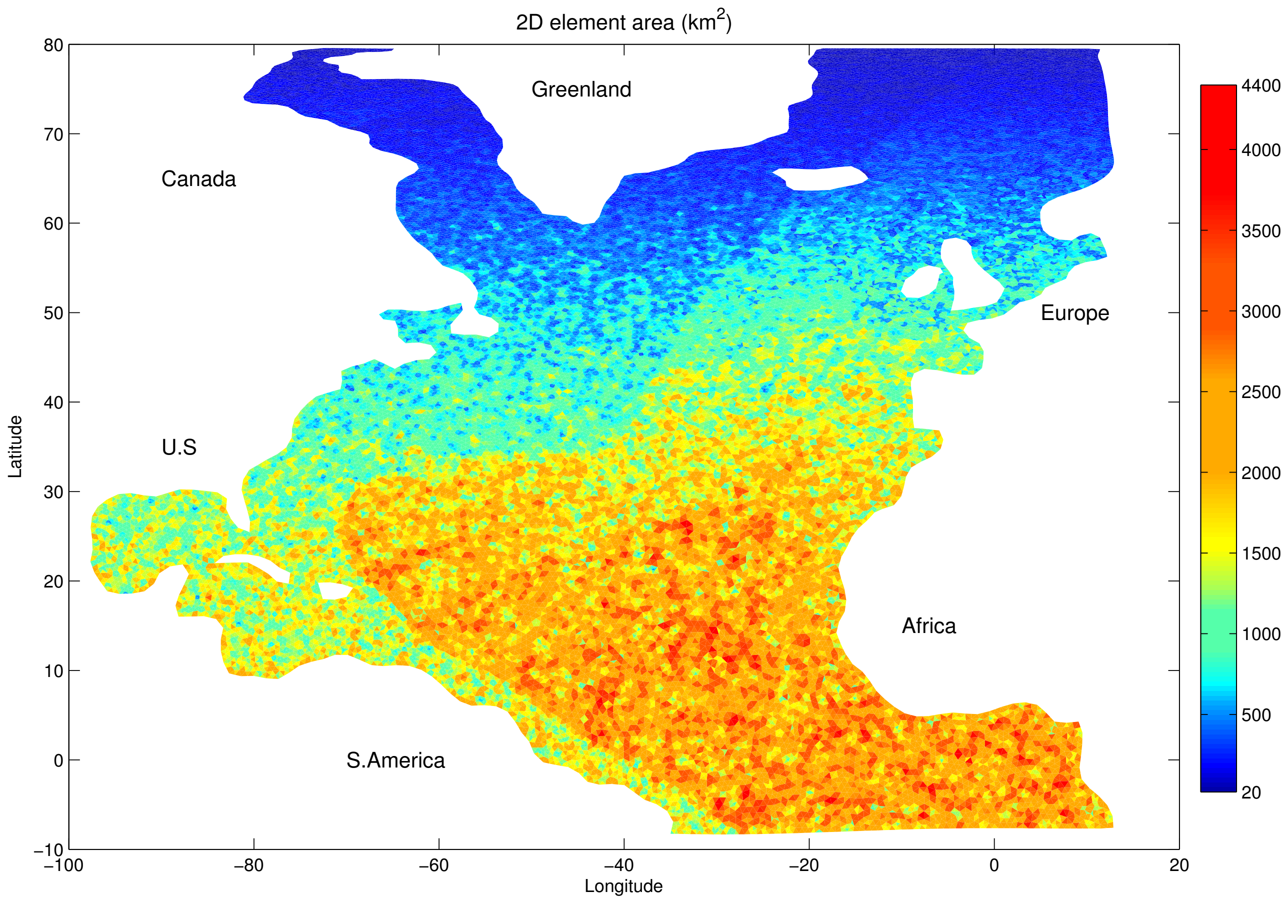

Figure 2.2: Model domain and finite element mesh resolution in km^2

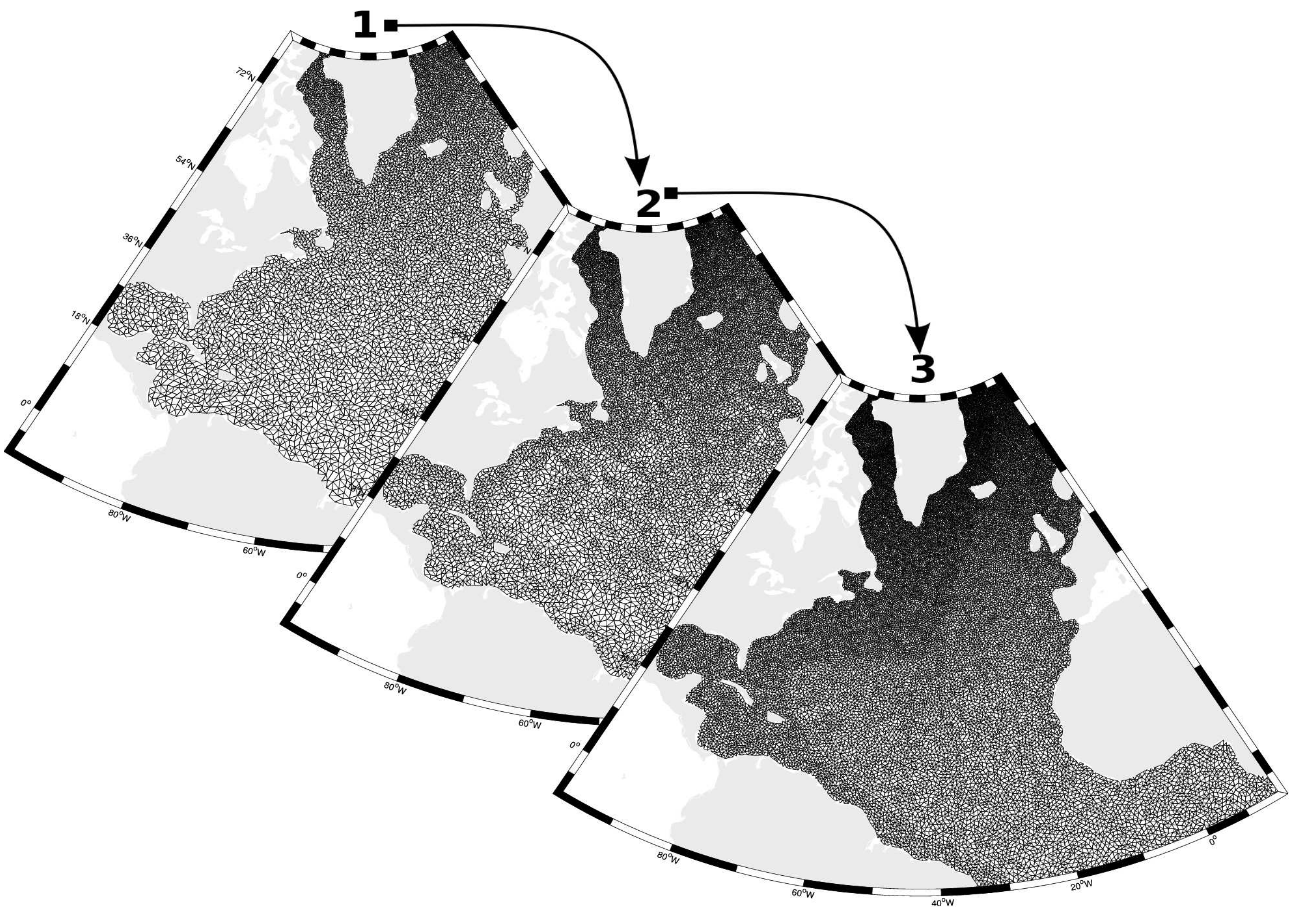

Figure 2.3: Steps in mesh generation and refinement. The coarser mesh produced in step-1 undergone refinement and produced an acceptable mesh for the study at step-3

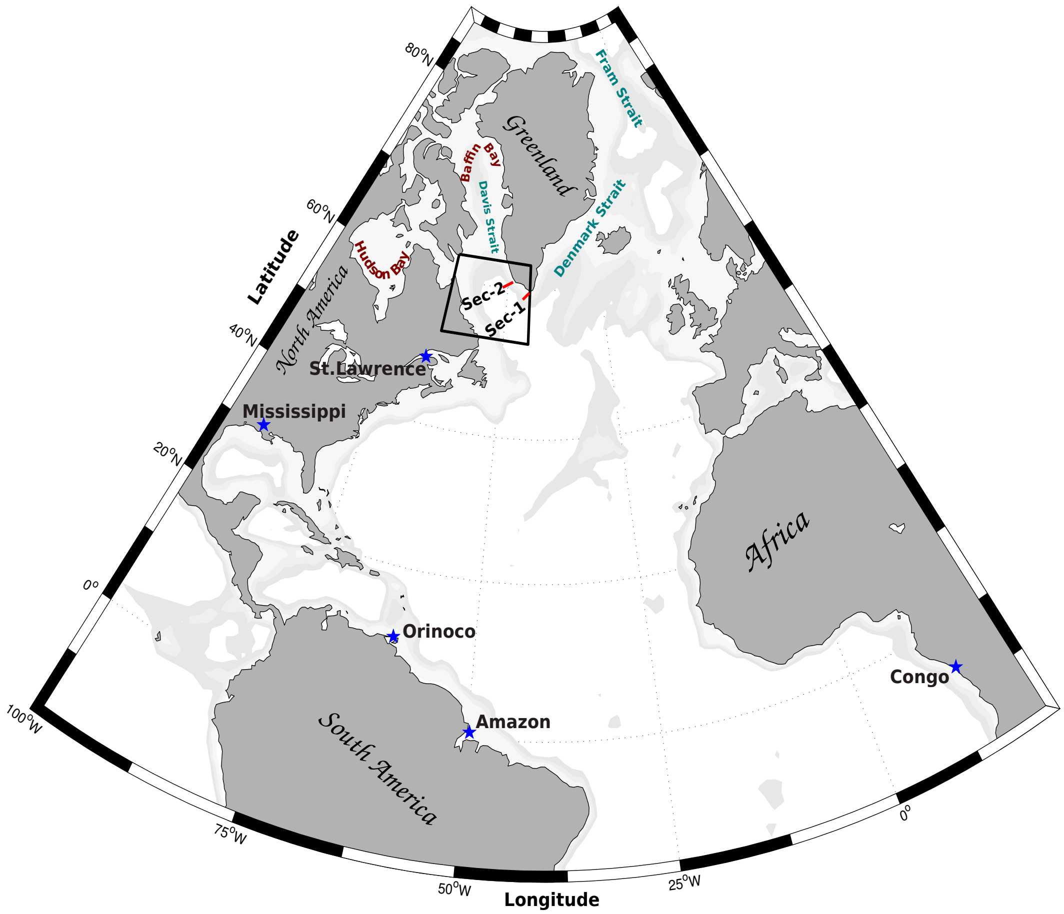

Figure 2.4: Input locations of river fluxes as well as transects (Sec-1 ⇒ Cape Farewell and Sec-2 ⇒ Cape Desolation) examined in the subpolar gyre, area inside the black box is considered as the Labrador Sea

Bibliography

Antonov, J.I., R.A. Locarnini, T.P. Boyer, A.V. Mishonov and H.E. Garcia (2006). World Ocean Atlas 2005. *Ed. NOAA Atlas NESDIS 62, U.S Government Printing Office, Washington, D.C.* **2: Salinity. S. Levitus**, 182.

Barnier, B., L. Siefridt and P. Marchesiello (1995). Thermal forcing for a global ocean circulation model using a three year climatology of ECMWF analyses. *Journal of Marine Systems* **6**, 363–380.

Bilgili, Ata, Keston W. Smith and Daniel R. Lynch (2006). BatTri: A two-dimensional bathymetry-based unstructured triangular grid generator for finite-element circulation modeling. *Computers Geosciences* **32**, 632–642.

Danabasoglu, Gokhan and James C. McWilliams (1995). Sensitivity of the global ocean circulation to parameterizations of mesoscale tracer transports. *Journal of Climate* **8**(12), 2967–2987.

Danilov, S., G. Kivman and J. Schroter (2004). A finite-element ocean model: principles and evaluation. *Ocean Modelling* **6**, 125–150.

Danilov, S., G. Kivman and J. Schroter (2005). Evaluation of an eddy-permitting finite-element ocean model in the North Atlantic. *Ocean Modelling* **10**, 35–49.

Gent, Peter R., Jurgen Willebrand, Trevor J. Mc Dougall and James C. McWilliams (1995). Parameterizing eddy-induced tracer transports in ocean circulation models. *Journal of Physical Oceanography* **25**, 463–474.

Griffies, Stephen M. (1998). The Gent-McWilliams Skew Flux. *Journal of Physical Oceanography* **28**, 831–841.

Hanert, Emmanuel, Daniel Y. Le Roux, Vincent Legat and Eric Deleersnijder (2005). An efficient Eulerian finite element method for the shallow water equations. *Ocean Modelling* **10**, 115–136.

Jackett, David R. and Trevor J. McDougall (1995). Minimal Adjustment of Hydrographic Profiles to Achieve Static Stability. *Journal of Atmospheric and Oceanic Technology* **12**, 381–389.

Large, William G., Gorkhan Danabasoglu, Scott C. Doney and James C. Mc Williams (1997). Sensitivity to Surface Forcing and Boundary Layer Mixing in a Global Ocean Model: Annual-Mean Climatology. *Journal of Physical Oceanography* **27**, 2418–2447.

Locarnini, R.A., A.V. Mishonov, J.I. Antonov, T.P. Boyer and H.E. Garcia (2006). World Ocean Atlas 2005. *Ed. NOAA Atlas NESDIS 62, U.S Government Printing Office, Washington, D.C.* **1: Temperature. S. Levitus**, 182.

Pacanowski, R.C. and S.G.H. Philander (1981). parameterization of Vertical Mixing in Numerical Models of Tropical Oceans. *Journal of Physical Oceanography* **11**, 1443–1451.

Redi, Martha H. (1982). Oceanic isopycnal mixing by coordinate rotation. *Journal of Physical Oceanography* **12**, 1154–1158.

Shewchuk, Jonathan Richard (1996). Triangle: Engineering a 2D Quality Mesh Generator and Delaunay Triangulator. In: *Applied Computational Geometry: Towards Geometric Engineering* (Ming C. Lin and Dinesh Manocha, Ed.). Vol. 1148 of *Lecture Notes in Computer Science*. pp. 203–222. Springernegativerlag. From the first ACM Workshop on Applied Computation Geometry.

Wang, Q., S. Danilov and J. Schroter (2008). Finite element ocean circulation model based on triangular prismatic elements, with application in studying the effect of topography. *Journal of Geophysical Research*.

Chapter 3

Impact of surface boundary flux forcing in FEOM

This chapter details the impact of a corrected surface boundary flux in FEOM. The results are compared with a Control Simulation (CS) and available observations in the area.

Three simulations were performed in this study (Figure-3.1 and Table-3.1). The first one is a Control Simulation (CS), where the model is initialized from a climatological temperature and salinity derived from WOA05 and a stationary state ($u = 0$, $v = 0$). At the surface the model is forced with the monthly climatological wind stress derived from ERA40 along with a 2 day relaxation to WOA05 climatological temperature and salinity. In the buffer zone this time scale for the entire water column decreases exponentially from 2 day to $\frac{1}{2}$ day away from the the boundary edge. The simulation is performed for 10 model years.

The second experiment is a Flux Simulation (FS) with same initial condition as that of the CS run. Instead of a climatology relaxed surface boundary, heat and fresh water flux forcings from ERA-40 monthly climatology are applied at the surface. Additional to this, a freshwater influx from major rivers (http://www.sage.wisc.edu/riverdata/) that are flowing into the North Atlantic Ocean are added. This includes the following major rivers: Amazon, Orinoco, Mississippi, St. Lawrence and Congo Figure-2.4. The monthly climatological river influx is incorporated as a freshwater point source into the salinity conservation equation (eq-2.12), in a way that, 60% of the total river flux goes into the first layer and 40% into the next layer below at their respective discharge locations in the model. As flux forced models often drift (Thompson *et al.*, 2007), a surface relaxation to the climatological temperature and salinity is still applied, with a 20 day time scale. Here the buffer zone relaxation time scale decreases exponentially from 20 days to 0.5 days as before.

The third experiment is a Corrected Flux Simulation (CFS) with the same initial condition as that of CS/FS case. However with a corrected surface heat flux scheme (Barnier *et al.*, 1995).

3.1 Control simulation (CS)

The model soon reaches a quasi-equilibrium state after the 2^{nd} year of the simulation (Figure-3.2). The oscillations in the mean kinetic energy plot (Figure-3.2) arise from the seasonal variability in the model wind forcing. Figure-3.2 shows that The results from the 10^{th} year of the control simulation are shown in Figures-3.3 to 3.12. The mean temperature field at 40 m depth (Figure-3.3.a) and the difference from the observation (WOA05) are shown in Figure-3.3.b. Salinity fields of the same simulation (Figure-3.3.c) and the difference from the climatology (WOA05) are shown in Figure-3.3.d. The largest differences in this run for both the temperature and salinity fields from the climatology are mainly near the coast of Newfoundland (Figure-3.3.b) with an increase of more than 5^oC in temperature on the western side and a decrease of 4^oC on the north-eastern side of the Gulf Stream. At the same time an increase of 2.2 units in salinity from the observation is also observed near the Newfoundland coast (Figure-3.3.d) and 1 unit decrease on the north-eastern side of the Gulf Stream. These differences arise from the lack of small scale features in the forcing data derived from the World Ocean Atlas (WOA), as well as the Gulf Stream's poor separation, leading to a lack of cold cyclonic circulation in the Mid-Atlantic Bight.

Figure-3.4a,d shows the comparison of the meridional average temperature and salinity to the observations. The basic model structure is comparable to the observations, although the gradients are too diffusive. This may be attributed to the simple horizontal mixing along z-coordinates used. Another major difference in the plots (Figure-3.4) is the absence of a high temperature and salinity tongue around $40^0 N$, caused by the lack of a Mediterranean Sea and the associated outflow in the model configuration.

Freshwater content (FW) in the model is calculated as follows,

$$FWC = \int_V \frac{S_r - S}{S_r} dV \tag{3.1}$$

here S_r is the reference salinity of 35.0 units, S is the model salinity and V is the volume of the Labrador Sea ($53^o N - 63^o N$ and $65^o W - 44^o W$). The results are shown in Figure-3.5 (dash line). Even though the beginning years of the model show a steady drift in the freshwater content in the Labrador Sea, later an equilibrium is reached after the model's 6^{th} year. Mean winter (January, February and March) mixed layer depth (MLD) is calculated for the 10^{th} model year based on a σ_t criteria of 0.02 (Figure-3.6) as explained in the Appendix. A maximum of around 300 m is observed in the Labrador sea (Figure-3.6.a), which is far too shallow compared to the observations, associated with a lack of deep convection in the basin.

The model's 10^{th} year mean sea surface height (SSH) from the CS run is shown in Figure-3.7.a. This shows an expected low sea surface height (0.8 m) in the interior of the Labrador Sea and a high in the western boundary (0.6 m) of the subtropics (Ferry and Reverdin, 2000). The low sea surface in the Irminger and Labrador Seas are well captured in this run. The high resolution mesh near the Gulf Stream region is able to represent aspects of the Gulf Stream separation in this simulation and can be improved further by using a better horizontal mixing parameterization scheme that can preserve the gradients in the frontal regions.

The mean boundary currents around Greenland and in the interior of the Labrador sea (Figure-3.8 a, d) are represented in this simulation with reasonable West Greenland Current (WGC) (Figure-3.9.a), East Greenland Current (EGC) (Figure-3.9.g) and Labrador Current (LC) (Figure-3.9.j) strengths leading to an annual mean barotropic stream function of 10 Sv in these regions.

However the eastward separation of the EGC around Jan Mayen Fracture Zone as found by Hopkins (1991) and Bourke *et al.* (1992) is poorly represented in this experiment (Figure-3.8.a).

The mean barotropic stream function of the 10^{th} year of this run is presented in Figure-3.10.a The strength and distribution of the stream function are reasonable with a minimum of -38 Sv in the subpolar gyre and a maximum of 40 Sv in the subtropical gyre. Figure-3.11.a shows the annual mean Meridional Overturning Streamfunction(MOC) for the 10^{th} year. Here the unstructured data were re-gridded onto a regular grid of $\frac{1}{4}^{o} \times \frac{1}{4}^{o}$ resolution before the stream function calculation. The stream function values are weak in this simulation compared to other model studies and observations in this area (Chassignet *et al.*, 2000; Beismann and Barnier, 2004). A maximum of 14 Sv is observed in the Ekman layer, which is consistent with the previous studies in the North Atlantic (Beismann and Barnier, 2004) (Figure-3.11.f), but only 6 Sv around 1000m depth.

To analyze the boundary currents in the model, vertical sections in the West Greenland current (WGC) region were compared with the International Council for the Exploration of the sea (ICES) TULUGAQ cruise data set (Ribergaard, 2006) taken during the cruise carried out in July, 2000 (Buch and Nielsen, 2000). Two major sections in WGC at Cape Farewell (Sec-1) and Cape Desolation (Sec-2) are taken for the analysis (Figure-2.4). 10^{th} year volume transport for these two sections are shown in Figure-3.9 with a mean transport of 2.7±0.50 Sv at Cape Farewell and 2.7±0.80 Sv at Cape Desolation (Table-3.2) which is comparable to that of Myers *et al.* (2009) (Table-3.2). Here the 34.8 isohaline is selected as the offshore edge of the WGC as in Myers *et al.* (2009). The decrease in magnitude is due to the early turning of WGC into the Labrador Sea than reality.

The model's vertical temperature (Figure-3.12.a,e) and salinity (Figure-3.12.i,m) along these sections are also compared with the available observational data sets for the summer months (June-July)(Figure-3.12.d,h and l,p). To ease the comparison, a land mask based on the model topography has been applied to the ICES data. The drift in hydrography can clearly be seen in these figures. Both Cape Farewell (Figure-3.12.a) and Cape Desolation (Figure-3.12.e) sections shows too much cold water transport near the boundary, as well as a lack of Irminger water at mid-depth (Figure-3.12.d,c). However a freshening is observed in near surface waters and a salinification around 700m (Figure-3.12.i,m). This may be attributed to the poor surface boundary conditions in the model and will be discussed more in the following sub-sections.

3.2 Surface heat and freshwater flux incorporated simulation (FS)

Flux forcing introduced new drifts in the representation of the model's hydrography. 2D temperature fields (Figure-3.3.e) and their difference from the observation (WOA05) (Figure-3.3.f) of this run is shown in Figure-3.3. Nearshore of Newfoundland and Labrador Sea, shows an increase of more than 6^oC in the FS simulation and a decrease of 6^oC on the eastern side of the Gulf Stream. According to Barnier *et al.* (1995) this is associated with the error in the heat fluxes over Gulf Stream area in winter and they found a correction of 30 to 55 $Wm^{-2}K^{-1}$ is needed. However an overall decrease in the near surface temperature in subtropical and subpolar gyre is also observed.

2D salinity fields (Figure-3.3.g) and their difference from the climatology (WOA01) (Figure-3.3.h) of this run are shown in Figure-3.3. The error in salinity around Amazon river is reduced to 0.5 units. The subtropical gyre and Nordic sea region shows additional drift from the CS case. As in the CS case the vertical structure of the tracer fields are more diffusive in the horizontal (Figure-3.4.b,e) compared to the initial condition (Figure-3.4.g,h).

Even though the fresh water content in the Labrador Sea showed a decreasing trend in the beginning years of the model simulation, a slow rebound from the CS case is evident in Figure-3.5. The MLD in the model is improved from the CS case (Figure-3.6.b) with an increase of 400m in the subpolar gyre with a core in the Labrador Sea and Irminger Sea. This bias in the Irminger Sea has been previously observed with WOA data sets (Schott *et al.*, 2009).

Mean Sea Surface Height from the 10^{th} year of this run is shown in Figure-3.7.b. The expected low sea surface (0.8 m) in the subpolar gyre is now seen through the Irminger Sea to the Labrador Sea. A core of low sea surface (0.8 m) is seen in the Nordic Seas. The magnitude of the low and high SSH (subpolar and subtropic regions) is improved, with a region of low sea surface extending to the tip of Florida compared to the CS case, leading to a better Gulf Stream separation in the model (Figure-3.7.b).

The barotropic stream function for the FS simulation is shown in Figure-3.10.b. The transport is enhanced by 2 Sv (in the subpolar gyre) from the CS case and also by 2 Sv in the western boundary current of the subtropical gyre (Figure-3.10.d). Overall the stream function values were improved, a direct result of strong currents in these two regions (Figure-3.8.b).

The model's MOC is shown in Figure-3.11.b. An increase of 3 Sv from the CS case is observed around 1000m between $30^o N$ to $60^o N$, with an increase of 3 Sv above 1000m extending to the surface layer near the equator (Figure-3.11.d). Overall the maximum transport and it's location is closer to the previous studies carried out in the North Atlantic with a range of 13-15 Sv (Beismann and Barnier, 2004; Chassignet *et al.*, 2000; Danilov *et al.*, 2005; Schmitz and McCartney, 1993).

The volume transport at Cape Farewell (Figure-3.9.a) and Cape Desolation (Figure-3.9.b) shows an amplified seasonality compared to the CS case. The mean transport at these sections slightly increased from the CS case to $2.8 \pm 1.1\,Sv$ and $2.7 \pm 1.3\,Sv$ respectively (Table-3.2). Moreover the tracer fields in these sections show more similarity with the ICES data (Figure-3.12). At Cape Farewell the inverted temperature stratification in the CS case (Figure-3.12.a) is removed as the model now forms Labrador Sea water (if too shallow) (Figure-3.12.b) becoming closer to the ICES data (Figure-3.12.d). The salinity stratification in this section is also improved. Relatively more saline Irminger waters compared to the CS case are now simulated as in the ICES data (Figure-3.12.l). This is the same for the Cape Desolation section (Figure-3.12.n). Even though the model lacks many small scale features from the ICES data (Figure-3.12.h), a better tracer field is obtained in this run compared to the CS case.

Over all the flux forcing in the model improved the hydrography but still corrections to the fluxes are needed to improve the tracer fields, which is detailed in the next sub-section.

3.3 Flux Corrected simulation (CFS)

The importance of a feedback from the state of the sea onto the flux forcing at the surface boundary in a General Ocean Circulation Model (OGCM) was examined by Barnier (Barnier *et al.*, 1995). Here I included this feedback into the model forcing, one step towards the coupling with an atmosphere/sea ice model and representing a realistic surface boundary condition. The model used an initial state identical to that of the CS case and with a similar setup as that of the FS case except with an added net-heat flux correction (Barnier *et al.*, 1995).

The forcing term (F) on the right hand side (R.H.S) of the temperature conservation equation (eq-2.12) becomes (Barnier *et al.*, 1995),

$$F = \frac{Q_{net}}{\rho_o C_{PW}} + \frac{dQ}{dT^s_{clim}} \frac{(T^s_{model} - T^s_{clim})}{\rho_o C_P} \tag{3.2}$$

where $\frac{dQ}{dT^s_{clim}}$ is given by

$$\frac{dQ}{dT^s_{clim}} = \underbrace{-4\epsilon\sigma(T^s_{clim})^3}_{Infrared} - \underbrace{\rho_a C_P C_H U_{10}}_{Sensible} - \underbrace{\rho_a C_E L U_{10} 2353\, ln(10) \times \left(\frac{q^s_{clim}}{(T^s_{clim})^2}\right)}_{Latent} \tag{3.3}$$

where T^s_{model} and T^s_{clim} are the model and climatological sea surface temperature respectively. Q_{net} and SST are the climatological net-heat (Wm^{-2}) and sea surface temperature(^oC) respectively. ρ_a is the air density in kg m^{-3}. The Emissivity coefficient is $\epsilon = 0.98$, Stefan-Boltzmann constant $\sigma = 5.67 \times 10^{-8} J\, s^{-1} m^{-2} K^{-4}$, specific heat at constant pressure for air $C_P = 1.0048 \times 10^3 J\, kg^{-1} K^{-1}$,specific heat at constant pressure for sea water $C_{PW} = 4.18 \times 10^3 J\, kg^{-1} K^{-1}$, Bulk transfer coefficient for sensible heat $C_H = 1 \times 10^{-3}$, 10m wind speed $U_{10}(ms^{-1})$, Bulk transfer coefficient for latent heat $C_E = 1.15 \times 10^{-3}$, Latent heat of vaporization $L = 2.508 \times 10^6 J\, kg^{-1}$ and the monthly climatological saturated air specific humidity $q^s_{clim}\,(g\, kg^{-1})$.

The first term on the R.H.S of the equation (3.3) comprises the contribution from the infrared radiation, the second term from the sensible heat and the last term from the latent heat. Since the net incoming solar heat flux at the ocean surface should not depend on the model SST, the contribution onto the incoming solar radiation is zero (Barnier *et al.*, 1995). For consistency, all the data needed for the above correction term is taken from ERA-40 data. More details on the scheme are given in the Appendix.

Monthly mean net heat correction (second term on the R.H.S of equation-3.2) from the 10^{th} model year is shown in Figure-3.13. Major corrections are needed near the Gulf Stream region with more focus on the winter months. The 2D temperature field at depth 40m (Figure-3.3.i) and their difference from the observations (WOA05) is shown in Figure-3.3.j. The net-heat correction reduced the difference in temperature on the east side of the Gulf Stream region to 2^oC as well as to the north in Baffin Bay and east of Greenland. 2D salinity fields were also presented in the same figure for the model (Figure-3.3.k) and deviations from the observation (Figure-3.3.l) with minor differences from FS case. Freshwater content in the Labrador Sea shows a similar trend that of FS case (Figure-3.5) with fractional variations in magnitude.

The model's mean barotropic streamfunction is shown in Figure-3.10.c with minor improvement from the FS case, close to Smith *et al.* (2000). Both FS and CFS experiments shows an improved eastward separation of the EGC around the Jan Mayen Fracture Zone (Hopkins, 1991; Bourke *et al.*, 1992) and similar boundary currents in the subpolar region as that of the CS. The improvement can be observed in the mean Sea Surface Height (SSH) of the model (Figure-3.7.c,e). The expected low SSH (0.8 m) in the subpolar gyre in the Labrador Sea and Irminger Sea is evident. A high SSH of 0.6 m is observed in the western boundary of the Subtropical gyre and the northward extent of the low sea surface towards the Nordic sea is also better represented. However the magnitude is smaller compared to the high resolution modelling study of Malone *et al.* (2003).

The model's MOC is shown in Figure-3.11.c. An increase of 3 Sv from the CS case is observed around 1000m between 30^oN to 60^oN, with an increase of 3 Sv above this in the Ekman layer (Figure-3.11.d) which is closer to the FS case. The weak negative return stream function at lower depths near the southern boundary is due to the lack of an open boundary at that location. The MLD in the model is improved from the CS case (Figure-3.6.b) and to a small extent from the FS case with an increase of 400m in the subpolar gyre with maximums in the Labrador Sea and the Irminger Sea. Overall the CFS case simulated a better hydrography of the North Atlantic compared to the CS case and to some extent from the FS case.

The model's 10^{th} year annual mean meridional heat transport for each latitude (ϕ) with individual zonal cross sectional area of A is calculated as below,

$$HT = \rho_0 C_{pw} \int_A \overline{v}\overline{T} dA \tag{3.4}$$

where C_{pw} is the specific heat at constant pressure for water ($4186 Jkg^{-1}k^{-1}$), $\overline{v}$ and T are the mean meridional velocity and temperature respectively. The weak northward component of the MOC (Figure-3.11) leads to the dip in the meridional heat transport around mid latitudes (Figure-4.24).

The volume transport at Cape Farewell (Figure-3.9.a) and Cape Desolation (Figure-3.9.b) shows similar magnitudes in the beginning months of the 10^{th} year of the simulation and then diverts by a small magnitude in later months. The mean transports at these sections are $2.6 \pm 1\,Sv$ and $2.5 \pm 1.3\,Sv$ respectively, which is not much different from the FS case and Myers *et al.* (2009)(Table-3.2). Tracer fields (Figure-3.12.c,g,k,o) in these sections shows minor differences from the FS case and is closer to the ICES data.

3.4 Summary and Discussion

The results from the control simulation showed many discrepancies from observational data sets. These discrepancies are mainly caused by the simplified configuration of the model setup and were observed in all the three experiments. The spreading of the tracers in the horizontal direction (Figure-3.3,3.4) is the direct consequence of the simplified constant horizontal Laplacian mixing in the model. This could be improved by activating the sub-grid scale GM eddy parameterization scheme (Gent *et al.*, 2002) in the model, which improves the gradients near the frontal regions. The observed drift in the hydrography is improved to some extent by better forcings in the third simulation with a corrected air-sea flux.

The addition of the flux forcing into the model introduced some new discrepancies in the model result (FS case). This includes the shifting North Atlantic current in the subtropics (Figure-3.7.b) and an increase in the near surface temperatures between Newfoundland and the Gulf Stream, whereas the temperature decreased in the subtropical gyre (Figure-3.3:d and 3.3:f). Similar discrepancies were also observed in the case of the near surface salinity, with an increased salinity in the interior of the Labrador sea and a decrease in most areas of the subtropical gyre (Figure-3.3:d and 3.3:f).

These differences might be caused by errors in the heat flux as noted by Barnier *et al.* (1995) and can be improved by a correction to the fluxes that incorporates the feed back from the sea state. This approach is included in the CFS case, which gave more degrees of freedom to the model by replacing the surface nudging of climatological temperature to a net-heat correction scheme. The simulation results are a little closer to the observation than for the FS case, for both the near surface temperature (Figure-3.3.j) and salinity (Figure-3.3.l). The Gulf Stream separation and the drift in salinity and temperature in the interior of the Labrador sea were improved as well. The MLD in the model were also improved (Figure-3.6.b,d), with some discrepancies in the Irminger Sea as noted in previous studies (Schott *et al.*, 2009).

Addition of the river runoff directly into the model improved the salinity distribution at the major river discharge locations (Figure-3.3: k, l). Salinity around the Amazon river mouth is improved. This could be improved by using more river data, by introducing a better refined mesh near river mouths as well as including an open boundary condition north of Baffin Bay and the Nordic seas. At the same time the freshwater content in the Labrador Sea showed a slow rebound from its beginning years of drift trend and also from the CS case (Figure-3.5), although the improvement is small. The strength of the WGC is reasonable (Figure-3.9) but weak compared to Myers *et al.* (2009).

Figure 3.1: Experiment diagram of the three simulations (CS, FS and CFS)

The mean barotropic stream function for all these three simulations is presented in Figure-3.10. The overall improvements in the subtropics and subpolar gyre regions are clearly seen in the CFS (Figure-3.10.e) compared with the CS. The maximum and minimum locations and the magnitudes of the stream function are improved and is closer to the high resolution model study of Smith *et al.* (2000). The MOC of the model (for the CFS case) is reasonably close to the recent studies carried out in the North Atlantic (Chassignet *et al.*, 2000; Danilov *et al.*, 2005), even given the absence of any special treatment for the bottom topography or a further refinement in the mesh.

The lack of small scale features in the WOA data set were balanced by the addition of a better net-heat flux data set in the FS case. At the same time the correct flux in the CFS case improved both the small scale features and to some extent removed the drift introduced by the flux forcing in the model. All these improvements were obtained by just using a better boundary condition data set in the model. Thus this study shows that the simple configuration of prismatic $P1^{nc} - P1$ version of the Finite Element Ocean Model (FEOM) with its corrected flux forcing was successful in reproducing some aspects of important hydrographic features of the North Atlantic Ocean, which are crucial for any successful ocean general circulation model simulation.

Experiments	**Initialization**	**Surface forcing**	**Relaxation time scale**
Control Simulation (**CS**) (10-year)	T and S climatology (WOA05), Stationary state and flat sea surface	ERA40 wind stress, nudging towards T and S climatology (WOA05)	2 days
Flux Simulation (**FS**) (10-year)	””	ERA40 net-heat flux, E-P flux and wind stress, additional nudging towards T and S climatology (WOA05) and river flux	20 days
Corrected Flux Simulation (**CFS**) (10 -year)	””	ERA40 net-heat flux with correction, E-P flux and wind stress, additional nudging towards salinity climatology (WOA05) and river flux	20 days

Table 3.1: Details of the three model simulations (CS, FS and CFS)

Section	**CS**	**FS**	**CFS**	**Myers *et al.*, 2009**
Cape Farewell (Sec-1) (in Sv)	2.7 ± 0.5	2.8 ± 1.1	2.6 ± 1	$3.2 \pm 2.3\, Sv$
Cape Desolation (Sec-2) (in Sv)	2.7 ± 0.8	2.7 ± 1.3	2.5 ± 1.3	$5.5 \pm 3.9\, Sv$

Table 3.2: 10^{th} year annual mean volume transport and it's standard deviation (in Sv) across Cape Farewell and Cape Desolation sections for CS, FS and CFS simulations compared to Myers *et al.*, 2009

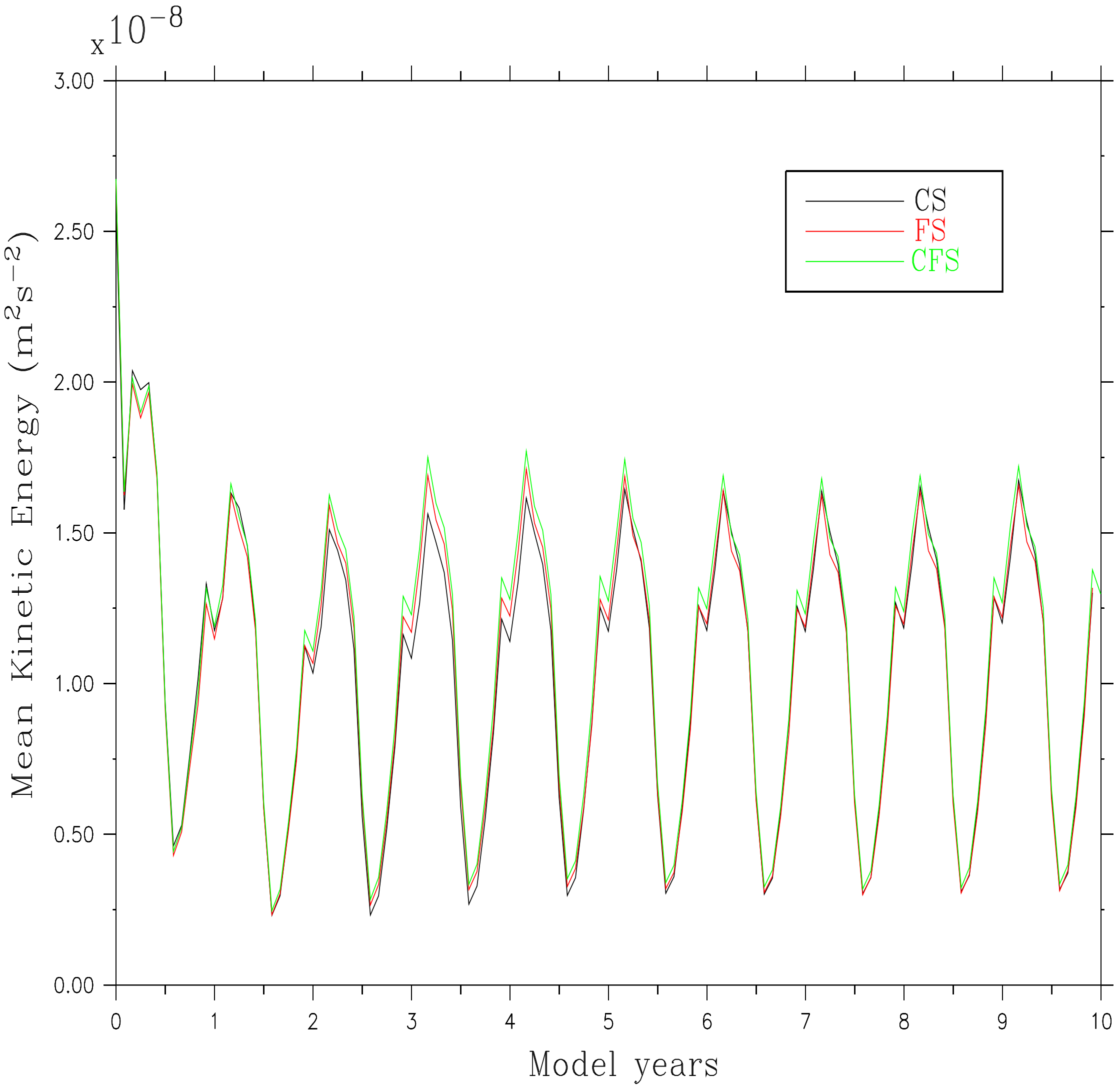

Figure 3.2: Time series of model's Mean Kinetic Energy (MKE $= \frac{u^2+v^2}{2}$) for simulations; CS (dash line), FS (solid line) and CFS (solid square)

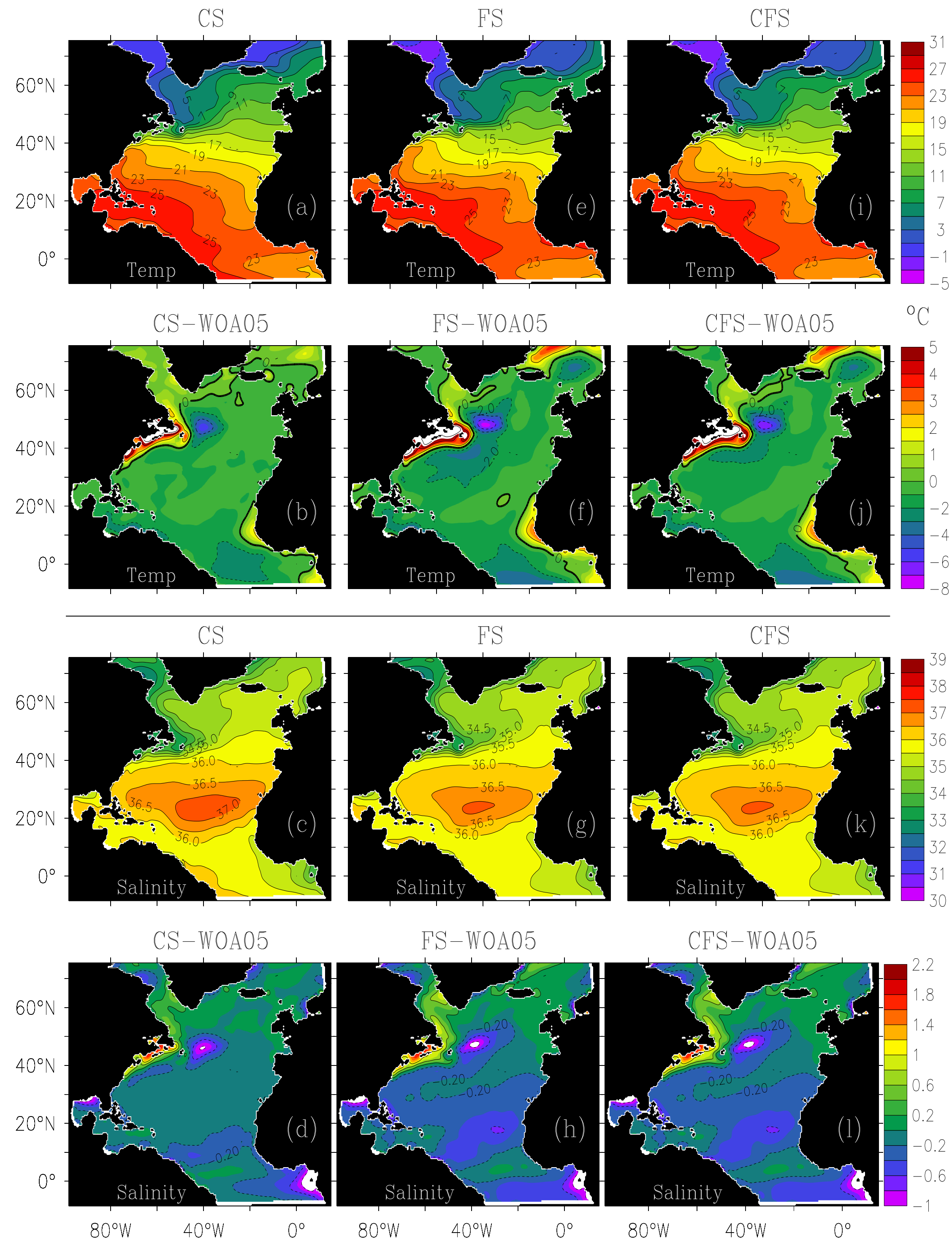

Figure 3.3: 10^{th} year temperature and salinity fields at 40m depth of CS, FS and CFS in 1^{st} and 3^{rd} row and corresponding differences from the WOA05 climatology, in the 2^{nd} and 4^{th} row respectively.

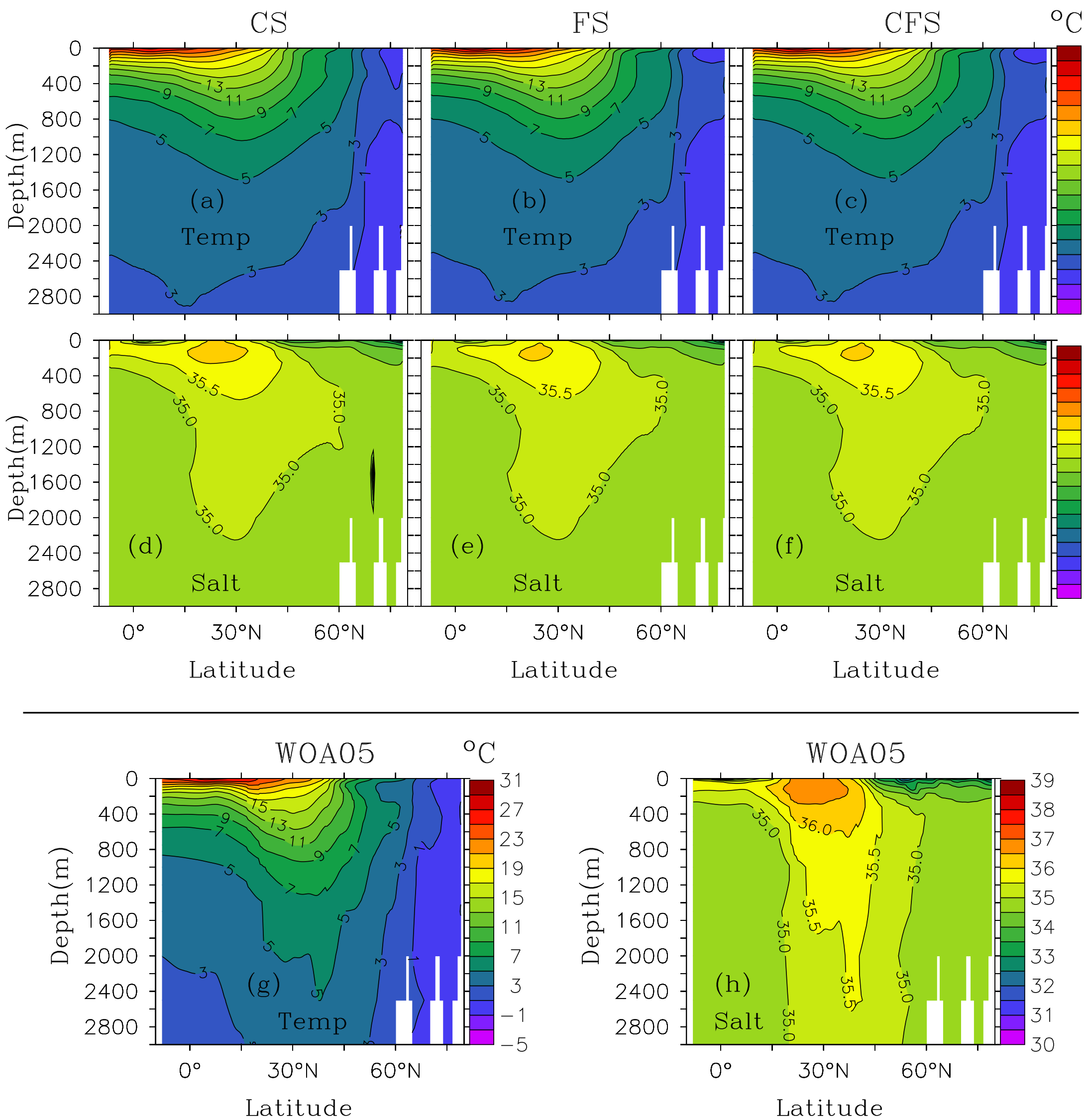

Figure 3.4: Meridional average temperature from the 10^{th} year of CS(a), FS(b), CFS(c) cases and salinity (d,e,f), in top panels. Meridionally averaged WOA05 temperature (g) and salinity (h) in bottom panels.

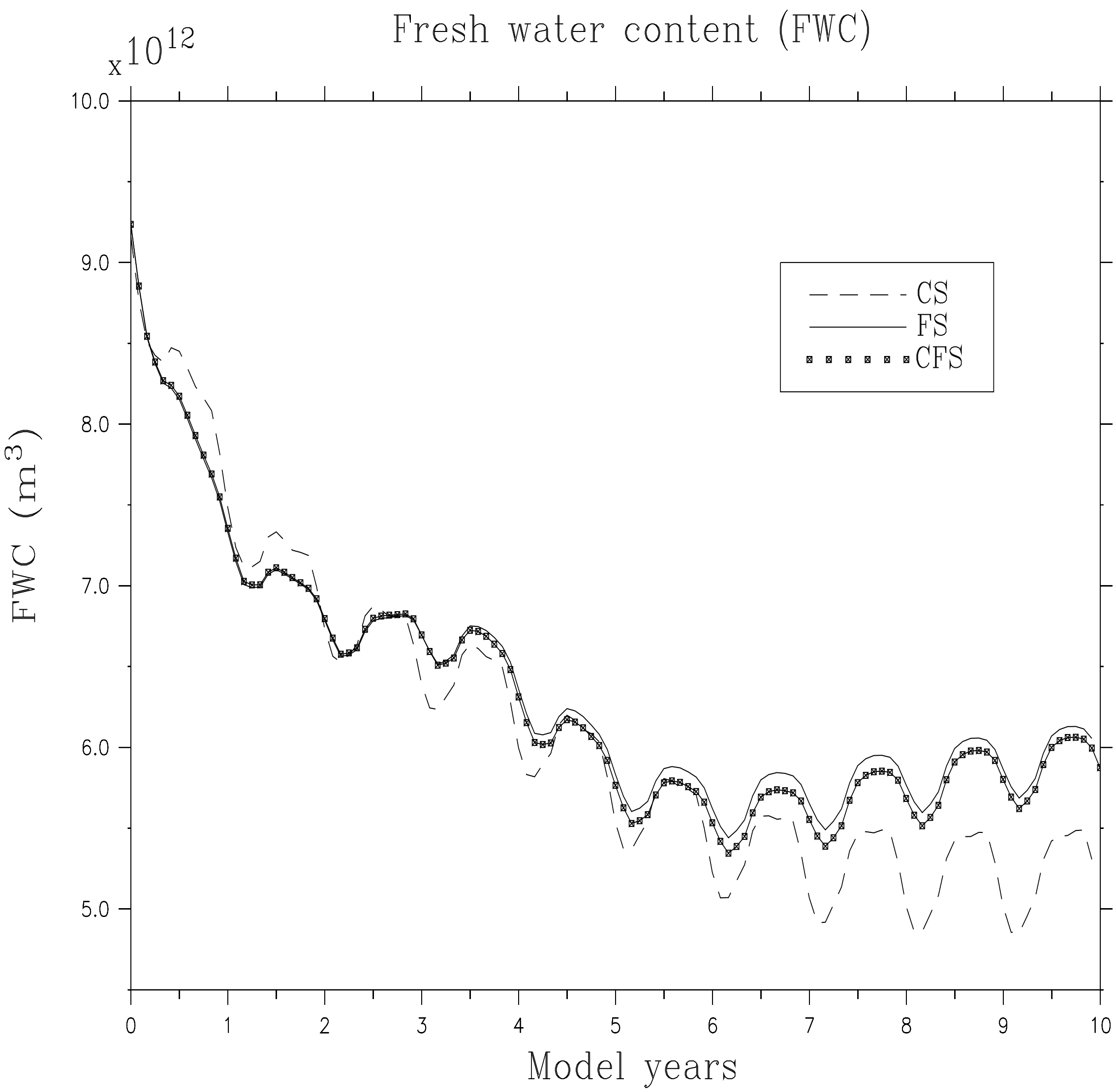

Figure 3.5: Freshwater content of CS (dash line), FS (solid line) and CFS (solid square) for the Labrador Sea ($53^oN - 63^oN$ and $65^oW - 44^oW$)

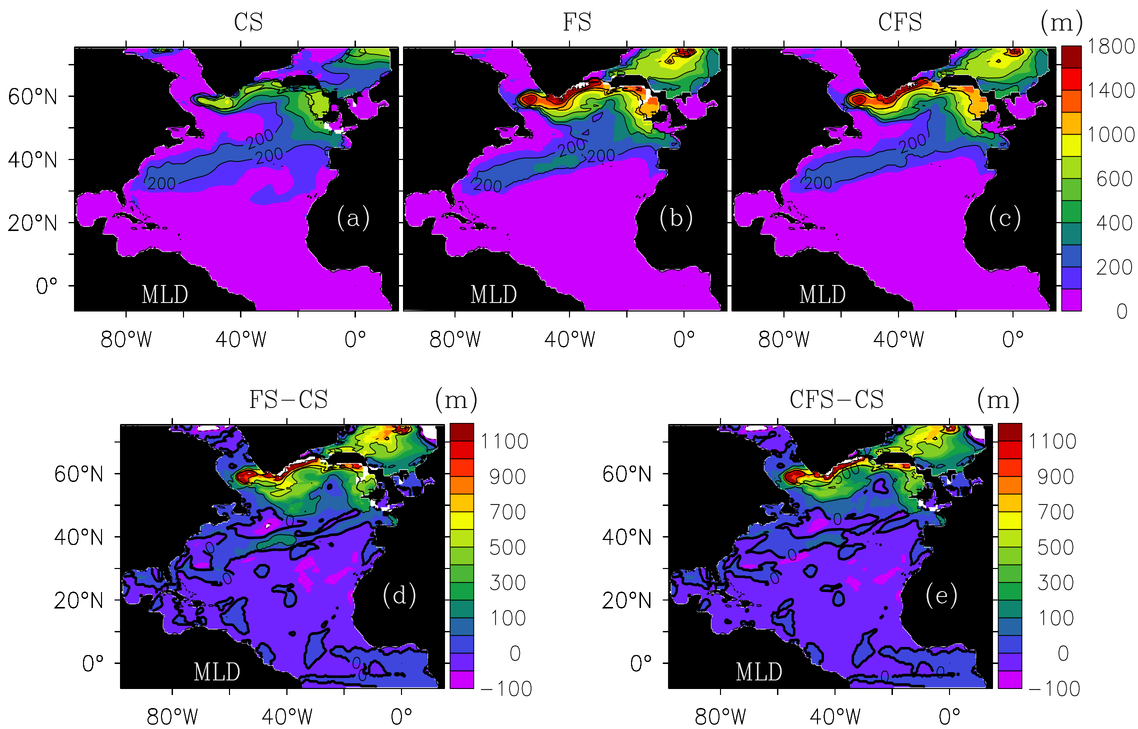

Figure 3.6: Mean winter (JFM) mixed layer depth (MLD) in meters from the 10^{th} year of the CS (a), FS(b), CFS(c) and their difference from CS in (d,e)

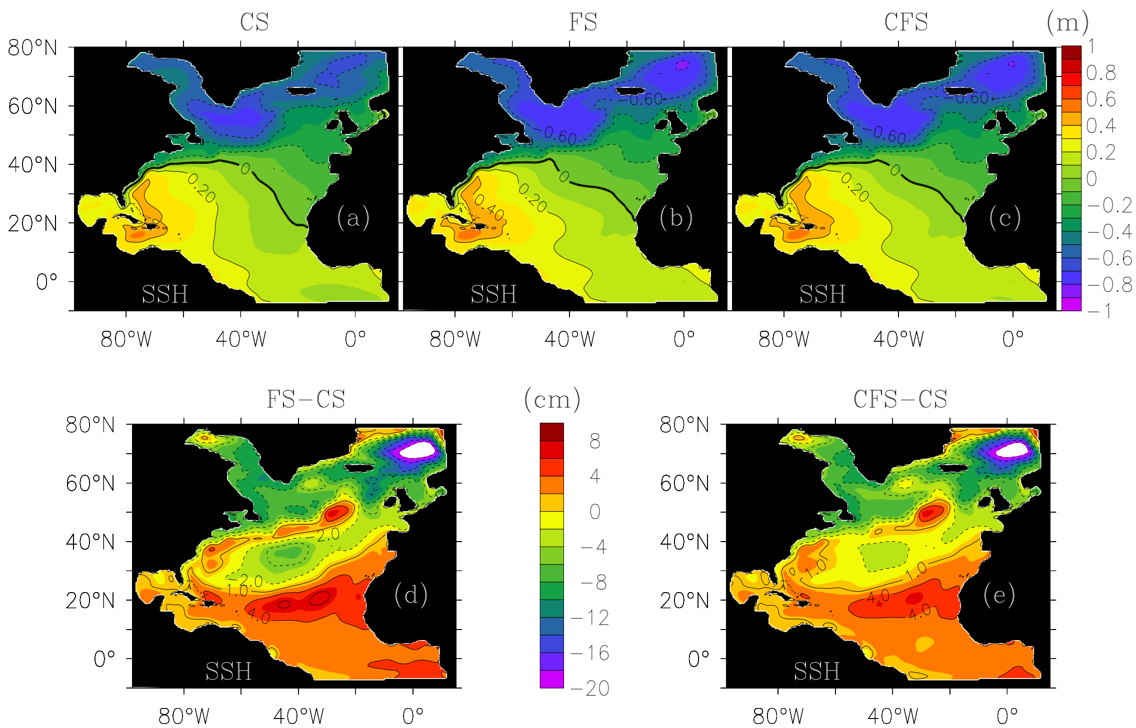

Figure 3.7: Mean sea surface height (SSH) from the 10^{th} year of CS (a), FS(b), CFS(c) and their difference from CS in (d,e)

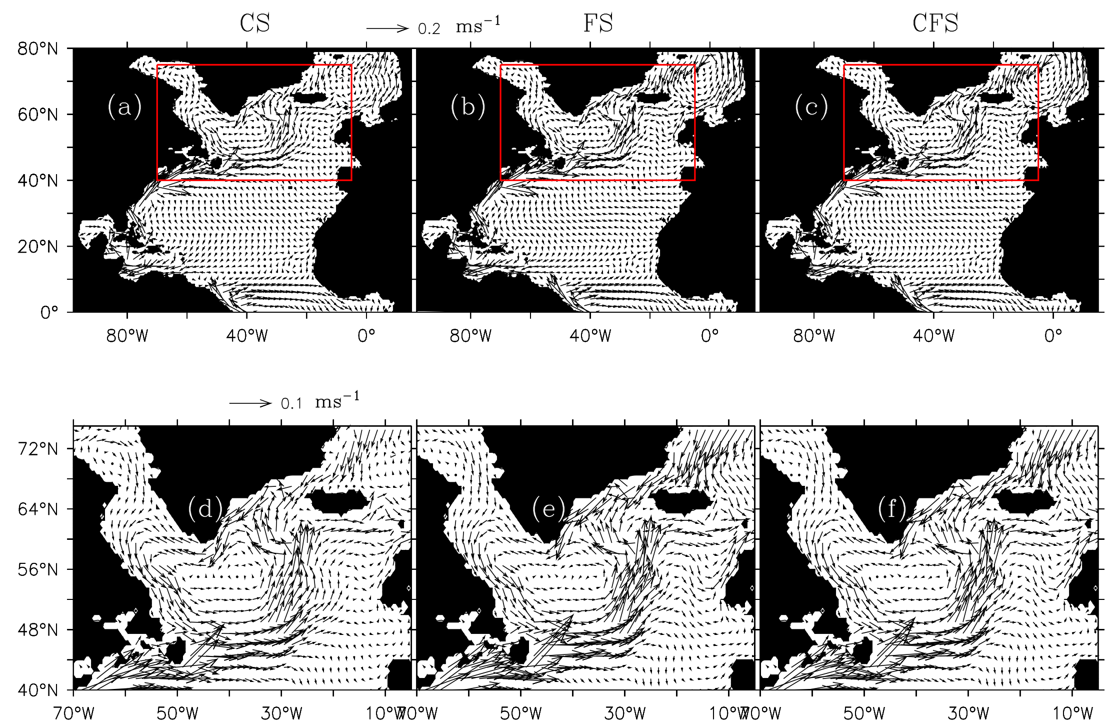

Figure 3.8: Mean currents at 40m depth from the 10^{th} year of CS(a), FS(b), CFS(c) with currents inside the box in the bottom panel (d,e,f) for each run

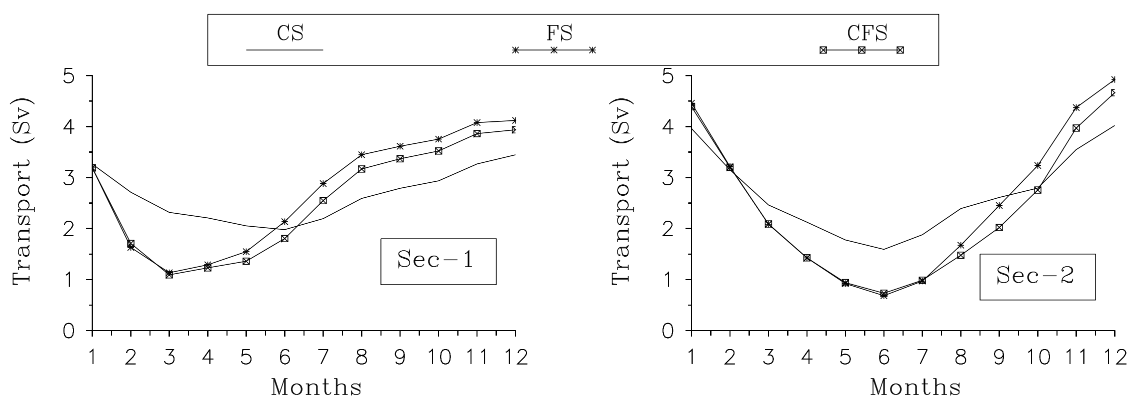

Figure 3.9: 10^{th}year volume transport across Cape Farewell (Sec-1) and Cape Desolation (Sec-2) for each simulations (CS, FS and CFS) relative to 700m depth.

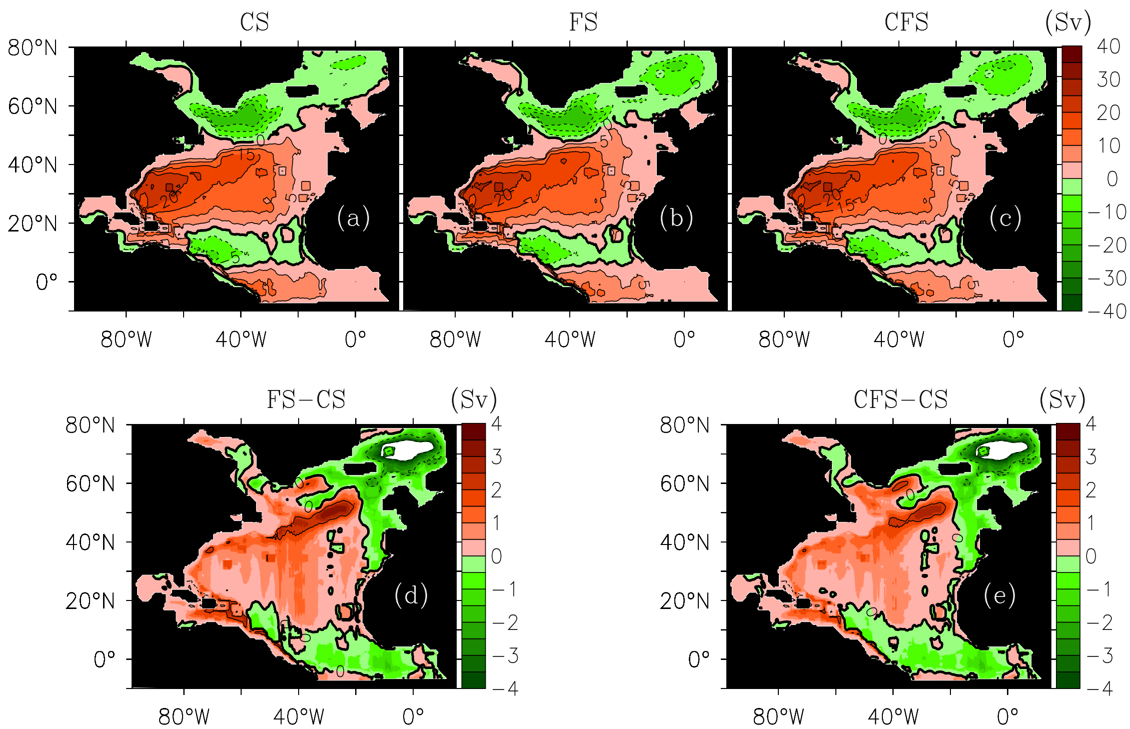

Figure 3.10: 10^{th} year mean barotropic stream function of CS(a), FS(b), CFS(c) and their difference from CS in(d,e)

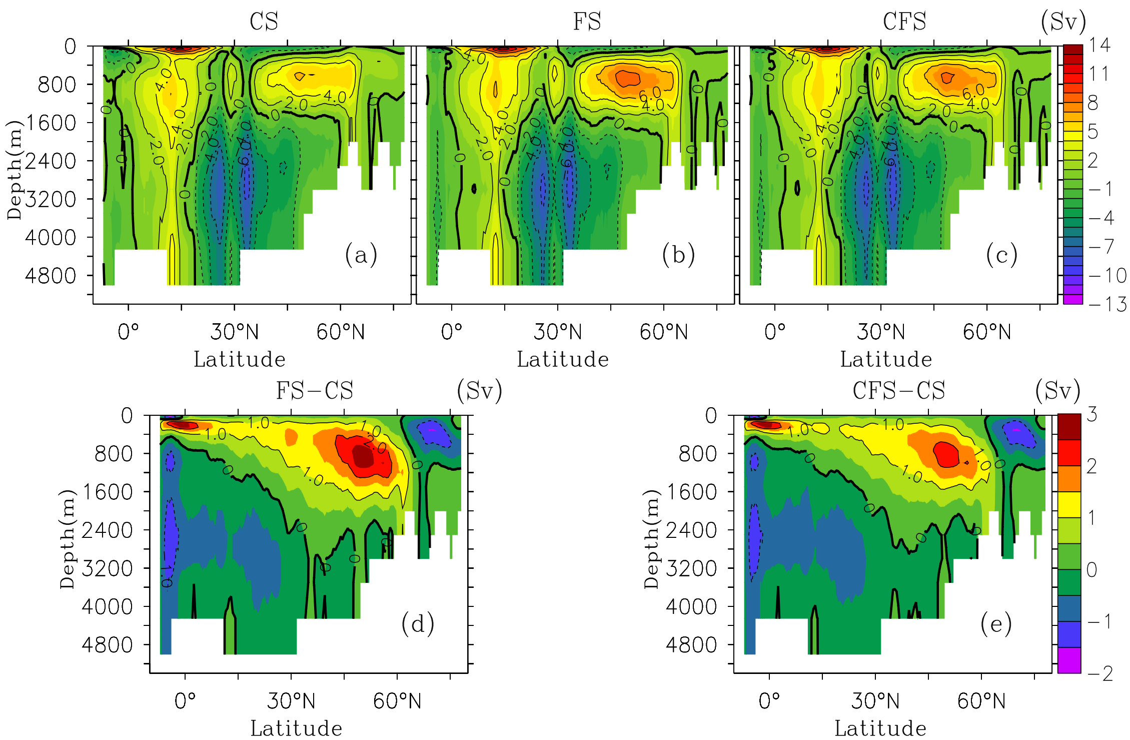

Figure 3.11: Mean meridional overturning stream function in Sv from the 10^{th} year of the CS(a), FS(b), CFS(c) and their difference from CS in (d,e)

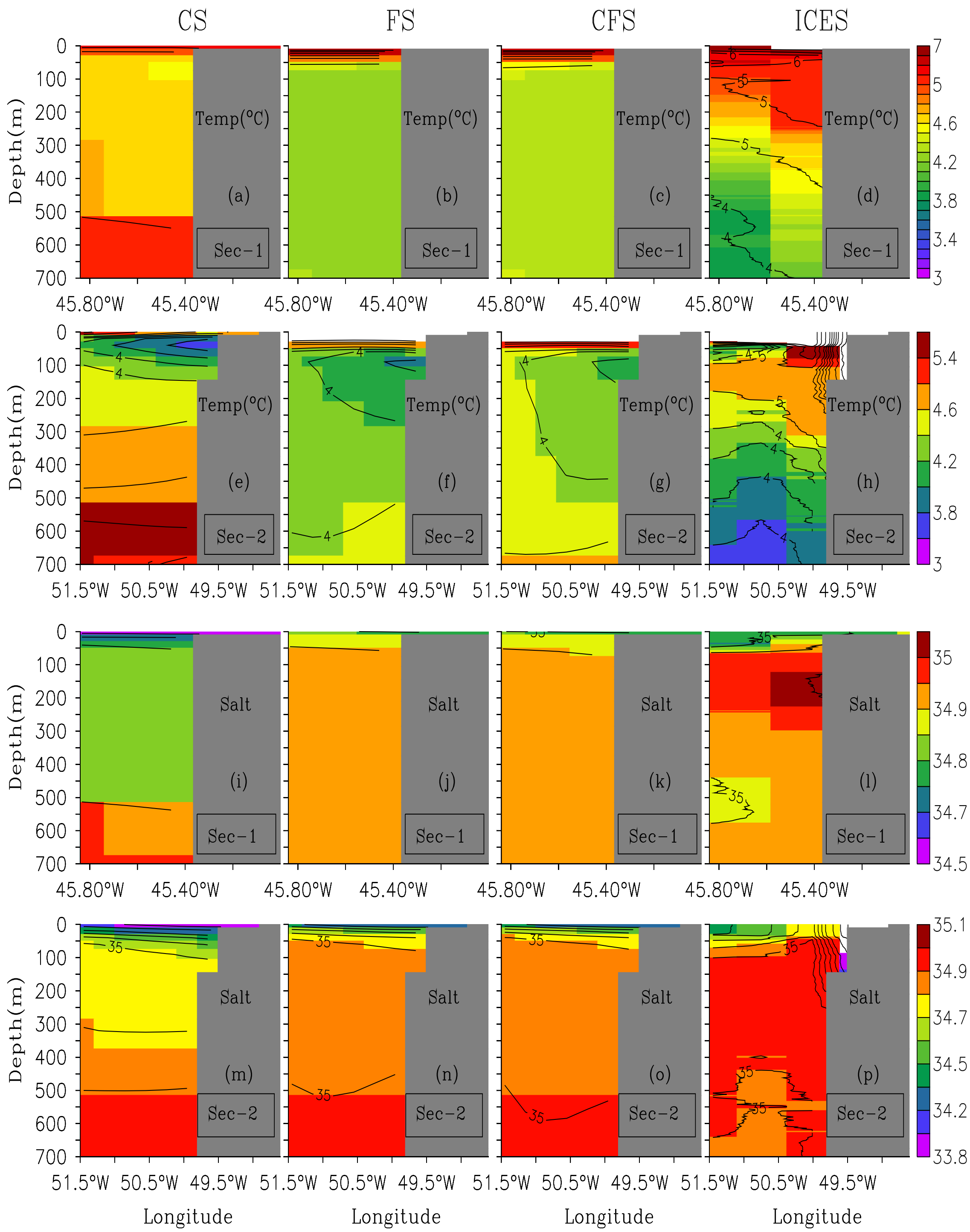

Figure 3.12: 10^{th}year summer mean (June-July) temperature for Cape Farewell (Sec-1) (a,b,c) for the CS, FS and CFS cases and salinity (i,j,k) along with the respective ICES data (d,l) . For Cape Desolation (Sec-2) model temperatures (e,f,g) and salinity (m,n,o) along with the respective ICES data (h,p).

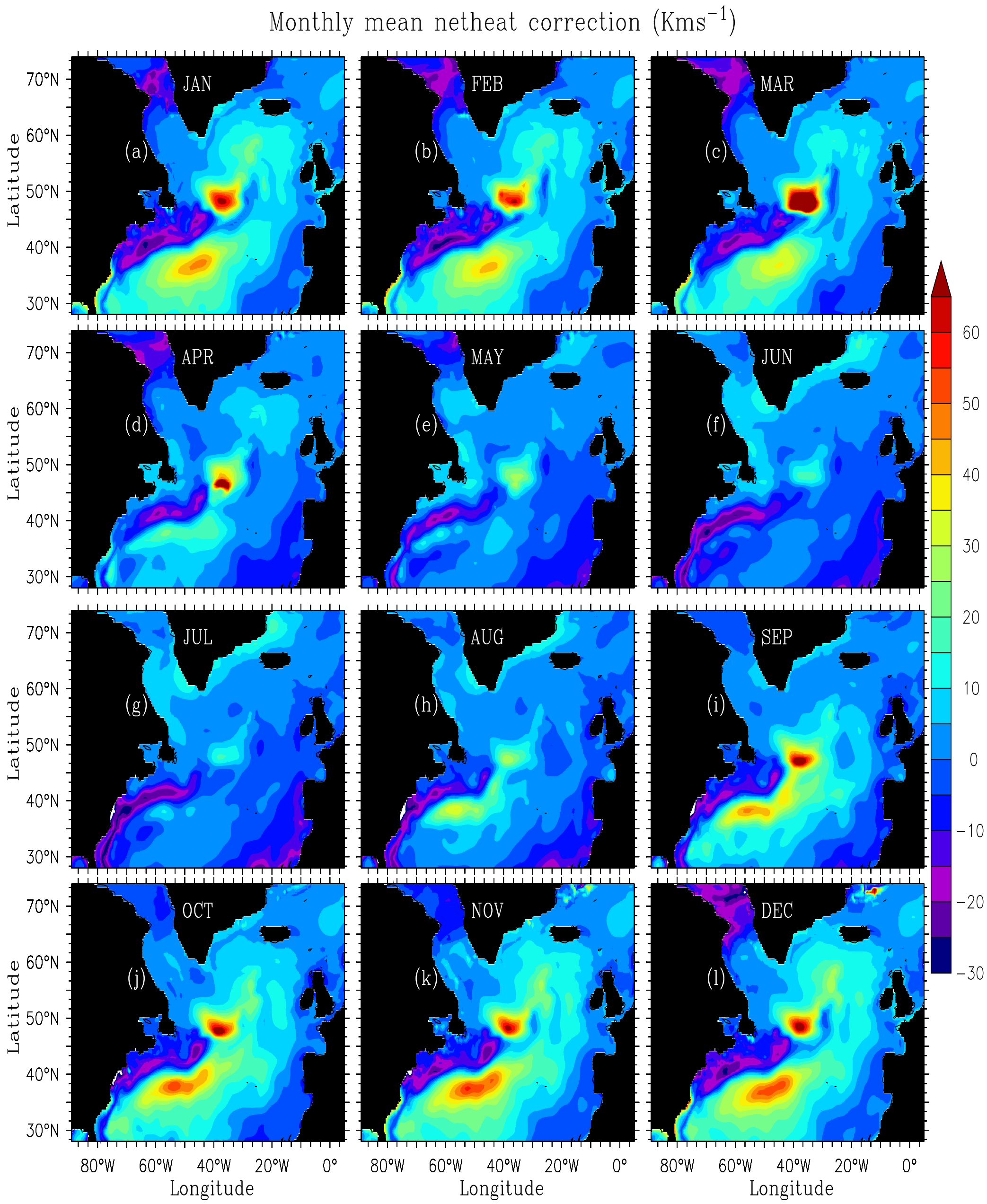

Figure 3.13: 10^{th} year monthly mean net-heat correction (Wm^{-2}) from the CFS experiment

Bibliography

Barnier, B., L. Siefridt and P. Marchesiello (1995). Thermal forcing for a global ocean circulation model using a three year climatology of ECMWF analyses. *Journal of Marine Systems* **6**, 363–380.

Beismann, J.O. and Bernard Barnier (2004). Variability of the meridional overturning circulation of the North Atlantic: sensitivity to overflows of dense water masses. *Ocean Dynamics* **54**, 92–106.

Bourke, Robert H., Robert G. Paquette and Robert F. Blythe (1992). The Jan Mayen Current of the Greenland Sea. *Journal of Geophysical Research* **97**, 7241–7250.

Buch, Eric and Mads Hvid Nielsen (2000). Oceanographic Investigations off West Greenland. In: *Scientific Council Meeting*. pp. 1–22. Number N4357 In: *NAFO SCR Doc. 01/2*. Northwest Atlantic Fisheries Organization.

Chassignet, Eric P., Herman Arango, David Dietrich, Tal Ezer, Michael Ghil, Dale B. Haidvogel, C.C. Ma, Avichal Mehra, Afonso M. Paiva and Ziv Sirkes (2000). DAMEE-NAB: the base experiments. *Dynamics of Atmospheres and Oceans* **32**, 155–183.

Danilov, S., G. Kivman and J. Schroter (2005). Evaluation of an eddy-permitting finite-element ocean model in the North Atlantic. *Ocean Modelling* **10**, 35–49.

Ferry, Nicolas and Gilles Reverdin (2000). Seasonal sea surface height variability in the North Atlantic Ocean. *Journal of Geophysical Research* **105**, 6307–6326.

Gent, Peter R., A.P. Craig, C.M. Bitz and j.W. Weatherly (2002). Parameterization improvements in an eddy-permitting ocean model for climate. *Journal of Climate* **15**, 1447–1459.

Hopkins, Tom Sawyer (1991). The GIN Sea – A Synthesis of its physical oceanography and literature review 1972-1985. *Earth-Science Reviews* **30**, 175–318.

Malone, Robert C., Richard D. Smith, Mathew E. Maltrud and Matthew W. Hecht (2003). Eddy-Resolving Ocean Modeling. *Los Alamos Science* (28), 223–231.

Myers, Paul G., Chris Donnelly and Mads H. Ribergaard (2009). Structure and Variability of the West Greenland Current in Summer derived from 6 repeat standard sections. *Progress in Oceanography* **80**, 93–112.

Ribergaard, Mads Hvid (2006). Oceanographic Investigations off West Greenland 2005. *Technical Report 06/001, NAFO Scientific Council Documents.*

Schmitz, William J. and Michael S. McCartney (1993). On the North Atlantic Circulation. *Reviews of Geophysics* **31**(1), 29–49.

Schott, Friedrich A., Lothar Stramma, Benjamin S. Giese and Rainer Zantopp (2009). Labrador Sea convection and subpolar North Atlantic Deep Water export in the SODA assimilation model. *Deep-Sea Research I* **56**, 926–938.

Smith, Richard D., Mathew E. Maltrud, Frank O. Bryan and Mathew W. Hecht (2000). Numerical Simulations of the North Atlantic Ocean at $1/10^o$. *Journal of Physical Oceanography* **30**, 1532–1561.

Thompson, Keith R., Kyoko Ohashi, Jinyu Sheng, Josko Bobanovic and Jie Ou (2007). Suppressing bias and drift of coastal circulation models through the assimilation of seasonal climatologies of temperature and salinity. *Continental Shelf Research* **27**, 1303–1316.

Chapter 4

Sensitivity study of the GM parameterization

This Chapter details the impact of parameterized sub-grid scale eddies in the model.

Eddies play a major role in the restratification of the Labrador Sea after deep convection (Katsman *et al.*, 2004) by transporting warm and buoyant Irminger Current water into the interior Labrador Sea governed by bathymetry (barotropic) as well as baroclinicity (by rim currents along interior fronts). In order to model the effects of these eddies on tracer transport, a resolution of a minimum of the first Rossby radius of deformation with lower values of mixing coefficients are required (Haidvogel and Beckmann, 2000). The present model resolution used in this thesis is enough to resolve some of these eddies but not the smallest eddies. In order to circumvent this draw back, the popular GM sub-grid scale parameterization scheme is added into the model (Gent *et al.*, 1995). The sensitivity to the choice of thickness diffusion (K_{gm}) in the GM scheme is studied by using a constant as well as a spatially and temporally varying K_{gm}. A spatial and temporally varying K_{gm} scheme is adopted from Visbeck *et al.* (1997), which is given by,

$$K_{gm} = \alpha T^{-1} l^2 \tag{4.1}$$

$$\text{where,} \qquad T^{-1} = \frac{f}{\sqrt{\overline{\overline{Ri}}}} \tag{4.2}$$

Where f is the Coriolis parameter. The constant α has a value of 0.13 as in Eden *et al.* (2009) and the baroclinic length scale l is calculated from the local

Rossby radius of deformation (L_r) as,

$$l = max(\overline{l_r}, \Delta) \tag{4.3}$$

$$\overline{l_r} = \frac{\overline{N}H}{f} \tag{4.4}$$

where Δ is the square-root of the area of the mesh, N and Ri are as given in equations (2.20) and (2.19) respectively. The over line denotes mean quantities over depth (100 to 2000m). Since the Coriolis parameter goes to zero at the equator, f there is given as $\sqrt{2\beta c_r}$, where $\beta = \frac{\partial f}{\partial y}$ and C_r the first baroclinic wave speed given by $C_r = \int_{-h}^{0} \frac{N}{\pi} dz$ (Eden *et al.*, 2009). Further more K_{gm} is restricted to the range of 50 to 3000 m^2s^{-1}, similar to Wright (1997) and Deacu and Myers (2005).

4.1 Simulations

Three additional experiments of 10 model years are carried out to study the impact of sub grid scale eddies in the hydrography of the Labrador Sea and their representation using the GM parameterization. The first experiment (GM_{250}) uses a constant thickness diffusion coefficient (K_{gm}) of 250 m^2s^{-2}. The second one (GM_{area}) uses a spatially variable thickness diffusion that is linearly proportional to the area of the mesh and a third simulation (GM_{vis}) incorporates the baroclinicity of the region as suggested by Visbeck *et al.* (1997) and Eden *et al.* (2009), which varies in both space and time as detailed above.

4.2 GM with constant K_{gm} (GM_{250})

A recent study by Eden *et al.* (2009) using a coarse resolution global ocean model examined the effect of different closures for the thickness diffusivity (K_{gm}) with a range of values from 0 to 5000ms^{-2}. The study also shows a range of 0 to 600ms^{-2} value for the subpolar region of the North Atlantic Ocean. Based on this study, as a zeroth order choice a constant value of 250ms^{-2} for the K_{gm} is used in this simulation. Such an approach can be of use to compare the sensitivity of this parameter in time and space.

The comparison of results from this simulation to a climatology shows the distinctive separation of temperature (Figure-4.1) and salinity (Figure-4.2) properties near the Gulf Stream region marking the front compared to the CFS run. The salinity drift offshore of Newfoundland is reduced from -2 units to -0.5 units compared to the CFS case. Where as the temperature shows a 1 degree rise in the subpolar gyre and offshore of Newfoundland.

10^{th} year winter (JFM) mean MLD for this run is shown in (Figure-4.3). The over estimation of MLD in the Labrador Sea is reduced by 500m from the CFS case, even though the Irminger sea still shows an over estimation caused by the bias in the WOA climatology (Schott *et al.*, 2009).

The strength and the structure of the subpolar gyre in the Labrador Sea region has improved from the CFS case. This is evident in the better representation of low SSH in the Labrador Sea region as shown in Figure-4.4.b. A similar SSH pattern is observed in the high resolution eddy-resolving model study of Malone *et al.* (2003) using Los Alamos's Parallel Ocean Program (POP) model.

Compared to CFS, even though the vertical profile (Figure-4.5) shows lesser drift towards higher salinity in the deeper layers, the drift around 500m (which covers a larger area of the Labrador Sea) acts as a potential barrier layer to vertical mixing and causing further drift in the freshwater content to continue (Figure-4.6).

4.2.1 Transports

The weakening of the volume transport as the integration proceeds through the sections in the boxes (Figure-4.7) WGB, EGB and LB in the subpolar gyre (in the CFS case) is replaced by a stronger transport (Figure-4.9, 4.10) in this experiment. The variability in the plots are the result of eddy shedding around the boundary current region as noted by Jones and Marshall (1997) with a seasonal variability. Here the positive values show the perpendicular transport in Sv into the respective box (WGB or EGB or LC) with negative values as export. In order to calculate these perpendicular transports, the model velocities are first rotated onto an axis aligned with the sections of the boxes. All the following discussion containing these sections use only the velocity components that are perpendicular to the sections unless stated otherwise.

A 10^{th} year mean of 3.76 Sv offshore transport with a maximum of 4.73 Sv in October month is observed for the WGC_T section. Whereas CFS had a mean of 5.94 Sv with a maximum of 7.30 Sv in July and a minimum of 4.42 Sv in January. The mean transport across section WGC_S in the CFS case is 9.40 Sv which then mainly dissipates across the WGC_T section. Whereas in GM_{250} the considerably increased mean transport of 20.27 Sv across WGC_S is transported northward and exits through section WGC_N ($\approx 18\,Sv$), leading to the weak transport across WGC_T section. A detailed comparison on the transports across other sections is given in Table-4.1.

Figure-4.11 shows the sectional mean time series of S_{ref}-salinity across the sections shown in Figure-4.7. This gives a measure of the mean freshness of the sections. The mean salinity across the EGC_T and LC_T (Figure-4.11) sections is decreased compared to that of the CFS, whereas EGC_S, EGC_N, LC_N and LC_S show an increase. Even though the transport across the south and north sections of the box LB (Figure-4.7) balance each other (Figure-4.12), the decrease in salinity in LC_T (Figure-4.11) is coming from the merging of freshwater across the WGC_T section along its cyclonic path to Labrador Current (LC).

The salinity drift in the early model years (1 to 6) of the CFS experiment across WGB and LB box sections is reduced in GM_{250} (Figure-4.6), a contribution through the deeper layers (200 to bottom) (Figure-4.13, 4.14), whereas in the EGB box section, it is balanced through both the surface (0 to 200m) and deeper layers.

The northward flow maxima in the MOC has strengthened compared to the CFS whereas the southward flow maxima is reduced by 1 Sv as it spread over a broader depth range. However the structure of the MOC became closer to other studies (Beismann and Barnier, 2004).

4.2.2 Fresh water

Time series of the total freshwater content (FWC) in the whole Labrador Sea region and the interior (defined as a region deeper than 3000m) are shown in Figure-4.6.a and Figure-4.6.b respectively, which shows a steady drift similar to that of the CFS case, with a lag in the interior of the Labrador Sea freshwater content (Figure-4.6.b).

In order to scrutinize the influence of boundary currents towards this drift, the freshwater transport across the sections in Figure-4.7 are calculated as follows,

$$FWT = \int_A \vec{v} \left(\frac{S_r - S}{S_r} \right) dA \tag{4.5}$$

where A is the area of the vertical section and $\vec{v}$ is the rotated cross velocity perpendicular to the section. The freshwater content drift in Figure-4.6 is caused by the weak offshore freshwater transport along the West Greenland section (WGC_T) in the upper layers (0-200m) of the water column (Figure-4.13). Towards the 10^{th} year of the simulation this weakening spreads to deeper layers (200-bottom) (Figure-4.13), leading to the drift in the salinity profile of the Labrador Sea region as shown in Figure-4.5.d. The weak freshwater transport across the WGC_S section (200 to bottom) (Figure-4.14) towards the 10^{th} model year is causing this trend in the WGC_T section.

Compared to the CFS, this experiment shows a reduction in temperature in the Labrador Sea interior causing the density to increase and raise the isopycnals (Figure-4.15.a). This process together with cyclonic circulation brings the denser water closer to the surface, a prerequisite for the deep convection to occur (Gascard, 1991; Steffen and D'Asaro, 2002). A subsurface (below 150m) summer salinification and warming of the Labrador Sea interior leading to a thinner LSW during the restratification period as noted by Straneo (2006*b*) is more evident in this experiment (Fgiure-4.15.b). However the year long subsurface warm and saline layer (800 to 1200m) found in the Labrador Sea interior of the CFS simulation (Figure-4.15.a) is absent in this experiment.

The WGC_T section in Figure-4.13 shows a reduction in the fresh water compared to that of CFS. The reduction in offshore transport collectively with less available fresh water (Figure-4.11) further adds to the salinity drift in the Labrador Sea.

4.2.3 Results and Discussion

The temperature drift near the Gulf Stream region is still poor in this run (Figure-4.1) similar to that of CFS (Figure-3.3), however the drift in salinity in this region and subpolar gyre is reduced (Figure-4.2). The vertical profile of salinity in the interior of the Labrador Sea still drift towards higher salinity compared to that of the CFS case from surface to mixed layer depths, which in turn contributes to further drift in freshwater content (Figure-4.6).

These drifts could be explained by the weak cross isobath transport of freshwater from the WGC system evident in the WGC_T cross section, irrespective of the higher transport from south across the WGC_S section. This result implies that the freshwater entering through the south of WGC system exits through the north without entering into the Labrador Sea interior and causing the drift in the freshwater content (Figure-4.6) to continue as in that of the CFS case.

4.3 GM with variable K_{gm}

This section details the two simulations that incorporated a spatially variable as well as both spatially and temporally varying K_{gm}.

4.3.1 K_{gm} linearly proportional mesh size (GM_{area})

To study the sensitivity of K_{gm} to its spatial variability, a spatially varying K_{gm} that depends on the area of the mesh is introduced in this simulation.

Tracer fields shows minor differences from the GM_{250} run (Figure-4.1, 4.2). The same is true for the MLD (Figure-4.3), MOC (Figure-4.16), SSH and currents (Figure-4.4).

Vertical sections at Cape Farewell (Sec-1) and Cape Desolation (Sec-2) (Figure-4.17) for the summer months (June-July) shows an increase in temperature by 1^oC and this difference extends to deeper depths compared to the

WOA dataset and ICES. A similar increase in salinity of 1 unit is also noted. Detailed features in the ICES data are still missing in the model due to the weak representation of WGC and EGC.

4.3.1.1 Transports

The volume transport across the sections in boxes WGB, EGB and LB (Figure-4.7) shows trends similar to that of the GM_{250} run (Figure-4.9, 4.10), with enhanced variability caused by the spatial variations in the thickness diffusion coefficient compared with a constant in GM_{250} run.

The strength of the sub polar gyre is increased and well marked compared to that of the CFS run (Figure-4.18.b,e). This leads to a stronger transport around the Greenland sections (Figure-4.7). However compared to CFS, the transport across the WGC_T section continues to be weak and often onshore (Figure-4.19) with a slightly higher mean value of 4.05 Sv than that of the GM_{250} (3.76 Sv). This relatively higher transport happens despite the weak transport across the WGC_S section compared to that of the GM_{250} by a magnitude of 1 Sv (Table-4.1). However the model's freshwater content continues to drift as that of GM_{250} and CFS (Figure-4.6) due to the above weak volume transport (Figure-4.19) across the WGC_T section.

4.3.1.2 Fresh water

The steady drift in the fresh water content (Figure-4.6) from the initial state is evident and a similar result is observed for the GM_{250} run. The drift is caused by the salinification from surface to the mixed layer as shown in the vertical profile of salinity (Figure-4.5.d and f) caused by the weak interior transport as explained above. On all the sections in Figure-4.7, the freshwater transport shows similar trends to that of GM_{250} in the deeper layers and shows large drift in the top layers (0-200m) (Figure-4.13, 4.14). Figure-4.11 shows a similar decrease in freshness as that of GM_{250} across these sections.

This concludes that the stronger boundary current in these two simulations (GM_{250} and GM_{area}) carries away the freshwater along the boundary rather than across into the interior leading to the salinification from surface to the mixed layer depths in the interior of the Labrador Sea as noted in the vertical profile Figure-4.5 and the freshwater content (Figure-4.6).

4.3.1.3 Results and Discussion

The results from these two experiments conclude that, irrespective of the stronger boundary current (compared to the CFS case), the weak freshwater transport across the WGC_T section into the Labrador Sea interior led to the salinification from the surface to the mixed layer depths (Figure-4.5), leading to the continued drift in the freshwater content (Figure-4.6).

Comparison of the GM_{250} and GM_{area} shows that, the results from these two experiments are very similar, due to the fact that the mean value of K_{gm} for the Labrador Sea region is around $250\,m^2s^{-1}$ in the GM_{area} run. Based on this conclusion, the GM_{area} run will be used for further analysis and comparison in this thesis.

According to Bracco and Pedlosky (2003), baroclinicity is the main mechanism for the instability along such boundary currents and barotropic according to Eden and Boning (2002). Whereas Katsman *et al.* (2004) found this process to be a mixed one. A better representation of the baroclinicity of this boundary current region in the model could resolve this issue, which is weak in the current mesh size dependent K_{gm} incorporated simulation. This leads to the next choice of incorporating baroclinicity into the determination of K_{gm}, leading to a temporally and spatially varying K_{gm} approach.

4.3.2 K_{gm} suggested by Visbeck *et al.*, 1997 and Eden *et al.*, 2009 (GM_{vis})

In this simulation both the spatial and temporal dependence of K_{gm} as proposed by Visbeck *et al.* (1997) and Eden *et al.* (2009) is studied. Meanwhile, both the GM_{vis} and CFS simulations were extended to 15 model years to compare and evaluate the drift in the model result.

The mean K_{gm} values from the 15^{th} model year and a domain averaged time series of the same are shown in Figure-4.20.a,c. The value of K_{gm} shows both spatial and temporal variability ranging from 50 to $3000\,ms^{-2}$ with a domain average of 270 to 370 ms^{-2} (Figure-4.20.c). Bolus velocities, as explained in Chapter 2 are also extracted from the model and a 15^{th} year average is shown in Figure-4.20.b along with a domain averaged time series (Figure-4.20.d). Higher velocities are observed in the Labrador Sea region as well as in the region of the overflows, where the boundary currents and baroclinicity are strong. The freshwater that these boundary currents carry meets the high saline water of the Irminger current thus leading to a highly baroclinic zone, which produces high bolus velocities.

The near surface mean tracer properties from the 10^{th} model year of this experiment are shown in Figure-4.21 and 4.22. Compared to all the previous experiments, the drift from the WOA data set around the Gulf Stream region and the Labrador Sea is reduced in this experiment. The drift in temperature near the coast of Newfoundland, of more than 5^oC found in the CFS and GM_{area} experiments is reduced to less than 4.5^oC and offshore from more than -8^oC to -5^oC. Meanwhile the drift in the interior of the Labrador Sea in the GM_{area} experiment of 2.5^oC is also reduced to less than 1.5^oC.

Compared to the CFS experiment, the salinity off the Newfoundland coast in both GM_{vis} and GM_{area} simulations shows a reduction in the drift from the WOA data set from more than 1 unit to less than 0.5 units (Figure-4.22). A similar but minor improvement is observed close to the Newfoundland coast and in the interior of the Labrador Sea.

Meanwhile the depth averaged annual mean tracer properties from the 10^{th} model year (Figure-4.23) shows many improvements from the previous experiments. The temperature drift of more than 2.6^oC in the subpolar gyre and along the western boundary of the subtropical gyre (Figure-4.23.b,f) is reduced to near zeros in this experiment (Figure-4.23.f). A similar improvement of more than 0.1 units is observed in the mean salinity of these regions (Figure-4.23k,l). These improvements are predominant in regions of high baroclinic activity. This emphasizes the importance of the choice of a K_{gm} that incorporates the baroclinicity of the region.

The MOC in this experiment is improved with a stronger northward transport, well spread in the vertical (13 Sv) as well as with a stronger deeper southward transport compared to that of the previous simulations (Figure-4.16). The stronger, deeper-cold southward transport combined with a stronger warm northward transport results in the net meridional heat transport more positive and northward (Figure-4.24).

The boundary currents are stronger in both GM_{vis} and GM_{area} experiments compared to that of the CFS experiment (Figure-4.18). A detailed analysis of the transports across these currents follows.

The 10^{th} year summer mean (June-July) vertical temperature and salinity for the sections at Cape Farewell (Sec-1) and Cape Desolation (Sec-2) for GM_{area}, GM_{vis}, WOA and $ICES$ data are shown in Figure-4.17. Compared to WOA, ICES and GM_{vis} results, the GM_{area} experiment shows a drift towards a warm and saline water column. The vertical salinity structure for the GM_{vis} at Sec-2 is closer to the WOA . The warmer surface and relatively colder deeper layers of Sec-1 in the GM_{vis} run are similar to that of the WOA and ICES data set.

A comparison of the 10^{th} year mean volume transport and it's standard deviation across these sections along with the observational study of Myers *et al.* (2009) is shown in Table-4.2. The transport across the Cape Desolation section in this experiment ($4.9 \pm 0.9Sv$) is more closer to the observations ($5.5 \pm 3.9Sv$). Meanwhile the mean transport across the Cape Farewell section (for GM_{vis}) is relatively low. However it's standard deviation is also smaller compared to the other experiments. Overall the sections in GM_{vis} run is closer to the observations.

In this run, the vertical profile of salinity is also maintained through the model years (Figure-4.5.h) thus reducing the model freshwater content drift (Figure-4.6). Meanwhile the temperature profile shows a slight return towards the beginning years of the model simulation (Figure-4.5.g).

4.3.2.1 Fresh water

The increasing trend in freshwater content in this simulation (Figure-4.6) around the later model years (6 to 10) coincide with an increased outflow (negative) across the west Greenland coast (section WGC_T) as shown in Figure-4.9

and an increased flow (positive) around Cape Farewell (section WGC_S) as shown in Figure-4.10. The weakening of these transports (Figure-4.9, 4.10) produced the drift in freshwater content that dominated the previous simulations.

4.3.2.2 Transports

The annual mean meridional heat transport (Figure-4.24) for the GM_{vis} run is above zero through all latitudes compared to the CFS simulation. This can be attributed to the strengthening of the northward component of MOC in the upper layers (Figure-4.16).

Figure-4.25 shows the vertical mean transport across WGC_T, EGC_T and LC_T and the corresponding Salinity-S_{ref} and temperature anomaly from the model's 15^{th} year. This gives a picture of the transport across these sections in terms of its relative freshness and warmness. All the transport across these sections are fresher than the reference salinity of 35. However, the northern part of the WGC_T section transports cold and fresh water compared to the south where it meets the warm and saline Irminger waters.

Figure-4.26 shows the monthly mean σ_θ and perpendicular transport across WGC_T, EGC_T and LC_T sections from the model's 15^{th} year. The northern end of the WGC_T section is less dense and has onshore transport whereas the middle of the section (50.5^oW to 46^oW) transports offshore (mean $\approx$ 6.1 Sv). Overall the transport is towards the interior of the Labrador Sea (6.3 Sv) and it is fresh and relatively warm compared with other locations in the section. This transport is stronger than the mean transport values of all the previous simulations (Table-4.1).

The southern end of the EGC_T section (44^oW to 33^oW in longitude) is dominated by a mixture of cold and saline offshore transport, where the cold-fresh EGC and warm-saline IC merges. Figure-4.26 in this location shows an offshore transport of uniform but higher density waters compared to that of the northern end where less dense and onshore transports are found. Whereas the LC_T section shows relatively the same temperature and salinity throughout the section, except at the middle ($\approx 52^oW$) where the fresh and warm waters crossing the WGC_T section merges and a narrow band of onshore transport is present (Figure-4.26). Overall the transport across the LC_T section is onshore (with a mean of 26.58 Sv) (Table-4.1).

To find the relative importance of variability in salinity (S) and velocity ($\vec{v}$) on the freshwater transport across the sections in Figure-4.7, these variables are split into their mean and perturbation (anomaly) components as below.

$$S = \overline{S} + S' \tag{4.6}$$

$$u = \overline{u} + u' \tag{4.7}$$

$$v = \overline{v} + v' \tag{4.8}$$

From the above, two entities ($\overline{S}v'$ and $\overline{v}S'$) were derived. The expression $\overline{S}v'$ gives the contribution of the variability in velocity on the freshwater transport and $\overline{v}S'$ the contribution of the variability in freshwater transport on the velocity (Figure-4.27, 4.28). Transports across the WGC_T section show a dependence on variabilities in velocity (Figure-4.28), where as WGC_S shows a dependence on variabilities in both velocity and salinity (Figure-4.27). However, the magnitude of variability in transport across WGC_N is found to be relatively small for both $\overline{S}v$ and $\overline{v}S'$ compared to the previous sections.

4.3.2.3 Eddy Transports

Figure-4.29 shows the vertical mean eddy transport across WGC_T, EGC_T and LC_T and corresponding Salinity-S_{ref} and temperature anomaly from the model's 15^{th} year. This gives a picture of the eddy transport across these sections in terms of its relative freshness and warmness. Even though the northern end of the WGC_T section (54^oW to 50.5^oW) is dominated by the resolved onshore transport (Figure-4.25), some cold and fresh eddies are still transported offshore (Figure-4.29). Whereas the middle of the WGC_T section (where the WGC starts its cyclonic turn at 50^oW to 48^oW) is completely dominated by resolved transport (Figure-4.25) rather than the eddy induced transport. This result implies that the transport across WGC_T section in it's southern and northern ends are dominated by the eddy induced transports whereas resolved transports at the middle of the section.

The eddies dominate in the 200 to 800m depth range in the above sections, as seen in Figure-4.8. This could contribute to the increase in freshwater transport found in the deeper layers (200m to bottom) as shown in Figure-4.13 compared to the CFS simulation, where the mean transport was also weak (Figure-4.19). However the Irminger current in this depth range also advects warm and saline waters in to the Labrador Sea basin (Cuny *et al.*, 2002; Lazier *et al.*, 2002). These two contrasting statements could be explained by the seasonality (Lazier, 1980) in the salinity anomaly for the WGC_T section shown in Figure-4.30, where the transport across this section is more fresh and strong (mean 6.5 Sv) in the late spring and summer months (April to August) compared to a mean 5 Sv saline transport in late fall and winter months (October to March). Spall (2004) and Katsman *et al.* (2004) found a similar seasonal role of these boundary current eddies and their exchange into the basin in setting the convection depth for an idealized basin.

The strength of the subsurface (200-800m) eddy activity associated with the Irminger Current in this experiment is comparatively stronger than the other two GM incorporated experiments (Figure-4.31). The mean monthly eddy velocity plot (Figure-4.32) from the 15^{th} model year shows the seasonal variability of the eddy activity in subpolar region with higher magnitudes towards the spring (Prater, 2002). The eddies are mostly confined to the coast during the winter months (December to April) and then spread to the interior during late winter to late summer (April to August). These eddies play a major role in the restratification of the Labrador Sea after deep convection as clearly seen in the monthly MLDs (Figure-4.33), with the MLD getting shallower in April to October. However the deepening of the MLD in winter months (December to March) is mainly due to the loss of net-heat flux into the overlying cold atmosphere.

4.3.2.4 Boundary currents and the Labrador Sea interior

Monthly salinity anomaly sections from the 10^{th} model year along with perpendicular cross sectional transport (Figure-4.30) of the WGC_T section shows a late fall and winter (November to February) subsurface (200 to 800m) high saline and warm anomaly (Figure-4.34) arising from the Irminger water with a relatively lower density anomaly (Figure-4.35). This water is being capped by a cold-fresh (Figure-4.30) surface water (Figure-4.34) in winter (December to February) which has a higher density anomaly (Figure-4.35) (contributed by the reduction in temperature). These properties are transported into the Labrador Sea interior with a mean perpendicular transport of 5.5 Sv in the above periods. This is evident in the Hovmoller diagram of Labrador Sea interior salinity and temperature (Figure-4.15), where the profile turns to high saline and cold during January till the summer (June). In rest of the months (March to September), this subsurface layer has a lower salinity and temperature anomaly with a higher density anomaly.

The summer (May-June) surface layer of WGC_T is comprised of a saline (Figure-4.30) and cold water anomaly (Figure-4.34) tending to become warm and saline anomaly in the later summer (July-September) with a lower density anomaly (Figure-4.35). This occurs before going back to the fresh and cold anomaly with higher density anomaly in the winter.

The above two processes are seen in the Hovmoller diagram of the Labrador Sea interior tracer properties (Figure-4.35), where a thickening of LSW occurs in the winter months (convection) followed by an equivalent thinning (restratification) as noted by Straneo (2006*a*). This implies that the hydrography of the boundary currents and their perpendicular cross transports duly play an important role in the vertical profile of the Labrador Sea interior properties. The transport of waters with a high salinity anomaly and relatively smaller density anomaly into the interior of the Labrador Sea are important in the preconditioning phase of the Labrador Sea before deep convection (Steffen and D'Asaro, 2002). The continuous cooling at the surface in winter months along with this subsurface saline layer and cyclonic currents leads to the raising of isopycnals (Figure-4.35) leading to the deep convection phase. Later in the summer the freshening and warming observed in the WGC_T section marks the restratification phase (Figure-4.35,4.15). Interestingly the Labrador Sea interior during this period (April to August) of restratification is dominated by offshore Irminger Current eddies (Lilly *et al.*, 2003) as shown in Figure-4.32.

This feature might be facilitating the restratification phase.

The above explained seasonal transport of subsurface Irminger water is also found to be influenced by the eddies in the 200 to 800m depth range in the WGC_T section as shown in Figure-4.29, 4.8 and detailed in subsection-4.3.2.3.

4.4 Summary and Discussion

The over estimation of winter (JFM) MLD in the Labrador Sea found in the CFS experiment ($> 1500\,m$) is reduced in the GM_{250} and GM_{area} simulations (Figure-4.3). Meanwhile the MLD over estimation in the Irminger sea due to the bias in WOA data set (Schott *et al.*, 2009) in CFS, GM_{250} and GM_{area} simulations is also reduced in the final GM_{vis} experiment.

The drift in mean temperature around the Gulf Stream region and the Labrador Sea is reduced in the GM_{vis} experiment compared to that of all the other experiments (Figure-4.21). Similar improvement is also observed in the mean salinity (Figure-4.22).

The strength and transport across the boundary currents into the interior of the Labrador Sea is also increased leading to the reduction of the salinity drift in this area. This is evident in the vertical salinity profile of the Labrador Sea region (Figure-4.5), where it keeps a steady profile through the model integration.

Analysis of the GM_{250} and GM_{area} experiments shows similar results due to the fact that the mean K_{gm} in GM_{area} is around $250\,ms^{-2}$. Even though the GM_{area} experiment uses a spatially varying K_{gm}, both these experiments uses the same value of K_{gm} from surface to deep through the model years. This approach thus lacks the ability to incorporate the baroclinic structure of the area under study. Since the boundary current region of Greenland is both baroclinic and barotropic in nature (Katsman *et al.*, 2004), a reasonable representation of eddies of this region in these experiments will be weak. This is evident in the weak eddy induced transport across the WGC section as shown in Figure-4.31.

The GM_{vis} experiment was able to explain the role of the boundary current in setting the post convection MLD depth in the Labrador Sea interior. The seasonality and the depth at which the transport happens marks the various phases of the convection processes. Boundary current eddies are found to play a major role in the GM_{vis} experiment as shown in the eddy transport across WGC (Figure-4.8,4.31) as well as in the freshwater transport (Figure-4.29). However the eddy transports dominate at mid-depths (200 - 800 m) where the IC meets the WGC impacting the resolved transport as shown in Figure-4.19 and 4.12. Figure-4.29 shows that the cold-fresh eddies are active in the north (transported by mean flow) and warm-saline eddies around the southern (transported by eddies) end of the WGC_T section. These results closely match with the observational study of the Labrador Sea eddy field by Lilly *et al.* (2003).

Figure-4.19 shows that the total volume transport across the Labrador Current (LC) is onshore (positive). This implies that this boundary current has the major role of draining the boundary current waters out from the basin and rather a minor role in setting the properties of the Labrador Sea interior.

Overall the GM_{vis} experiment was able to reduce the freshwater drift in the model by incorporating the effects of the baroclinic eddies in the boundary current regions of the Labrador Sea. This experiment was also able to show the role of boundary current eddies and seasonal exchange of heat and freshwater across the boundary currents in setting the convection depth in the Labrador Sea basin.

Exp.	Volume transport	WGC_T	WGC_N	WGC_S	EGC_T	EGC_N	EGC_S	LC_T	LC_N	LC_S
CFS	Mean (Sv)	-5.94	-0.27	9.4	-6.76	-0.04	-5.92	15.85	9.84	-11.78
	Maximum (Sv)	-7.3 (Jul)	-0.61 (Dec)	11.64 (Jan)	-9.9 (Dec)	-0.092 (Jun)	-6.99 (Dec)	18.61 (Jan)	12.31 (Jan)	-13.80 (Dec)
	Minimum (Sv)	-4.42 (Jan)	-0.061 (Jun)	7.43 (Jun)	-4.24 (Jun)	0.001 (Oct)	-5.15 (Jun)	13.94 (Jun)	8.07 (Jun)	-10.40 (Jun)
GM_{250}	Mean (Sv)	-3.76	-0.76	17.98	-20.27	-0.22	-11.49	28.27	20.06	-21.32
	Maximum (Sv)	-4.73 (Oct)	-1.49 (Dec)	19.74 (Jan)	-22.47 (Mar)	-0.31 (Apr)	-12.48 (Jan)	31.03 (Jan)	23.60 (Dec)	-24.97 (Dec)
	Minimum (Sv)	-1.84 (Jul)	-0.21 (Jun)	16.73 (Jun)	-18.24 (Aug)	-0.16 (Jul)	-10.52 (Jun)	25.64 (Oct)	17.26 (Jun)	-20.11 (Jul)
GM_{area}	Mean (Sv)	-4.05	-1.20	18.71	-19.27	-0.31	-12.32	26.65	18.74	-18.92
	Maximum (Sv)	-6.36 (Nov)	-2.68 (Jan)	19.47 (Dec)	-20.82 (Feb)	-0.48 (Apr)	-13.35 (Sep)	30.78 (Jan)	23.65 (Dec)	-23.11 (Dec)
	Minimum (Sv)	-3.40 (Jul)	-0.24 (Jun)	17.70 (Oct)	-16.47 (Oct)	-0.13 (Sep)	-10.98 (May)	23.23 (Oct)	14.96 (May)	-16.74 (May)
GM_{vis}	Mean (Sv)	-6.38	-0.30	15.63	-20.02	1.086	-10.12	26.58	16.57	-18.41
	Maximum (Sv)	-7.63 (Mar)	-0.80 (Dec)	17.56 (Jan)	-23.06 (Sep)	2.41 (Dec)	-11.54 (Jan)	29.94 (Jan)	20.11 (Jan)	-21.72 (Dec)
	Minimum (Sv)	-5.15 (Dec)	-0.02 (May)	14.36 (Jun)	-17.31 (Apr)	0.01 (Apr)	-9.09 (Jun)	24.55 (Jun)	14.50 (Jun)	-16.81 (Jun)

Table 4.1: A comparison of the 10^{th} year volume transport (in Sv) for CFS, GM_{250}, GM_{area} and GM_{vis} experiments from the vertical sections of WGB, EGB and LB boxes shown in Figure-4.7

Section	**CFS**	**GM_{250}**	**GM_{area}**	**GM_{vis}**	**Myers *et al.*, 2009**
Cape Farewell (Sec-1) (in Sv)	2.6 ± 1	3.3 ± 1.1	3.5 ± 1.2	2.8 ± 0.5	3.2 ± 2.3
Cape Desolation (Sec-2) (in Sv)	2.5 ± 1.3	7.0 ± 0.8	6.9 ± 1.2	4.9 ± 0.9	5.5 ± 3.9

Table 4.2: 10^{th} year annual mean volume transport and it's standard deviation (in Sv) across Cape Farewell and Cape Desolation sections for CFS, GM_{250}, GM_{area} and GM_{vis} simulations compared to Myers *et al.*, 2009

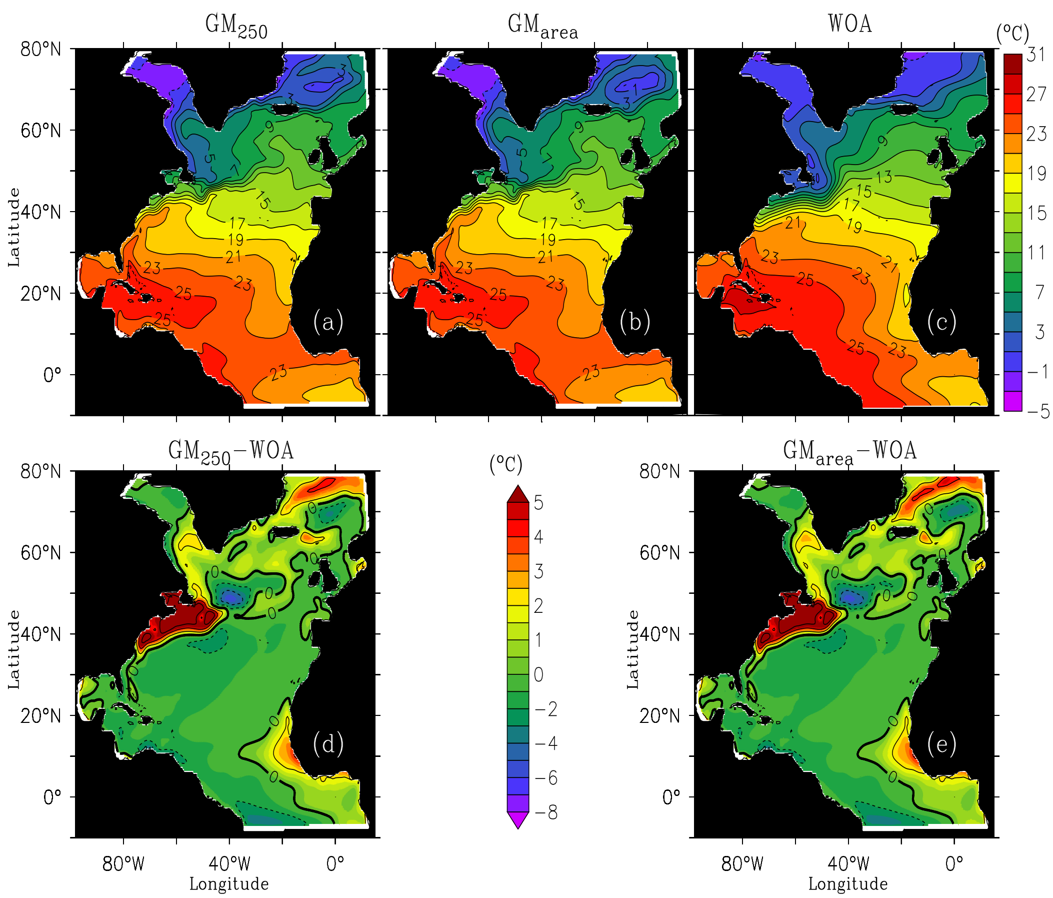

Figure 4.1: 10^{th} year annual mean temperature for GM_{250} (a), GM_{area}(b) and difference from WOA(c) are in (d) and (e) respectively for the first 100m layer

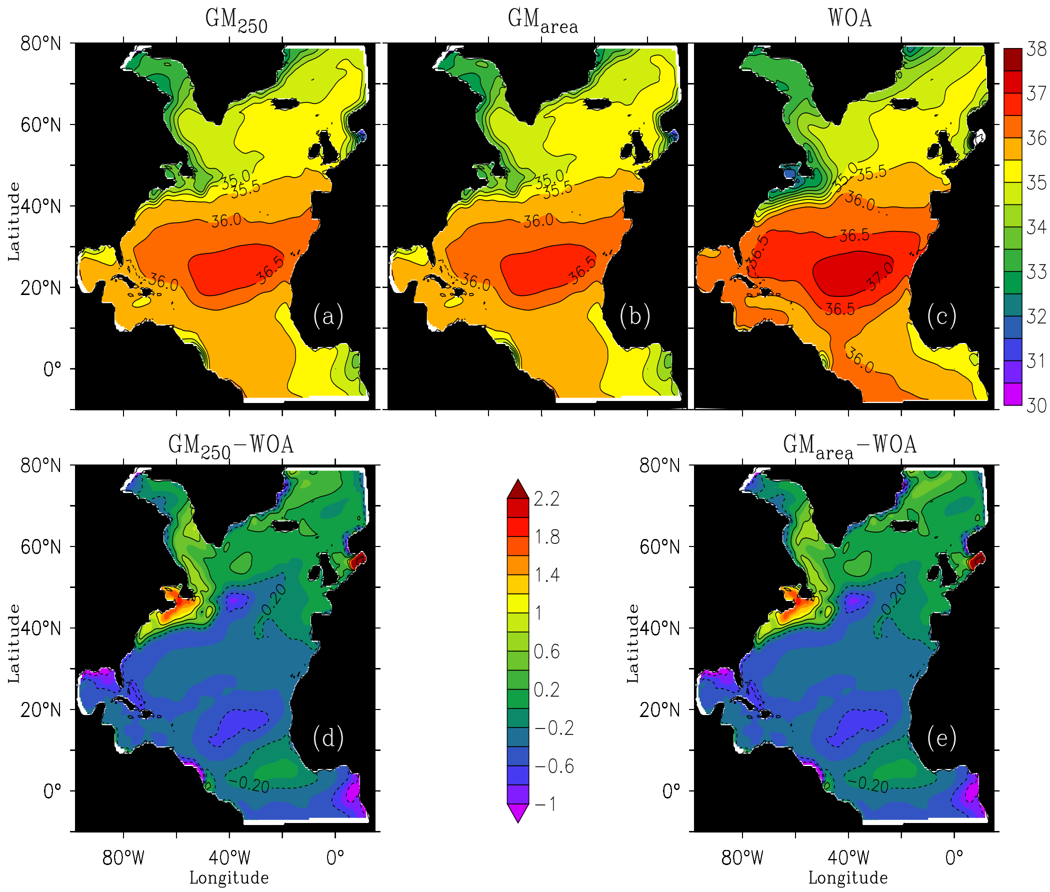

Figure 4.2: 10^{th} year annual mean salinity for GM_{250} (a), GM_{area}(b) and difference from WOA(c) are in (d) and (e) respectively for the first 100m layer

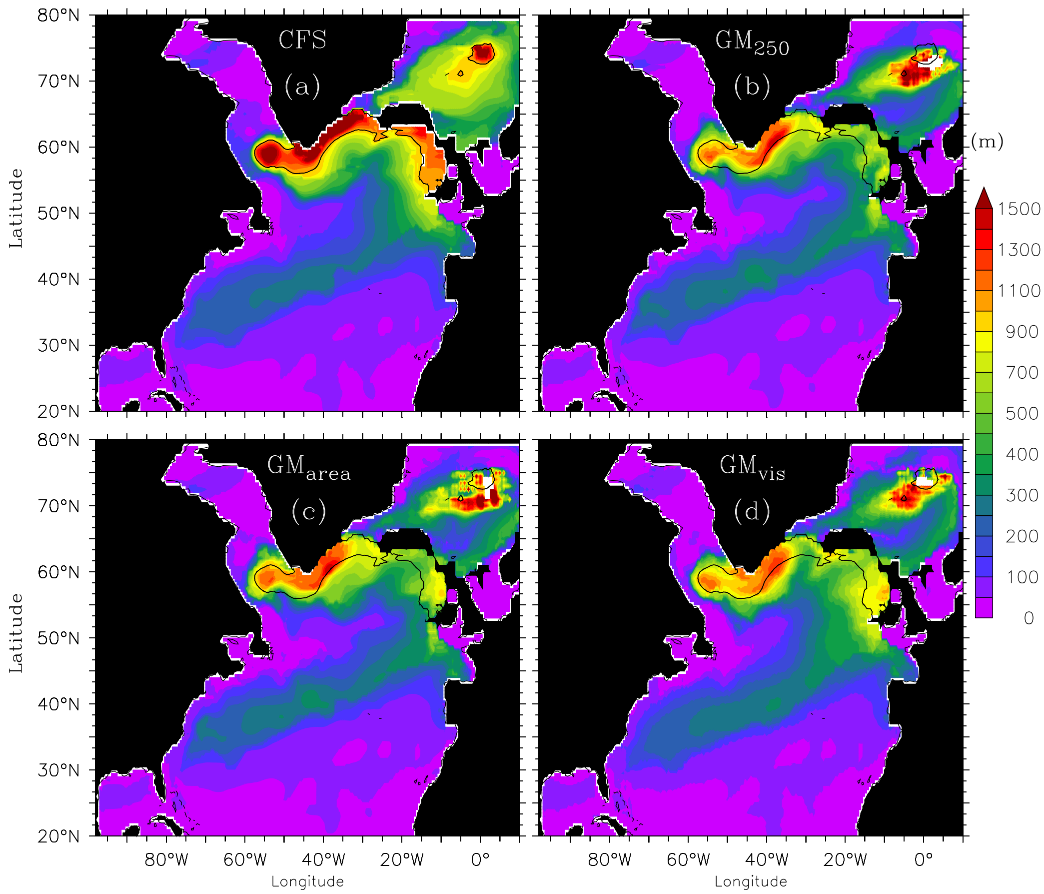

Figure 4.3: 10^{th} year winter (JFM) mean MLD for CFS (a), GM_{250}(b), GM_{area} and GM_{vis}

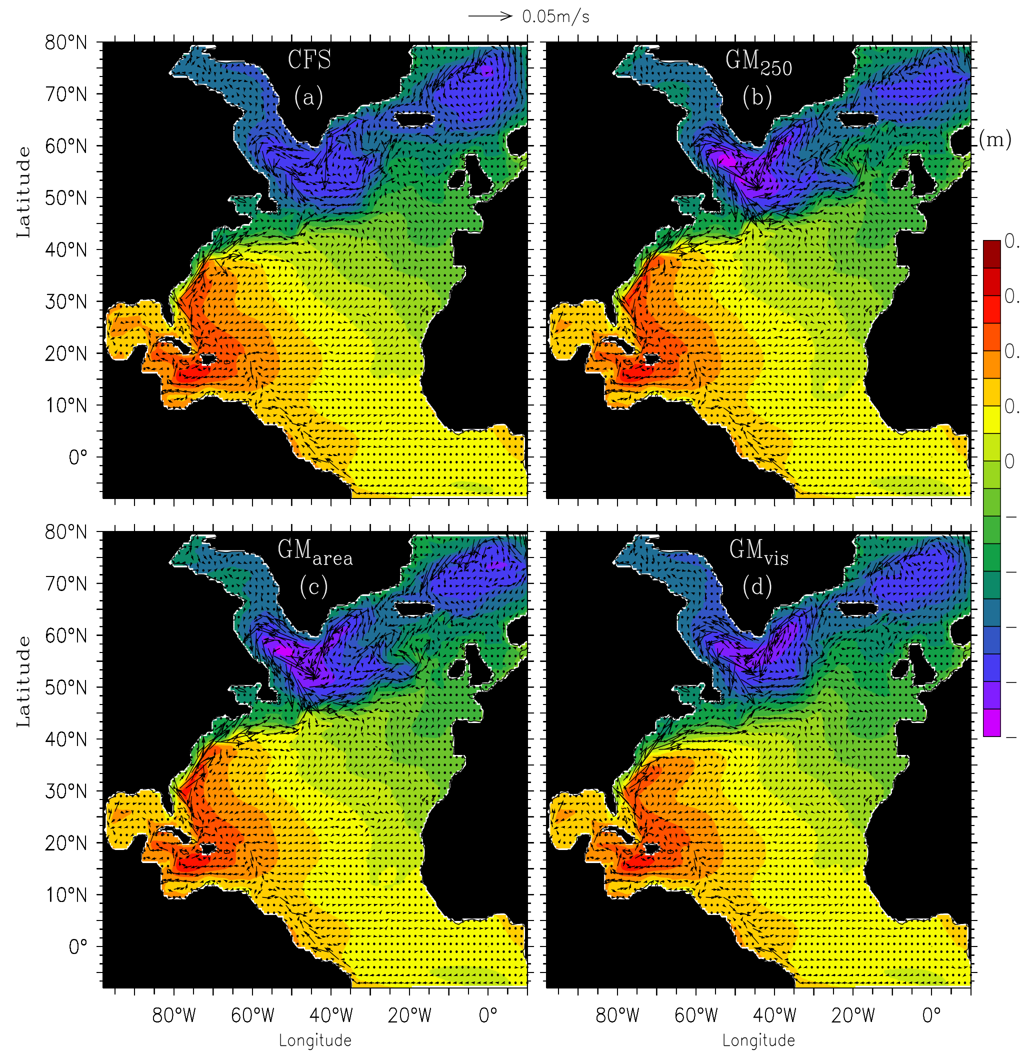

Figure 4.4: 10^{th} year annual mean SSH for CFS (a), GM_{250}(b), GM_{area} and GM_{vis} overlayed with mean currents

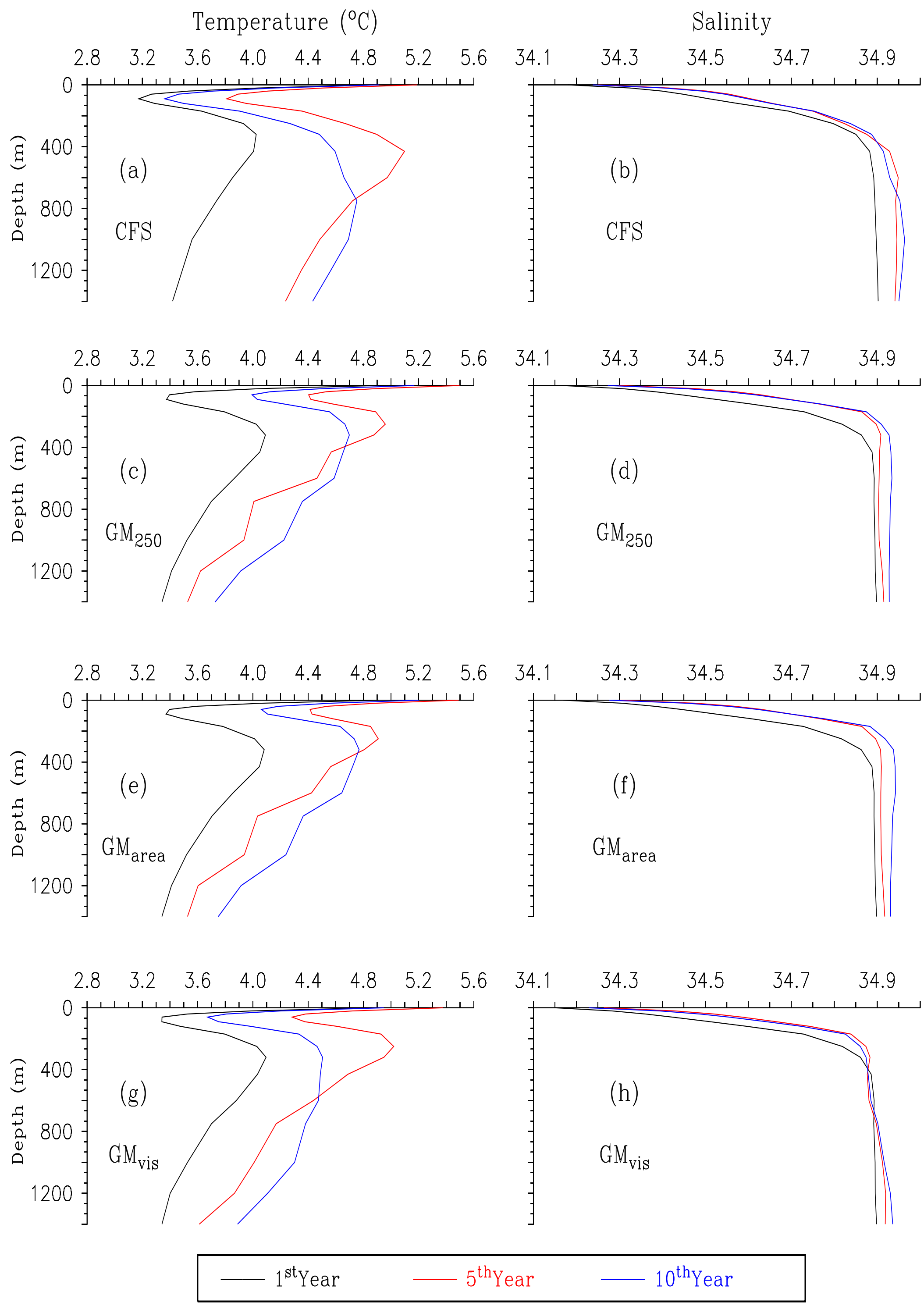

Figure 4.5: Vertical profiles of temperature (Column-1) and salinity (Column-2) in the Labrador Sea region for CFS, GM_{250}, GM_{area} and GM_{vis} for the 1^{st}, 5^{th} and 10^{th} year of the simulations

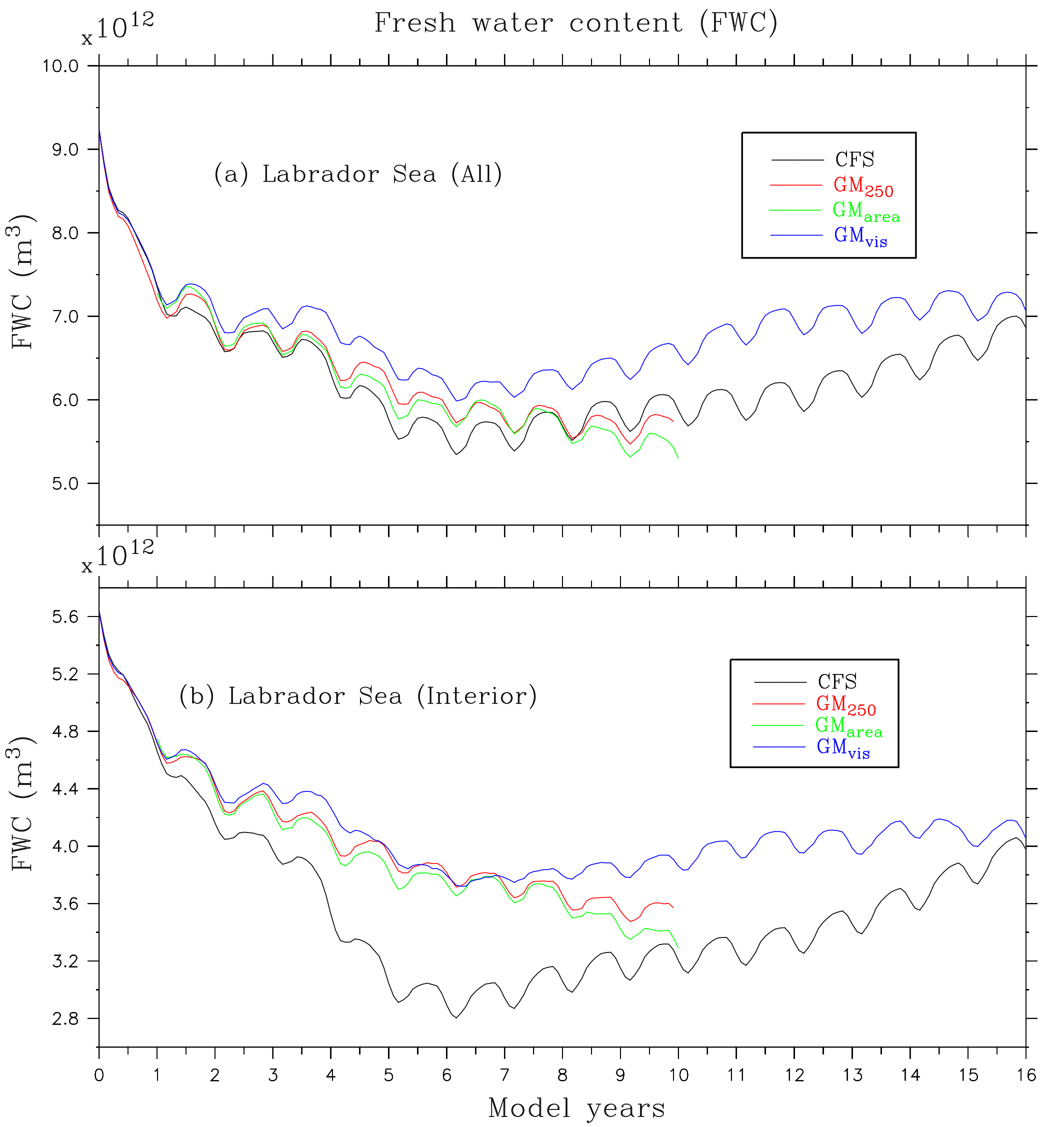

Figure 4.6: Freshwater content of CFS (black line), GM_{250} (red line), GM_{area} (blue line) and GM_{vis} (magenta line) for the (a) Labrador Sea ($53^oN - 63^oN$, $65^oW - 44^oW$) and (b) Interior Labrador Sea (depth $> 3000m$)

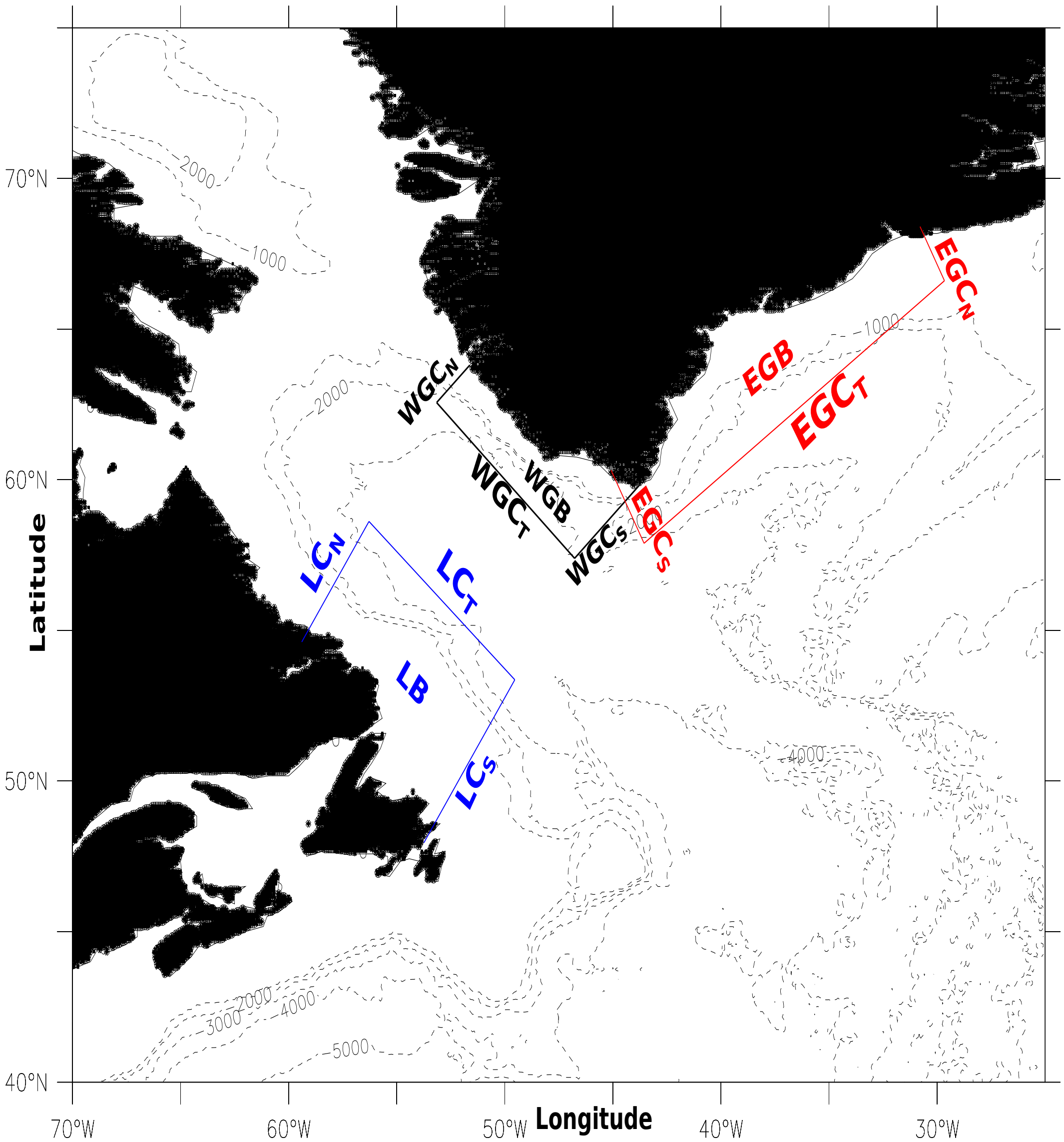

Figure 4.7: Vertical transect locations around the Greenland and Labrador coasts

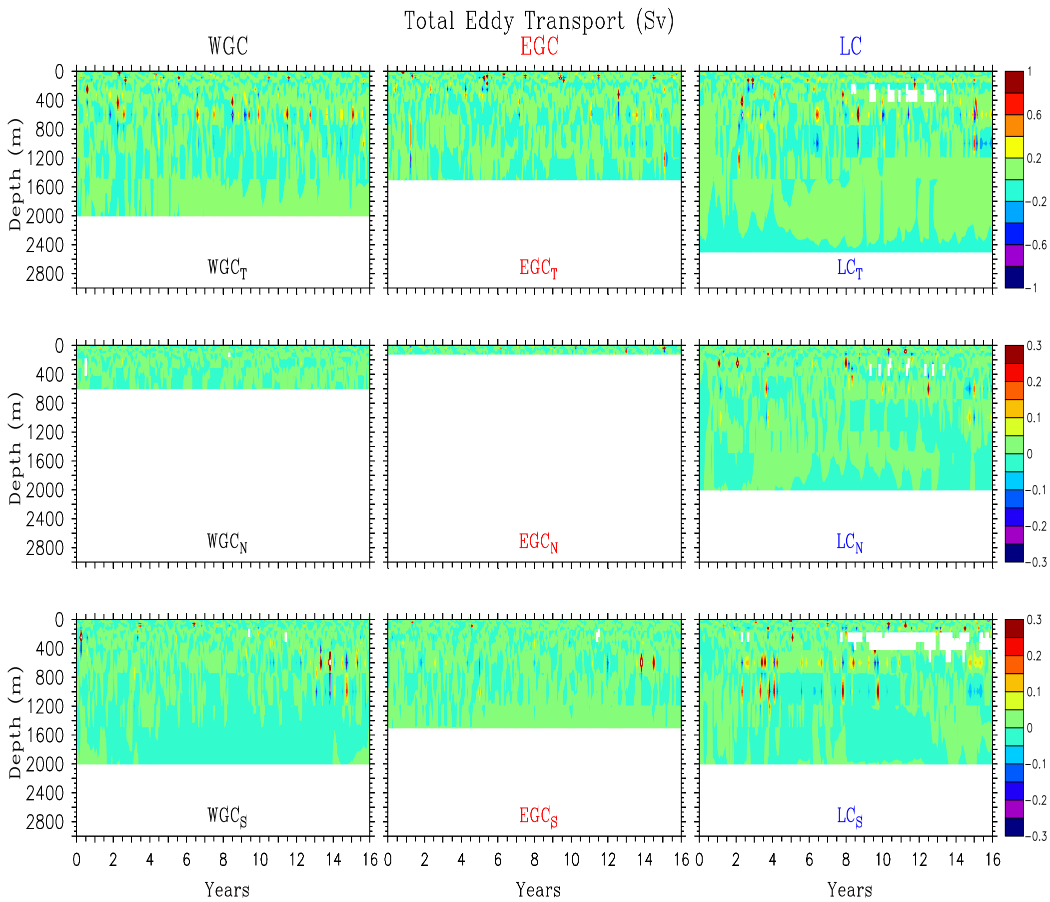

Figure 4.8: Hovmoller diagram of total eddy transport across the sections shown in Figure-4.7 for GM_{vis} experiment

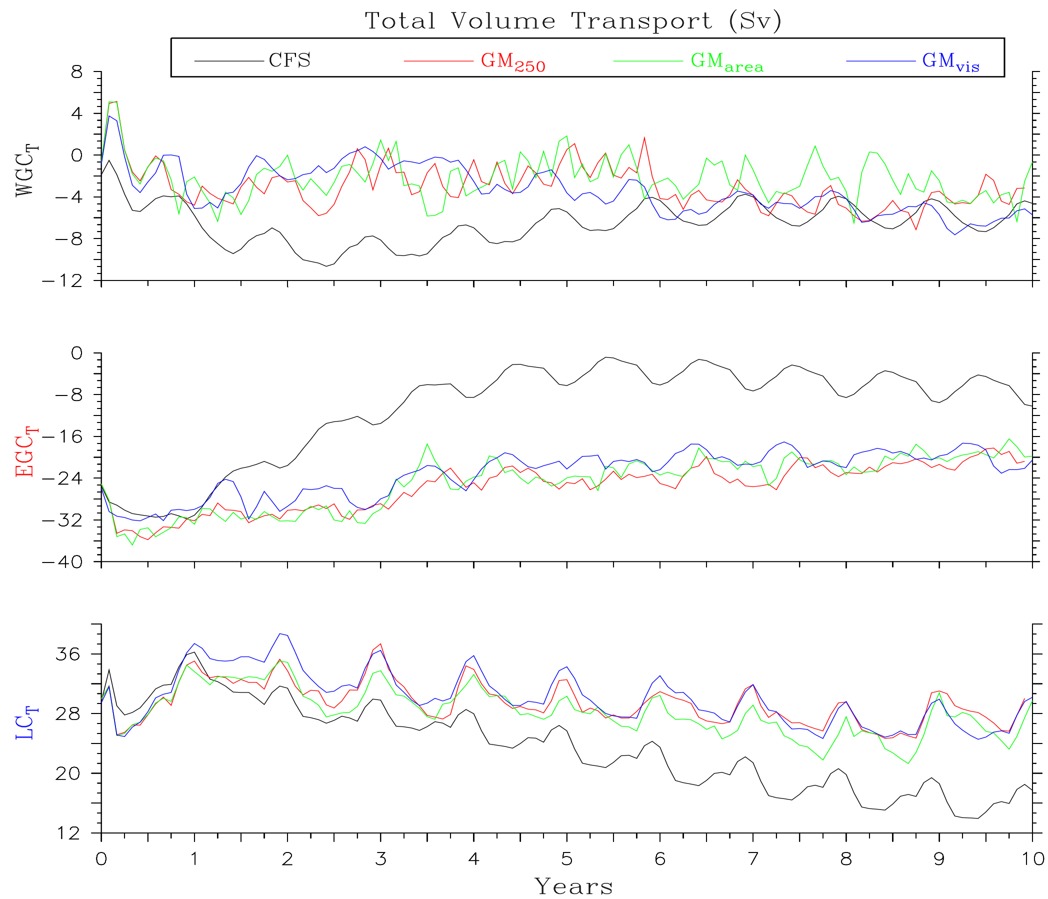

Figure 4.9: Time series of total volume transport (Sv) for CFS, GM_{250}, GM_{area} and GM_{vis} for sections WGC_T, EGC_T and LC_T respectively. Positive values shows transports into the box WGB, EGB or LB and negative is export

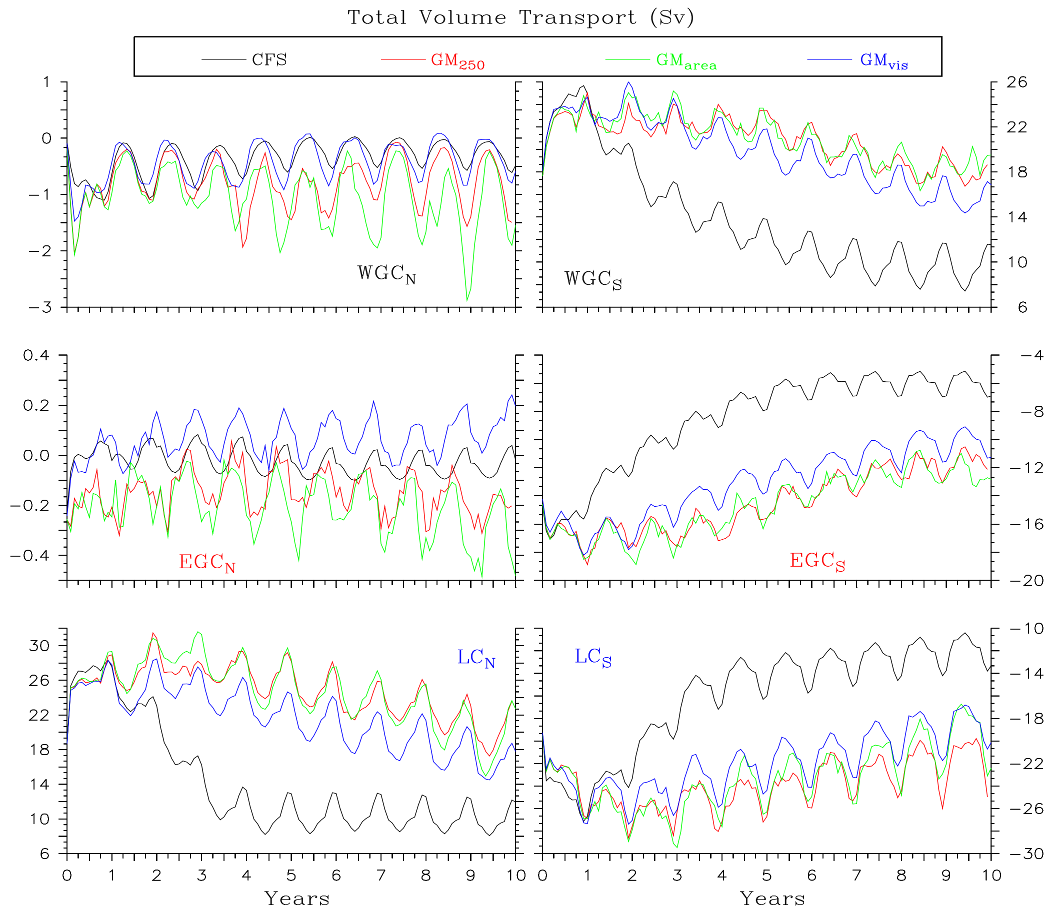

Figure 4.10: Time series of total volume transport (Sv) for CFS, GM_{250}, GM_{area} and GM_{vis} for sections WGC_N, WGC_S, EGC_N, EGC_S, LC_N and LC_S respectively. Positive values shows transports into the box WGB, EGB or LB and negative is export

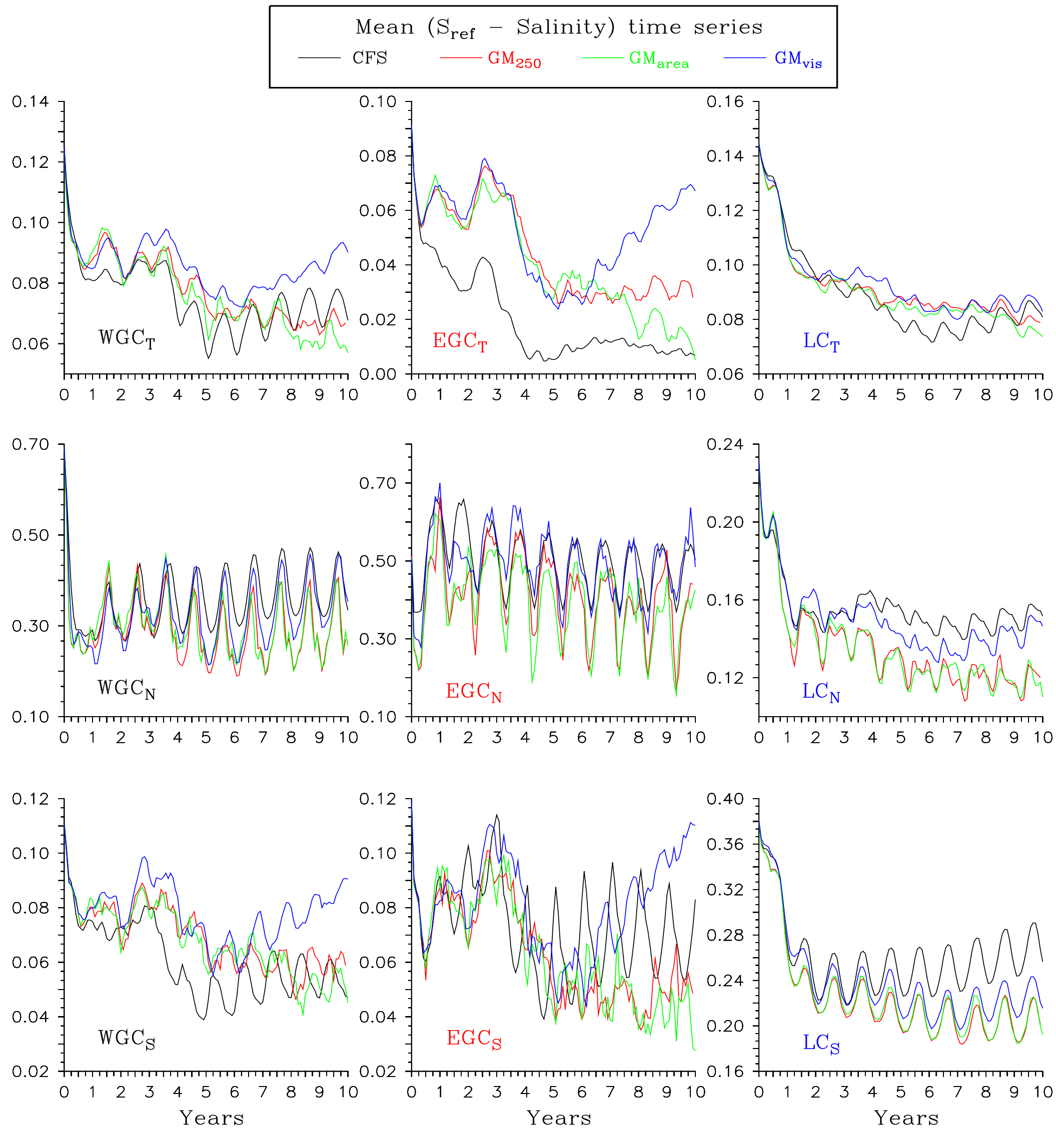

Figure 4.11: Mean S_{ref}-salinity ($S_{ref} = 35$) time series for sections of WGB, EGB and LB boxes shown in Figure-4.7 for CFS, GM_{250}, GM_{area} and GM_{vis} experiments

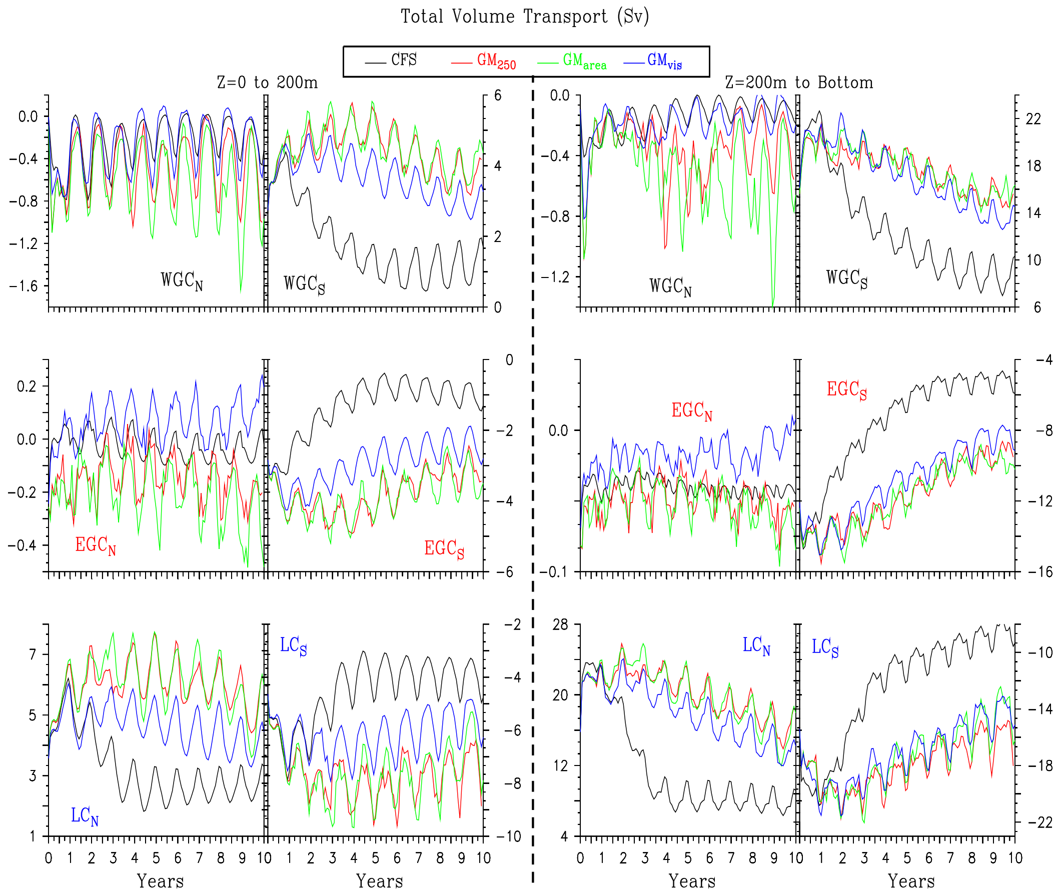

Figure 4.12: Time series of total volume transport (Sv) for CFS, GM_{250}, GM_{area} and GM_{vis} for sections WGC_N, WGC_S, EGC_N, EGC_S, LC_N and LC_S respectively. Positive values shows transports into the box WGB, EGB or LB and negative is export. The left two columns are for depth range from 0 to 200m and the right two columns are for the depth range from 200 to bottom

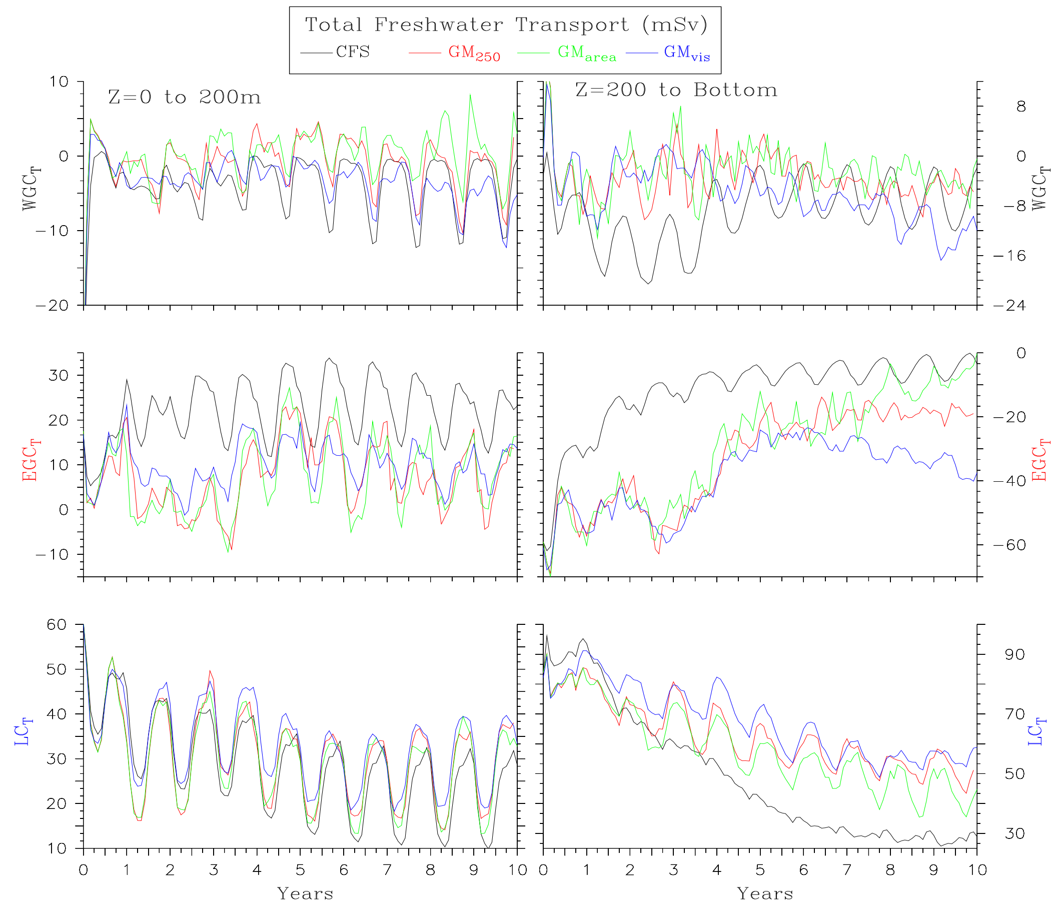

Figure 4.13: Time series of total freshwater transport (mSv) for CFS, GM_{250}, GM_{area} and GM_{vis} for sections WGC_T, EGC_T and LC_T respectively. Positive values shows transports into the box WGB, EGB or LB and negative is export. The left column is for depth range from 0 to 200m and the right column is for the depth range from 200 to bottom

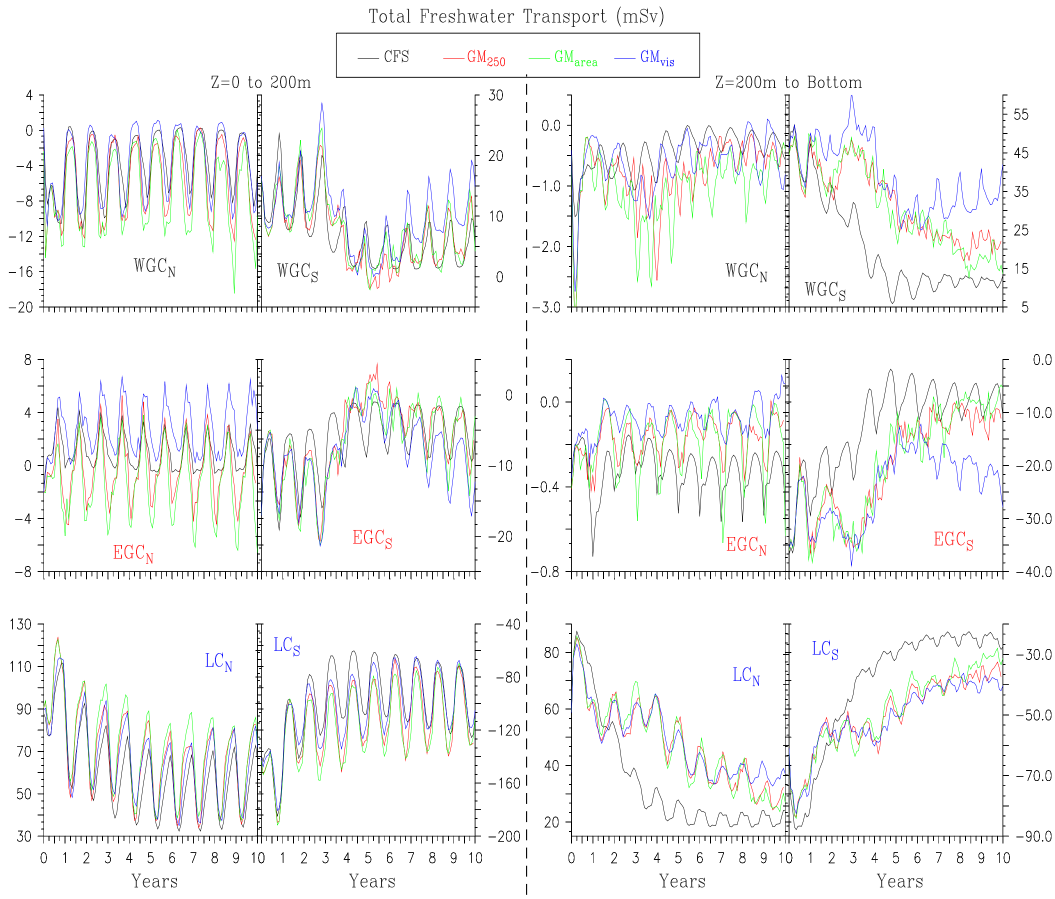

Figure 4.14: Time series of total freshwater transport (mSv) for CFS, GM_{250}, GM_{area} and GM_{vis} for sections WGC_N, WGC_S, EGC_N, EGC_S, LC_N and LC_S respectively. Positive values shows transports into the box WGB, EGB or LB and negative is export. The left two columns are for depth range from 0 to 200m and the right two columns are for the depth range from 200 to bottom

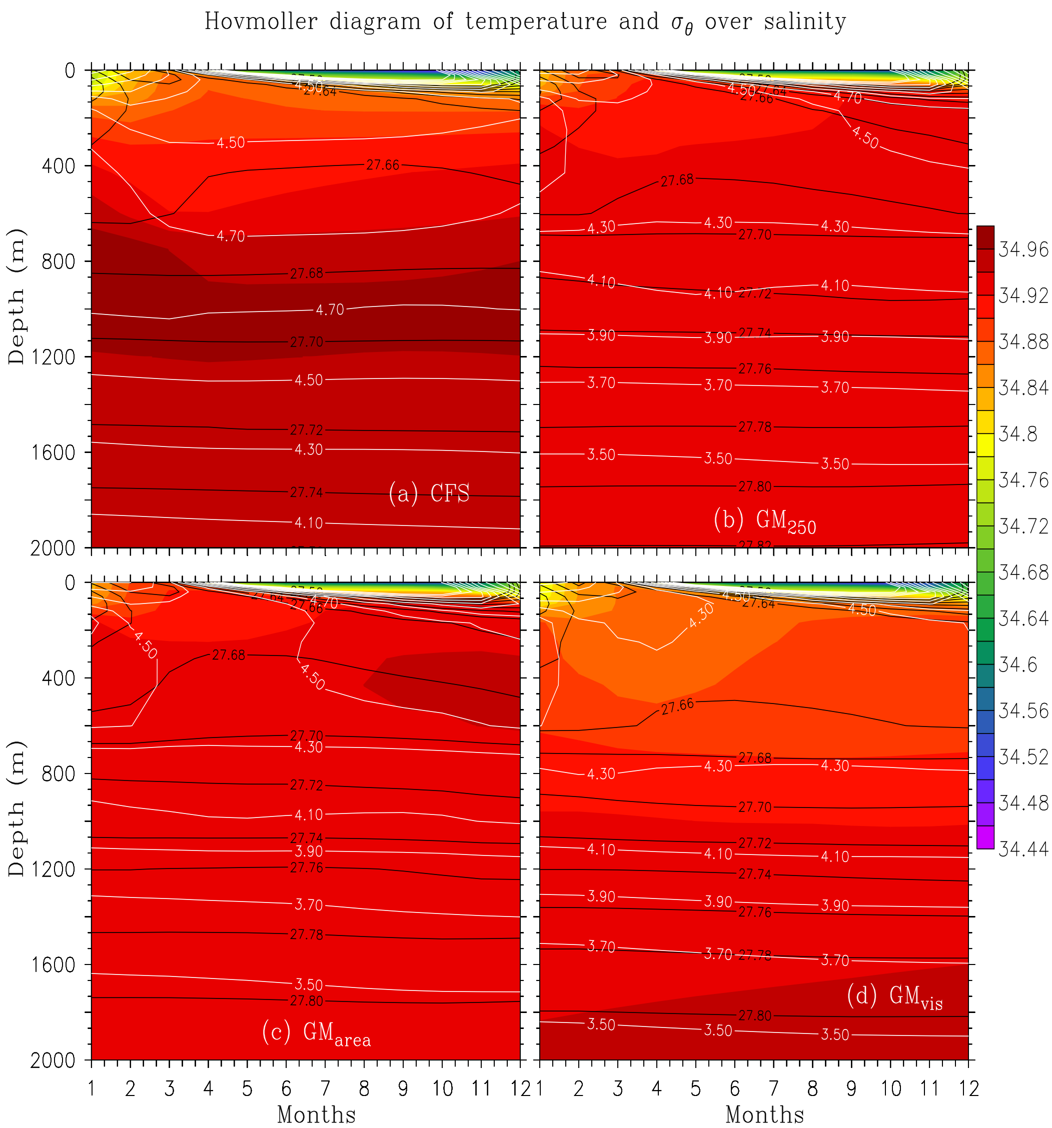

Figure 4.15: Hovmoller diagram of 10^{th} model year temperature (white line) and σ_θ (black line) in kg m^{-3} over salinity (color filled) for the Labrador Sea interior for CFS (a), GM_{250} (b), GM_{area} (c) and GM_{vis} (d) experiments

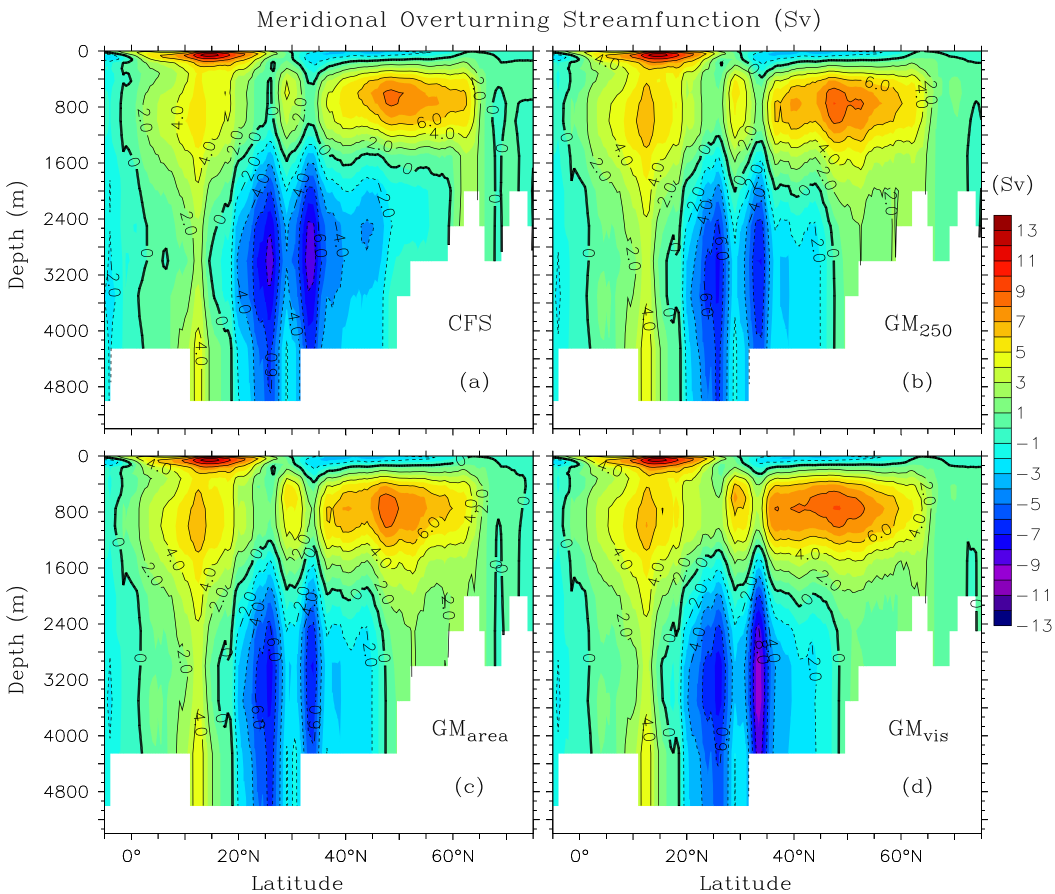

Figure 4.16: 10^{th} year mean MOC for CFS (a), GM_{250}(b), GM_{area} and GM_{vis}

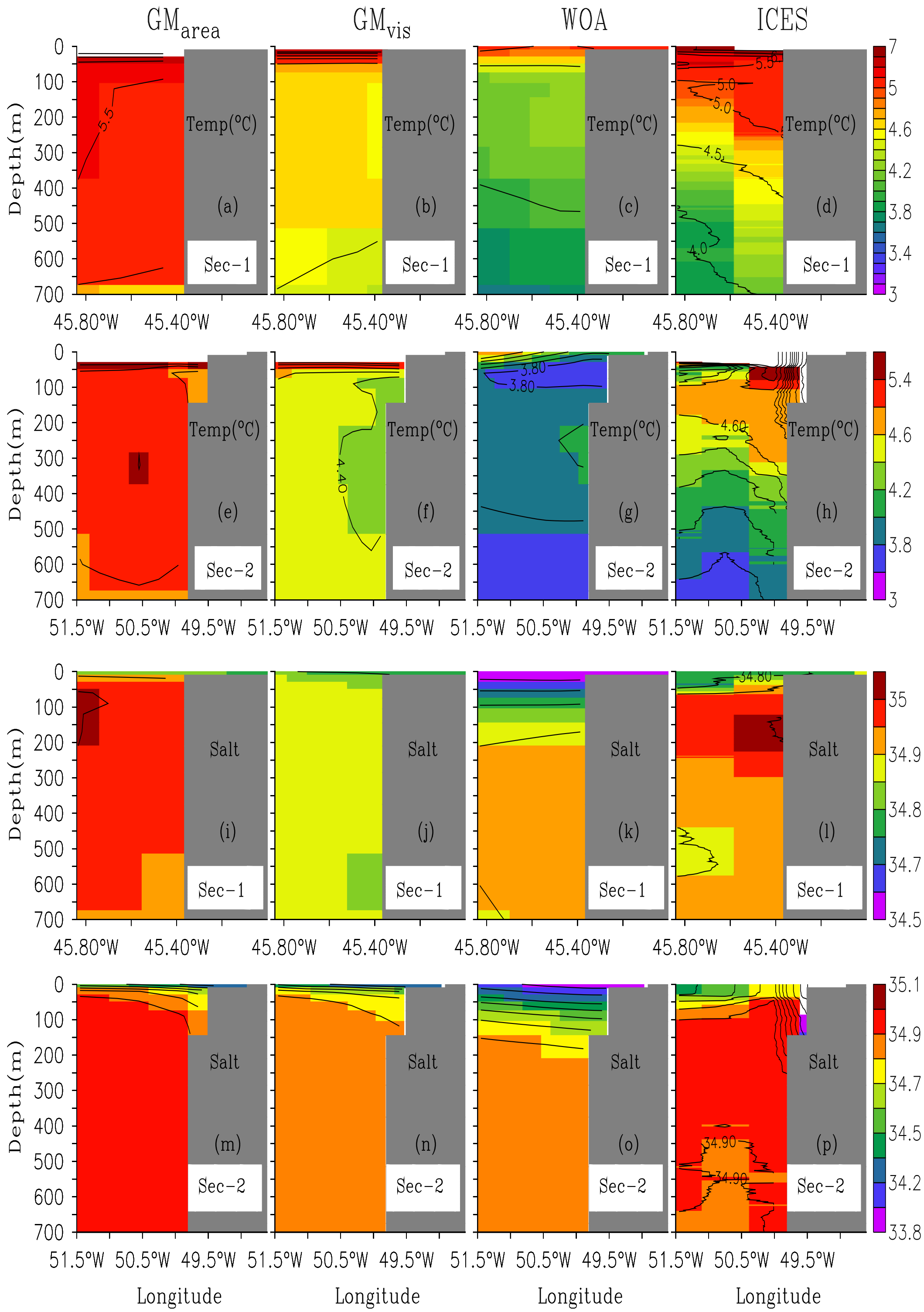

Figure 4.17: 10^{th}year summer mean (June-July) temperature for Cape Farewell (Sec-1) for the GM_{area} (a) and GM_{vis} (b) cases and salinity (i,j) along with the respective WOA data (c,k) and ICES data (d,l) . For Cape Desolation (Sec-2) model temperatures (e,f) and salinity (m,n) along with the respective WOA data (g,o) and ICES data (h,p)

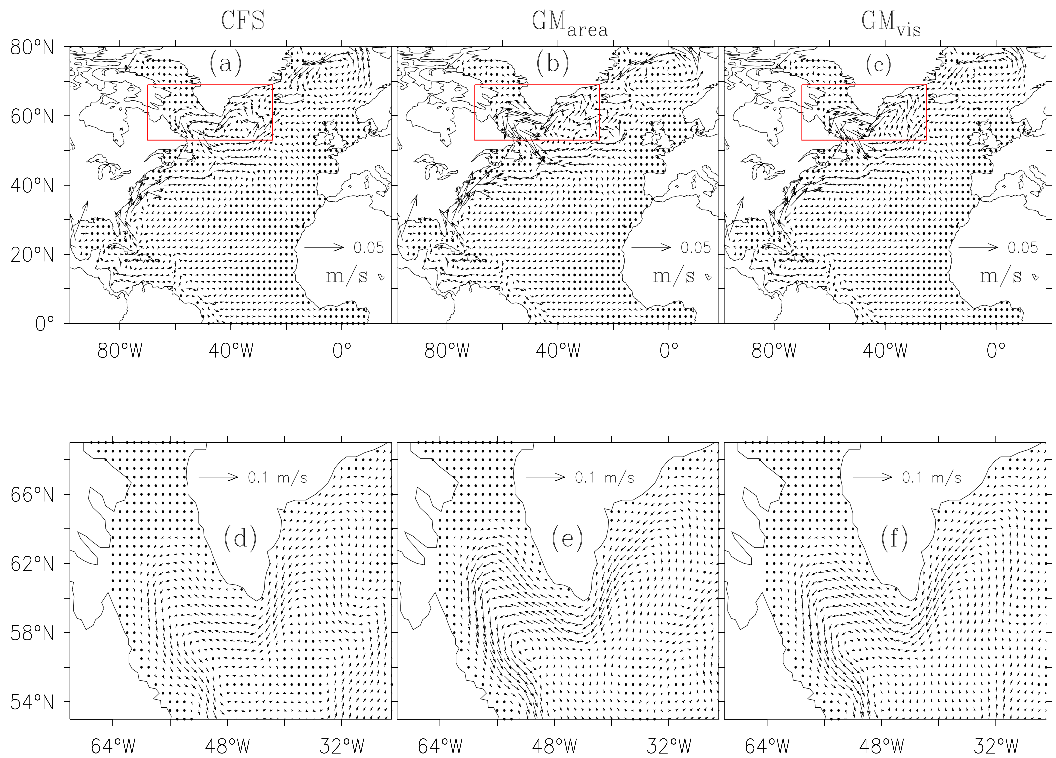

Figure 4.18: Mean currents from 10^{th} year of the CFS(a), GM_{area}(b), GM_{vis}(c). Currents inside the red boxes are shown in the bottom panel (d,e,f) for each run

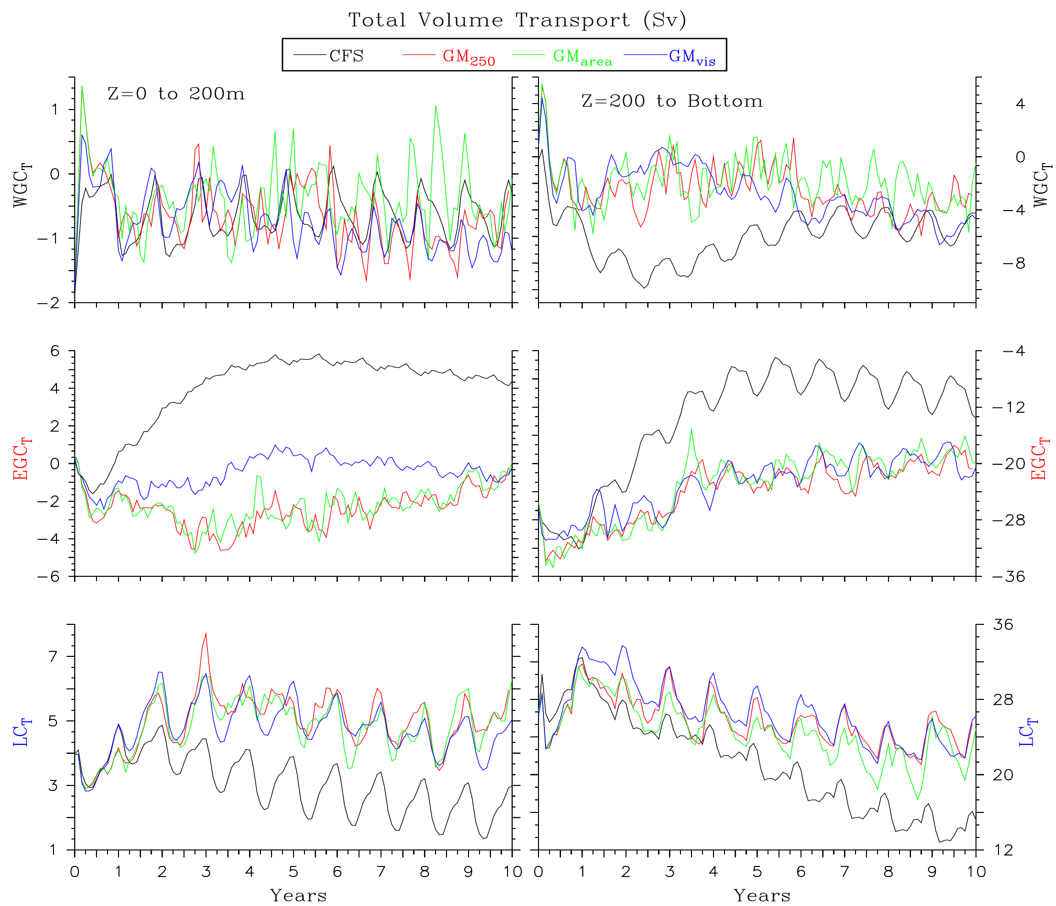

Figure 4.19: Time series of total volume transport (Sv) for CFS, GM_{250}, GM_{area} and GM_{vis} for sections WGC_T, EGC_T and LC_T respectively. Positive values shows transports into the box WGB, EGB or LB and negative is export. The left columns are for the depth range from 0 to 200m and the right columns are for the depth range from 200 to bottom

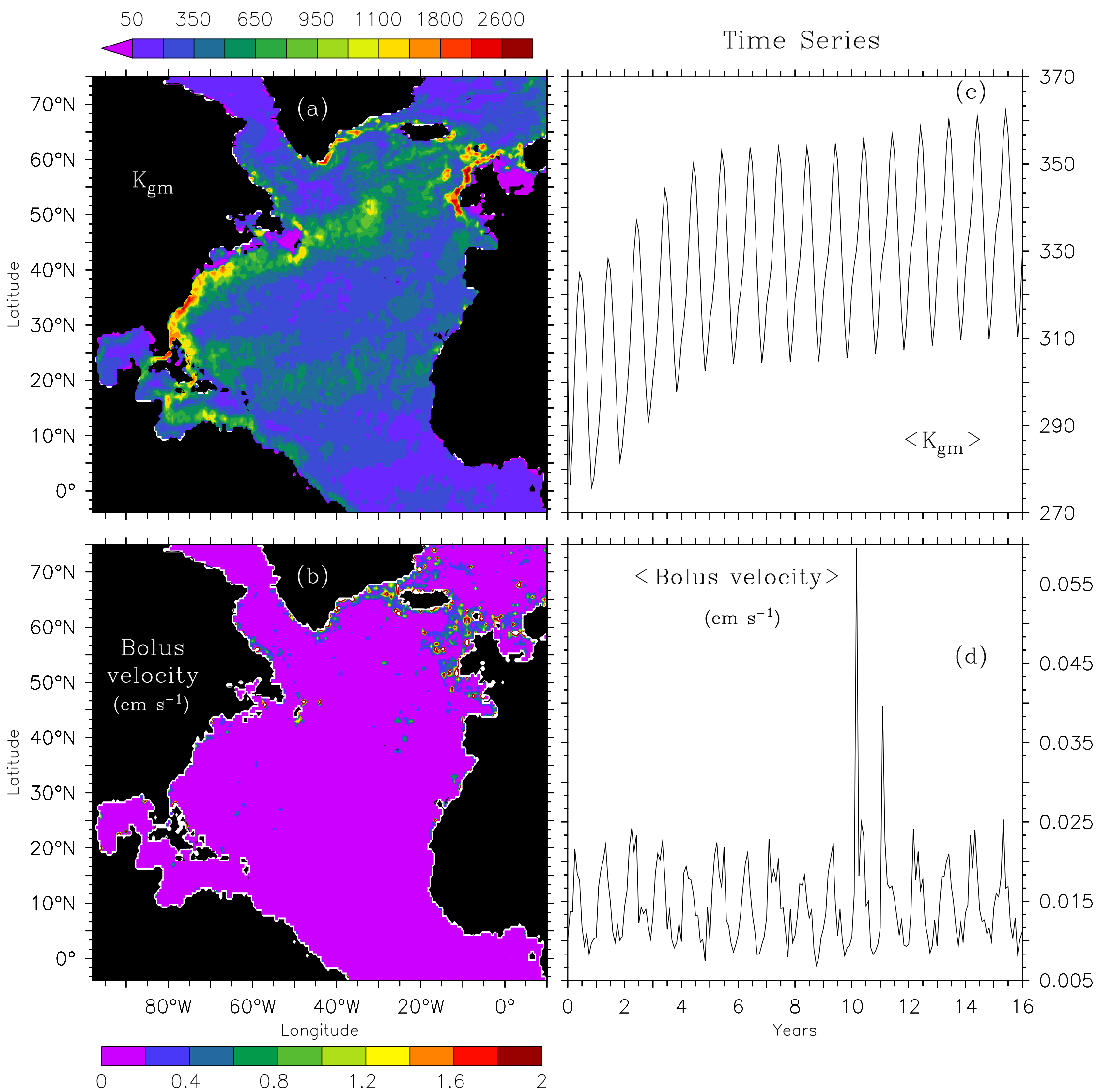

Figure 4.20: 15^{th} year mean K_{gm} (a) and Bolus velocity (b) and corresponding domain average time series on RHS (c) and (d) for GM_{vis} run

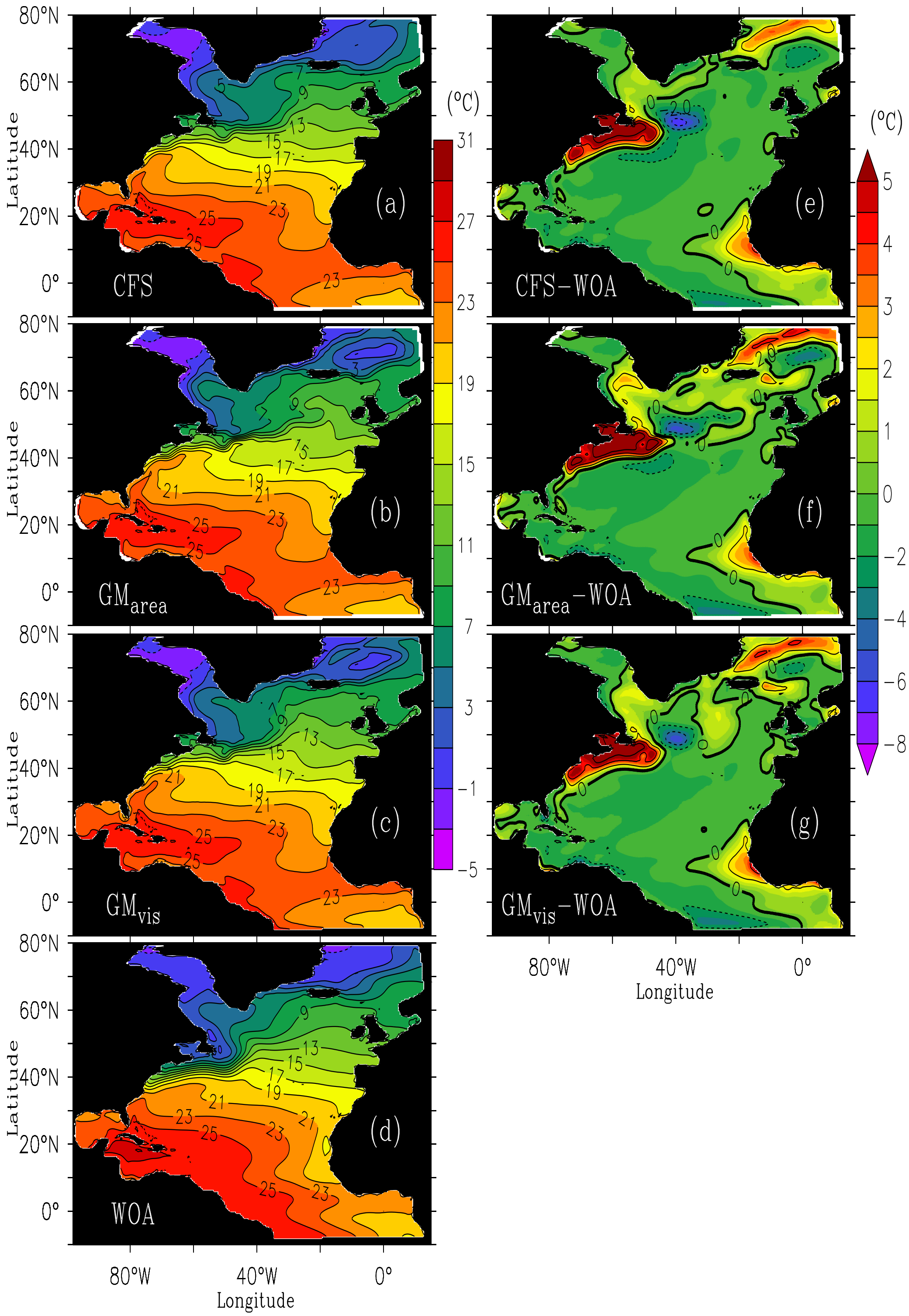

Figure 4.21: 10^{th} year annual mean temperature for CFS (a), GM_{area}(b), GM_{vis} (c) and difference from the WOA(d) are in (e), (f) and (g) respectively for the first 100m layer

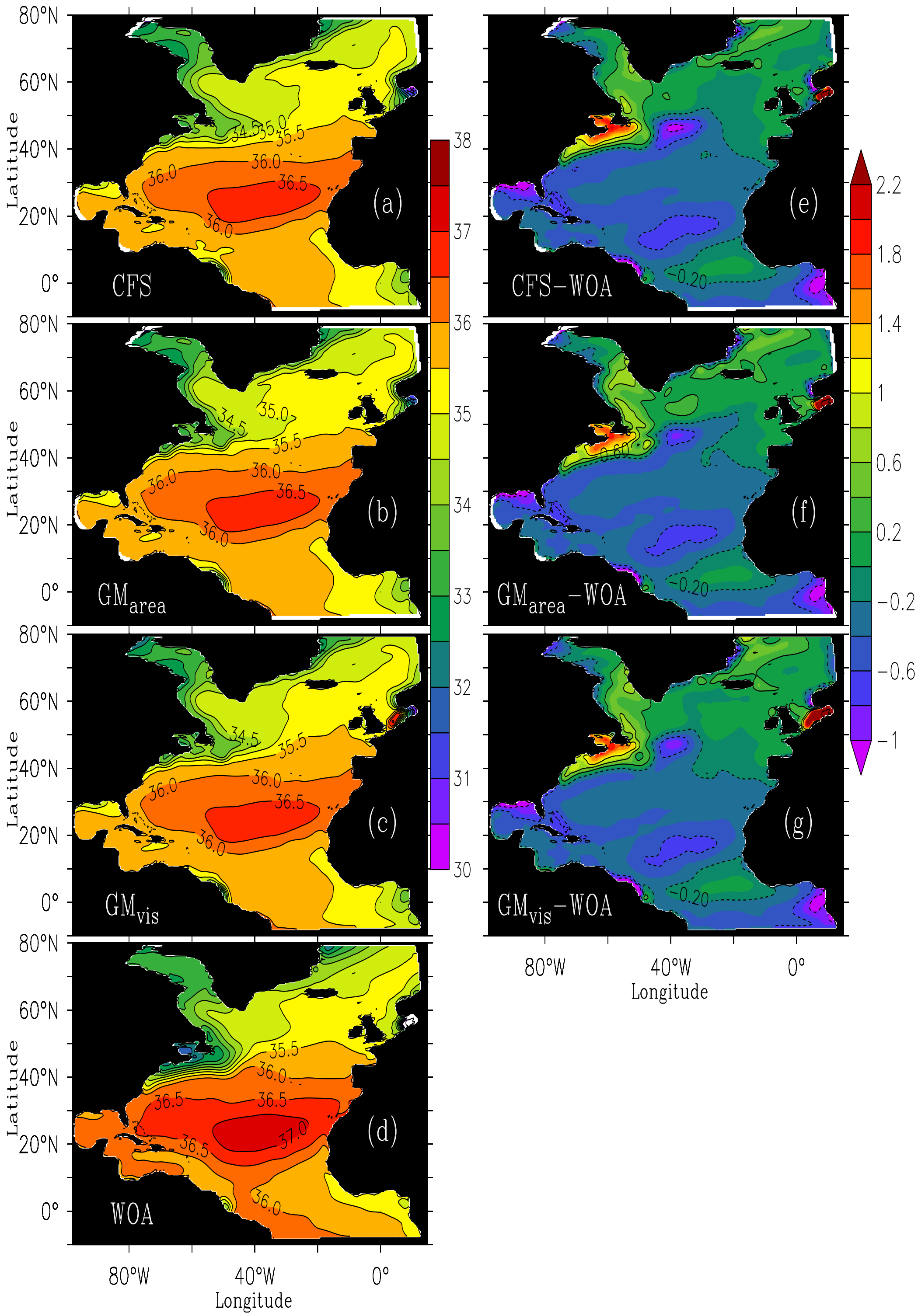

Figure 4.22: 10^{th} year annual mean salinity for CFS (a), GM_{area}(b), GM_{vis} (c) and difference from the WOA(d) are in (e), (f) and (g) respectively for the first 100m layer

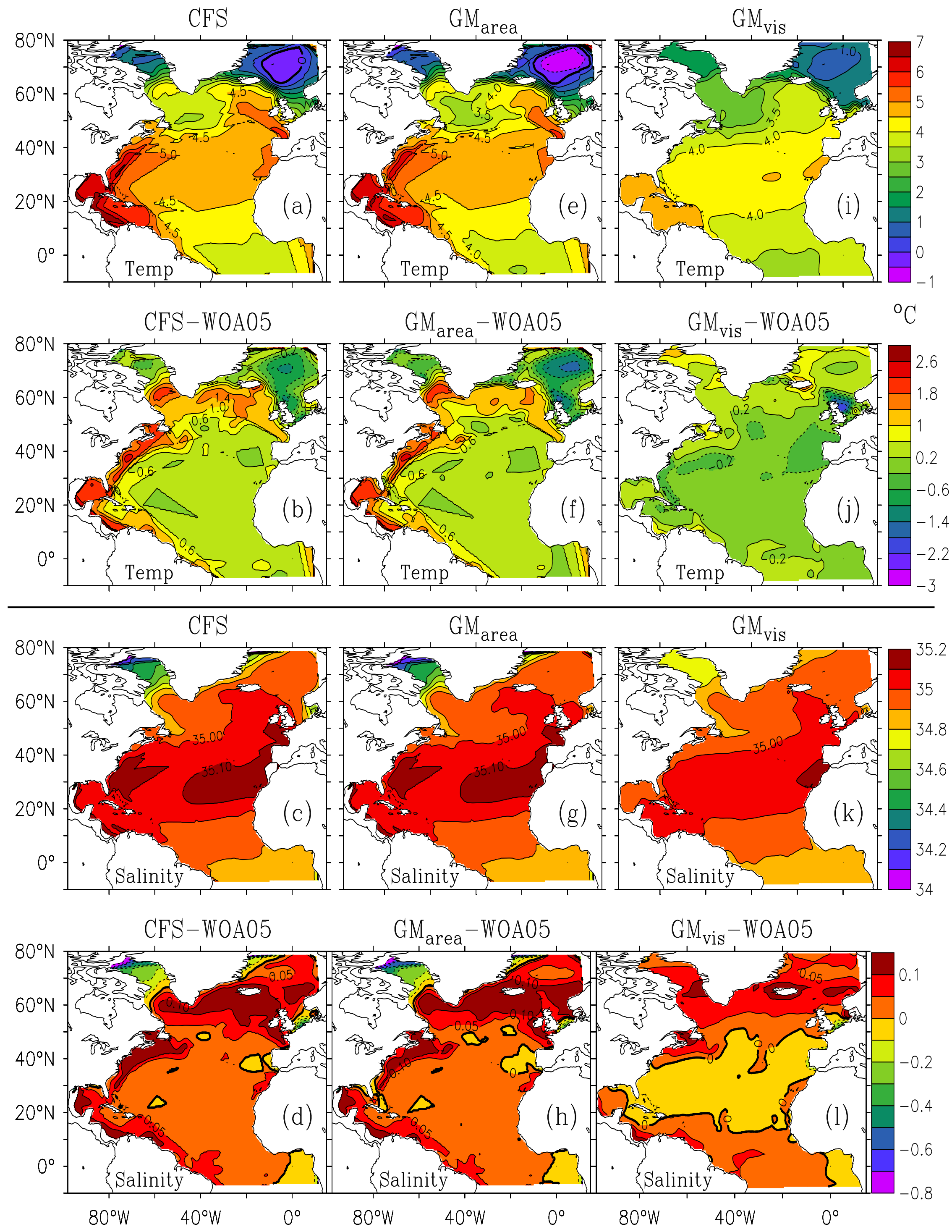

Figure 4.23: 10^{th} year mean temperature and salinity fields (depth average) for CFS, GM_{area} and GM_{vis} in 1^{st} and 3^{rd} row and corresponding differences from the WOA05 climatology, in the 2^{nd} and 4^{th} row respectively.

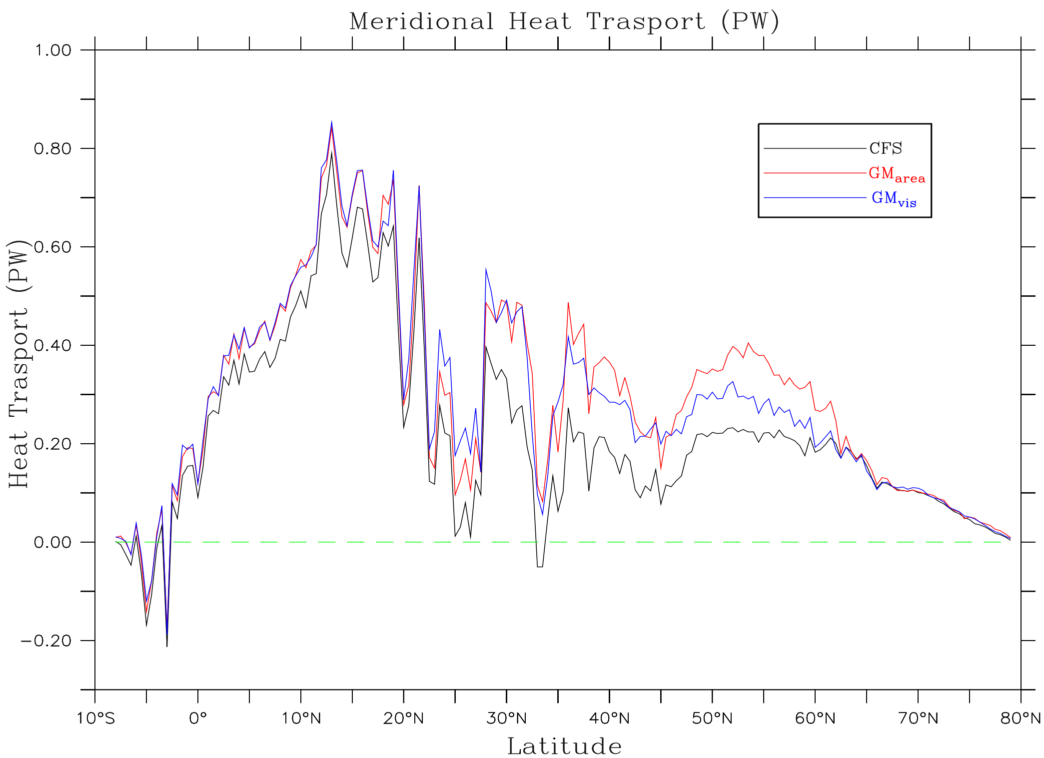

Figure 4.24: 10^{th} year mean meridional heat transport (in PW) for CFS (black line), GM_{area} (red line) and GM_{vis} (blue line) simulations

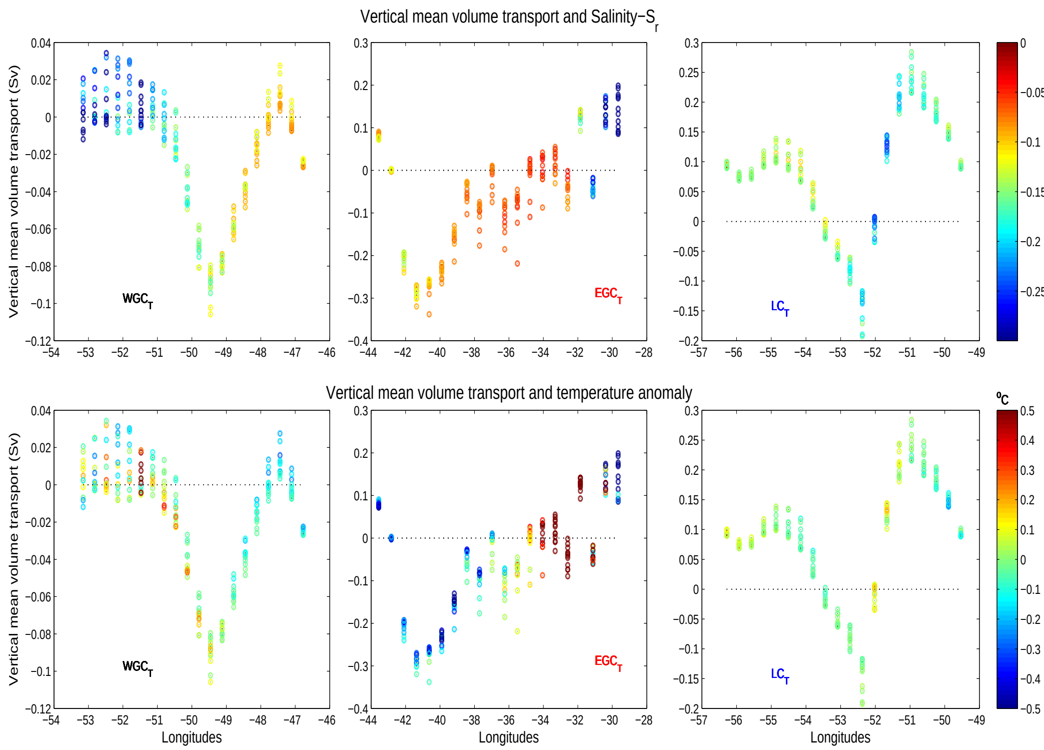

Figure 4.25: 15^{th} year vertical mean volume transport and corresponding vertical mean salinity-35 (first row), vertical mean temperature anomaly (second row) for WGC_T, EGC_T and LC_T sections

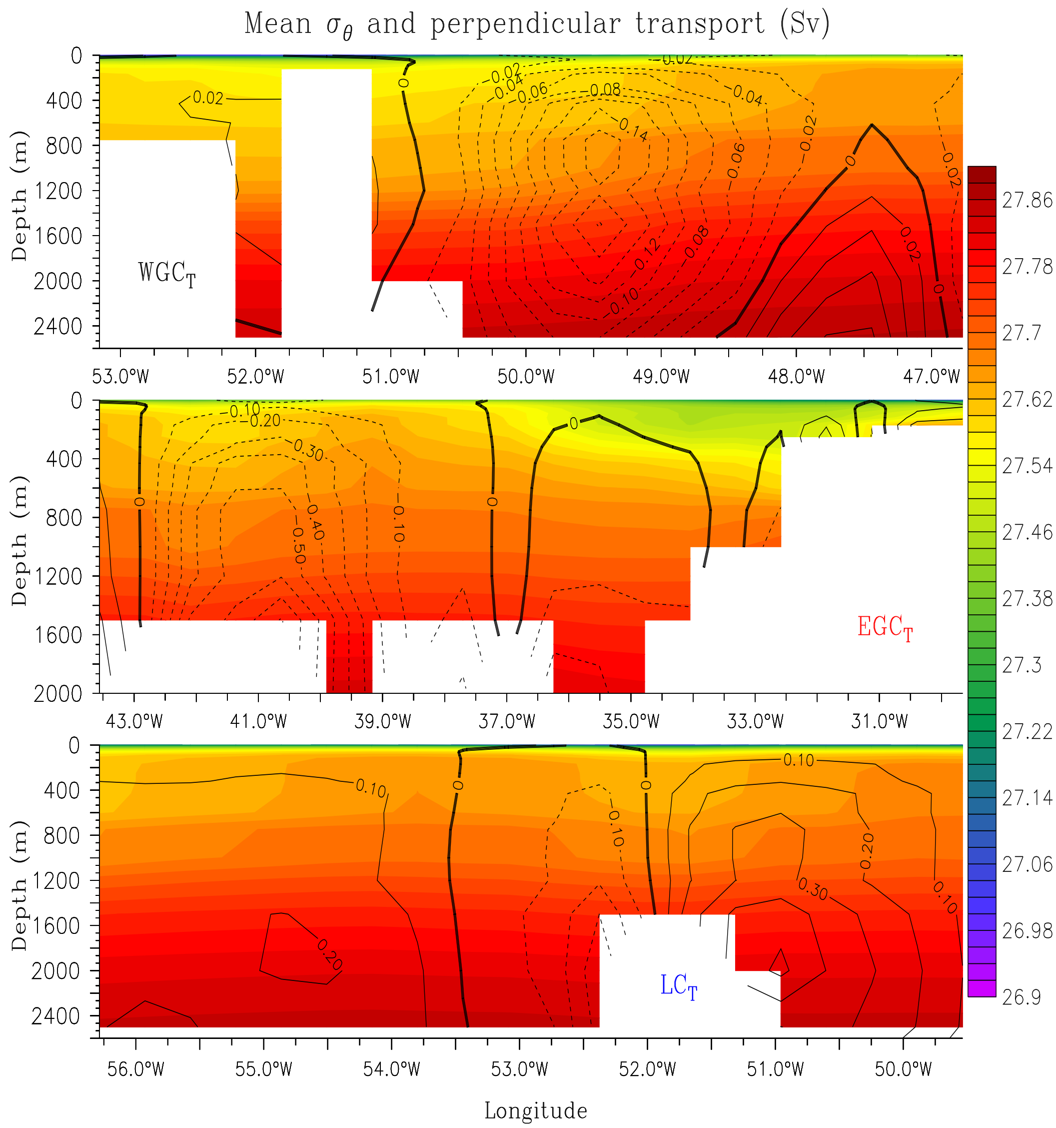

Figure 4.26: 15^{th} year mean σ_θ in kg m^{-3} over perpendicular transport (Sv) from the GM_{vis} experiment. Solid contour shows onshore (positive) and dotted offshore (negative) flow velocities

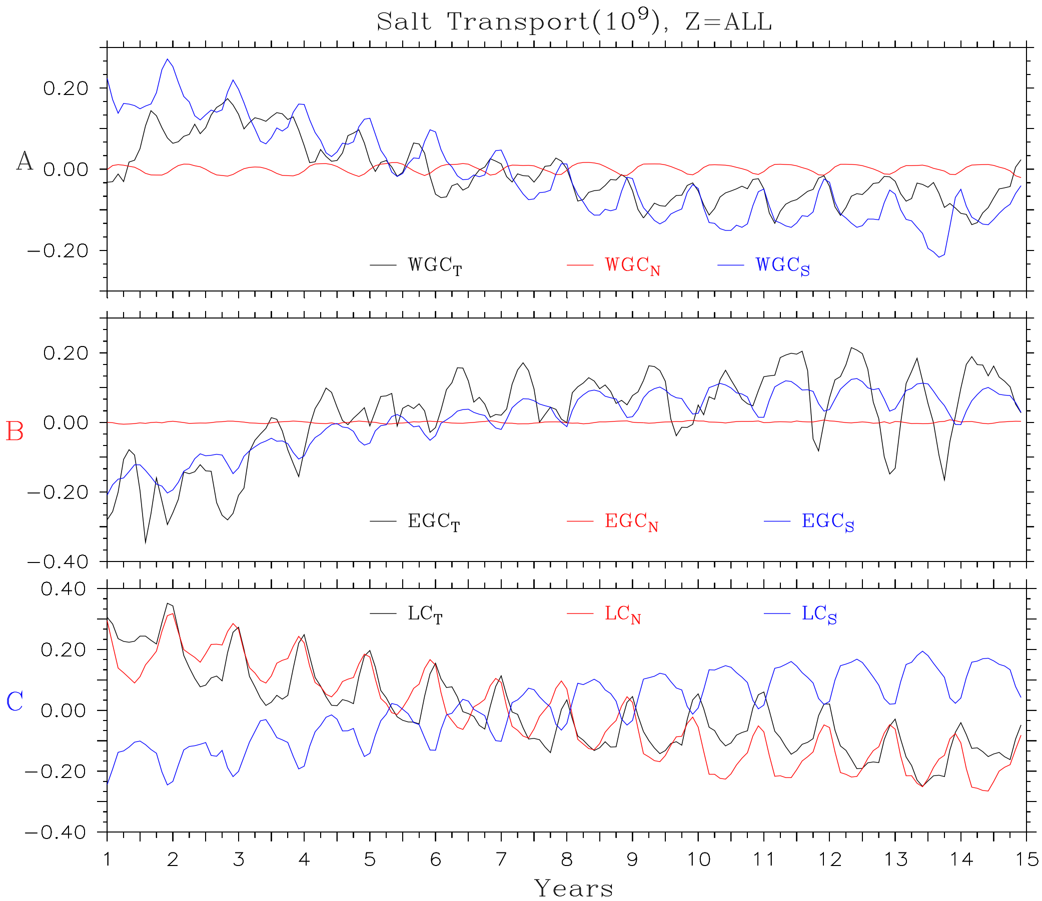

Figure 4.27: Time series of $\overline{S}v'$ for GM_{vis}

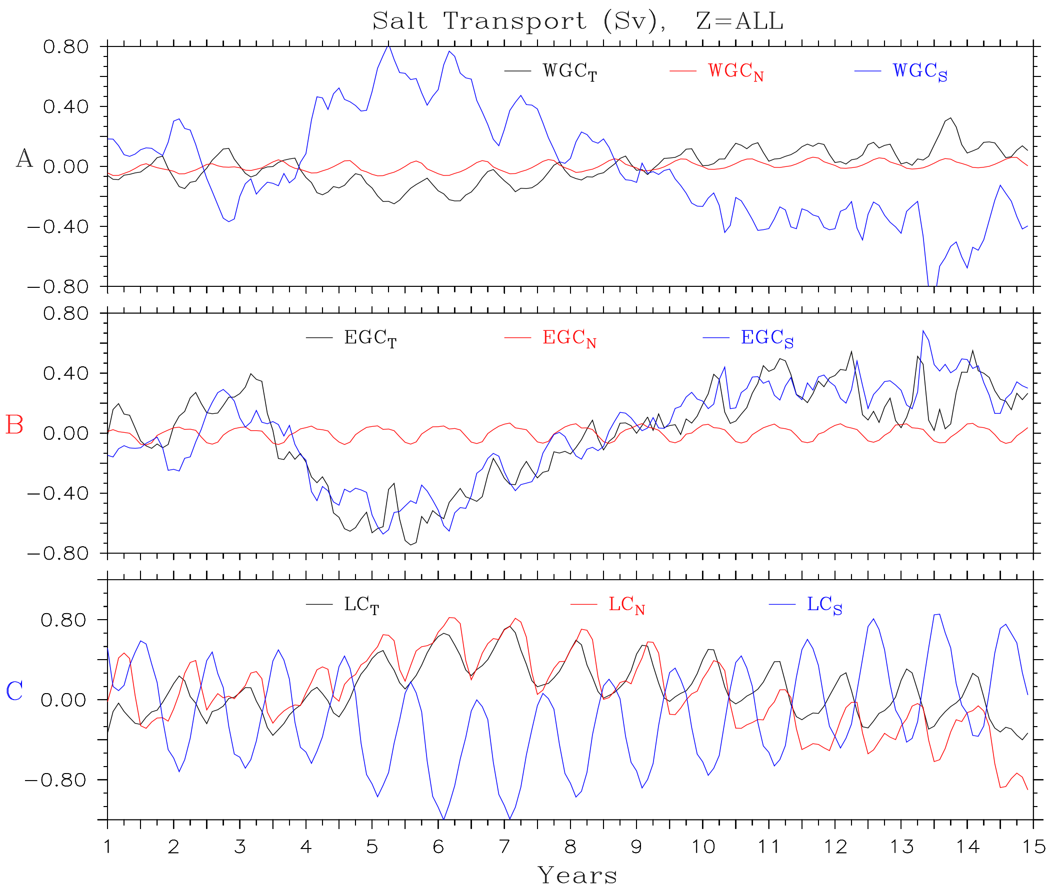

Figure 4.28: Time series of $\overline{v}S'$ for GM_{vis}

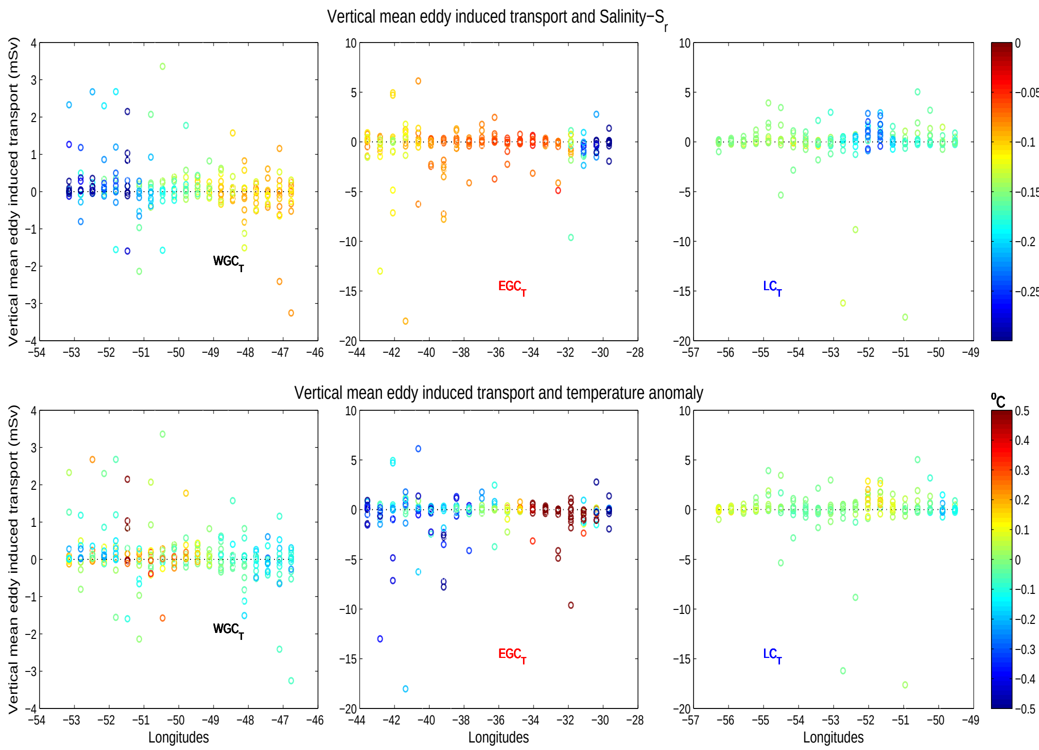

Figure 4.29: 15^{th} year vertical mean eddy induced volume transport and corresponding vertical mean salinity-35 (first row), vertical mean temperature anomaly (second row) for WGC_T, EGC_T and LC_T sections

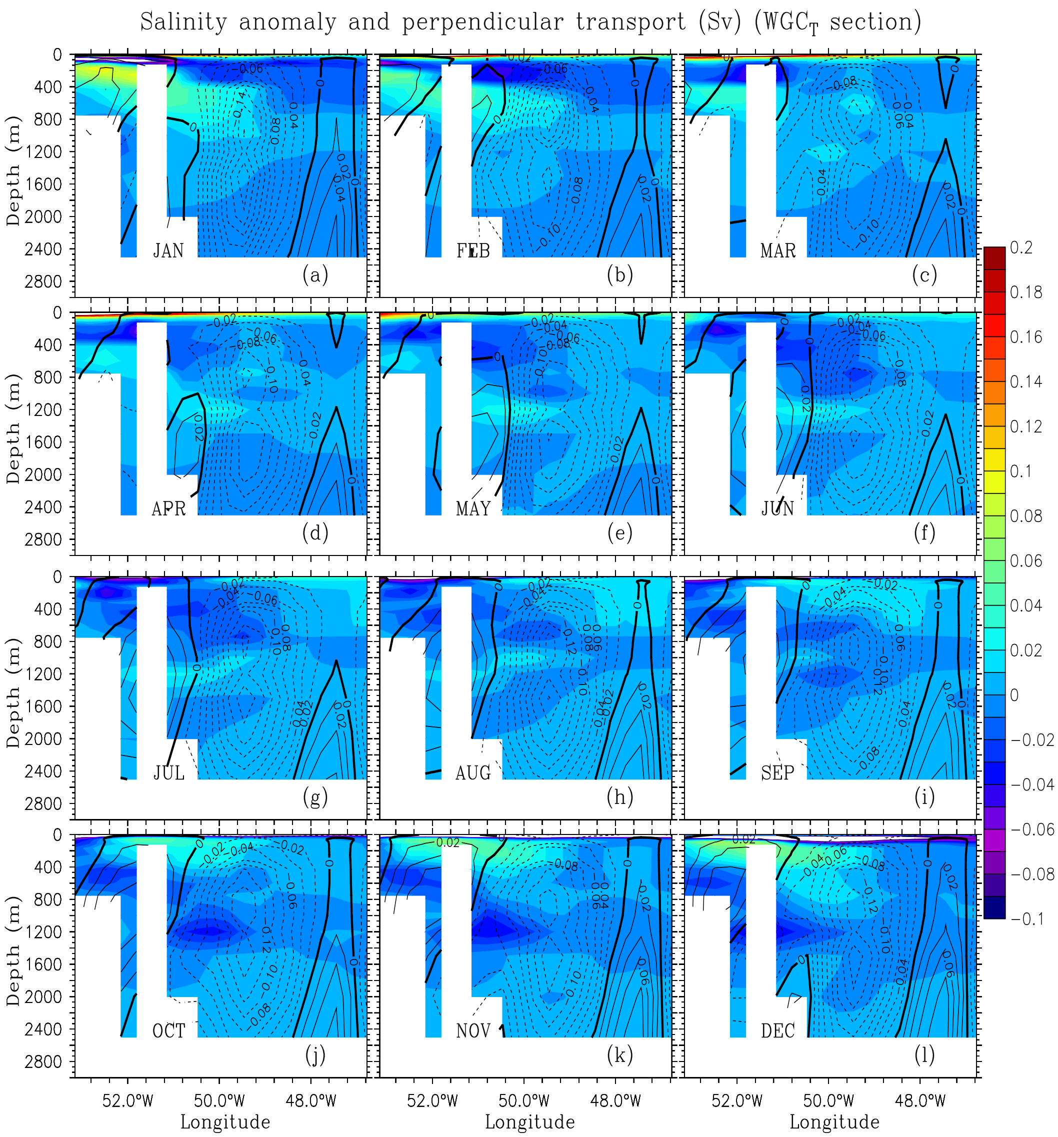

Figure 4.30: 10^{th} year Salinity anomaly and perpendicular transport (Sv) from the GM_{vis} experiment for the WGC_T section. Solid contour shows onshore (positive) and dotted offshore (negative) flow velocities

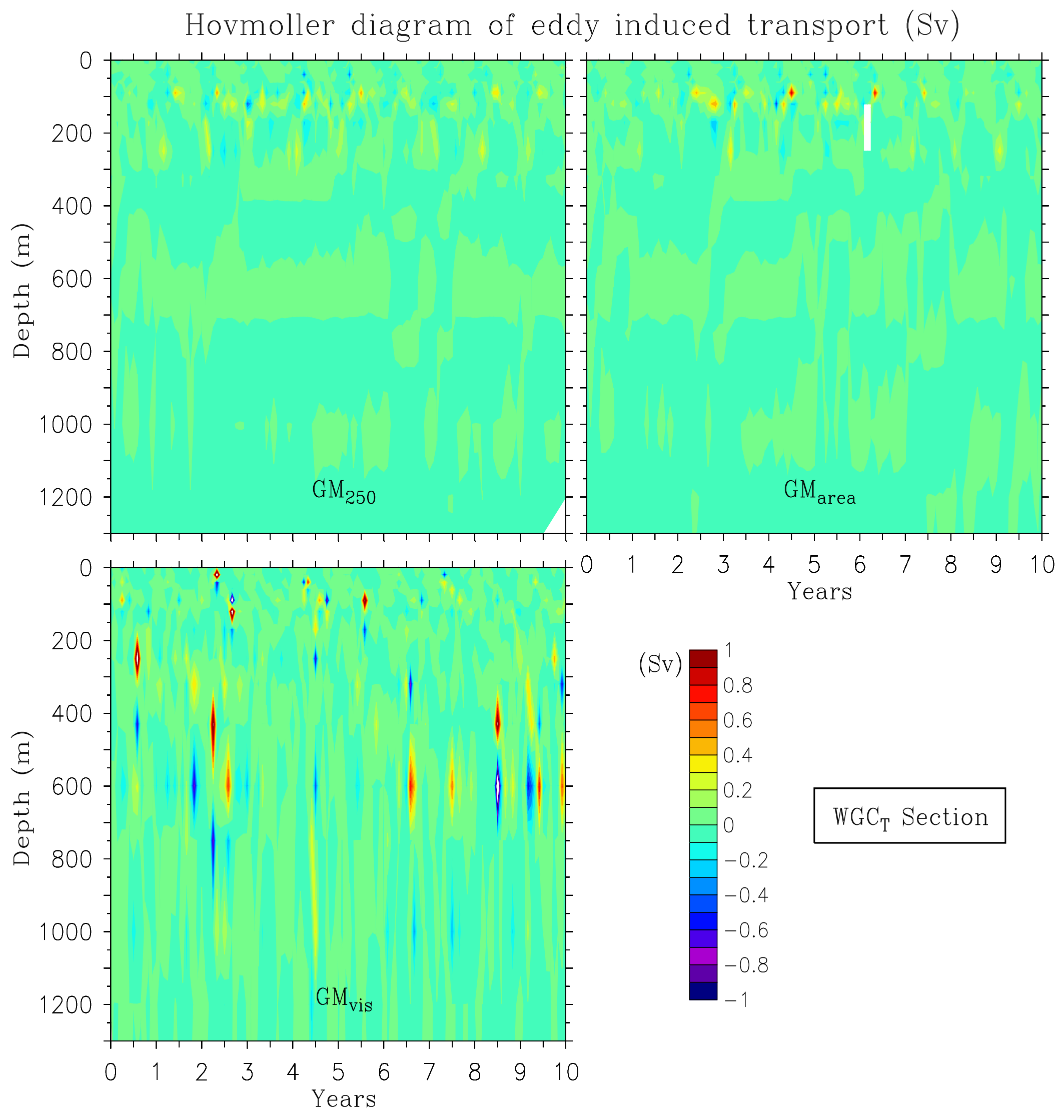

Figure 4.31: Hovmoller diagram of total eddy transport across the WGC_T section for GM_{250}, GM_{area} and GM_{vis} experiments

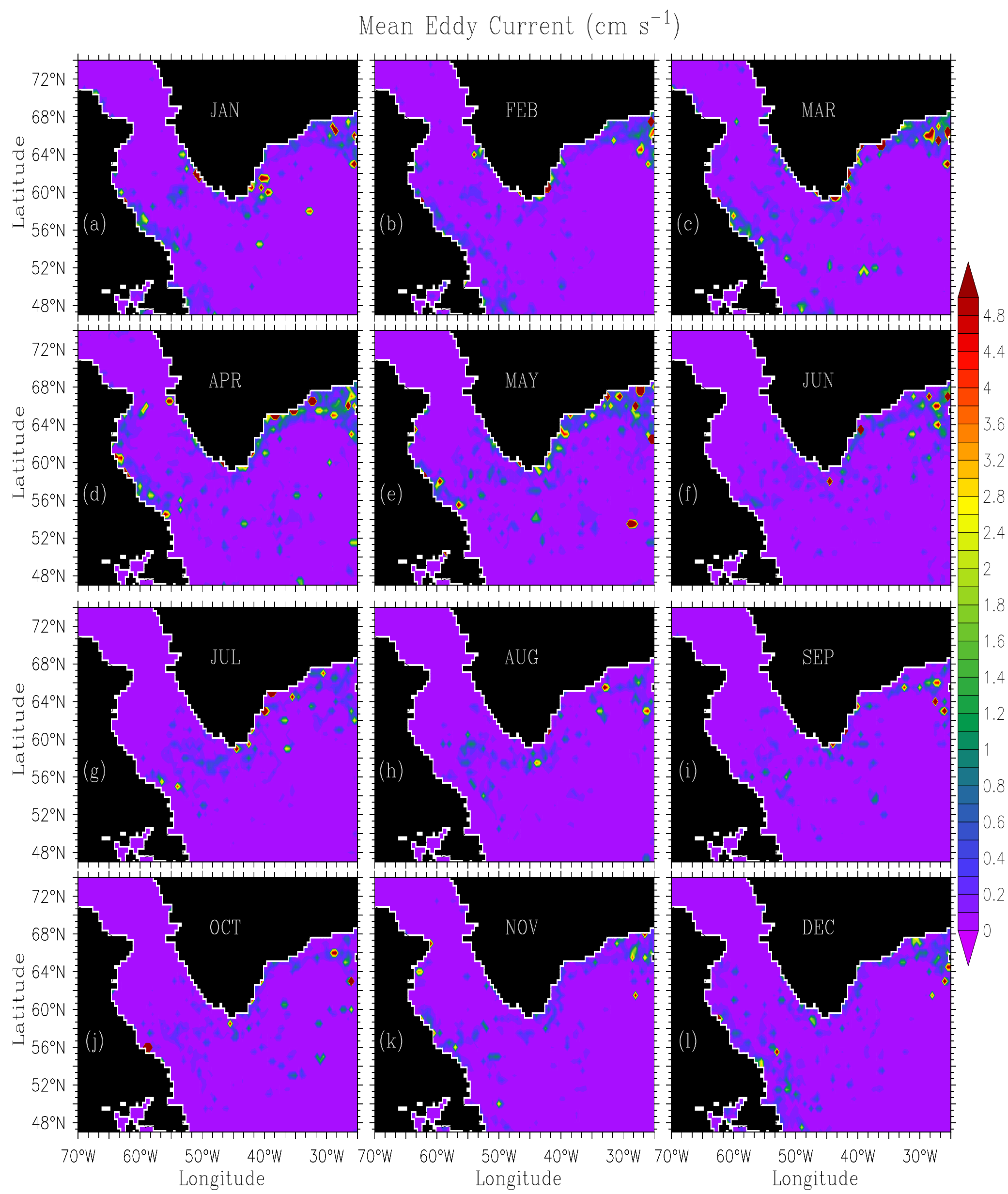

Figure 4.32: Mean monthly eddy velocity from the 15^{th} model year of GM_{vis} experiment

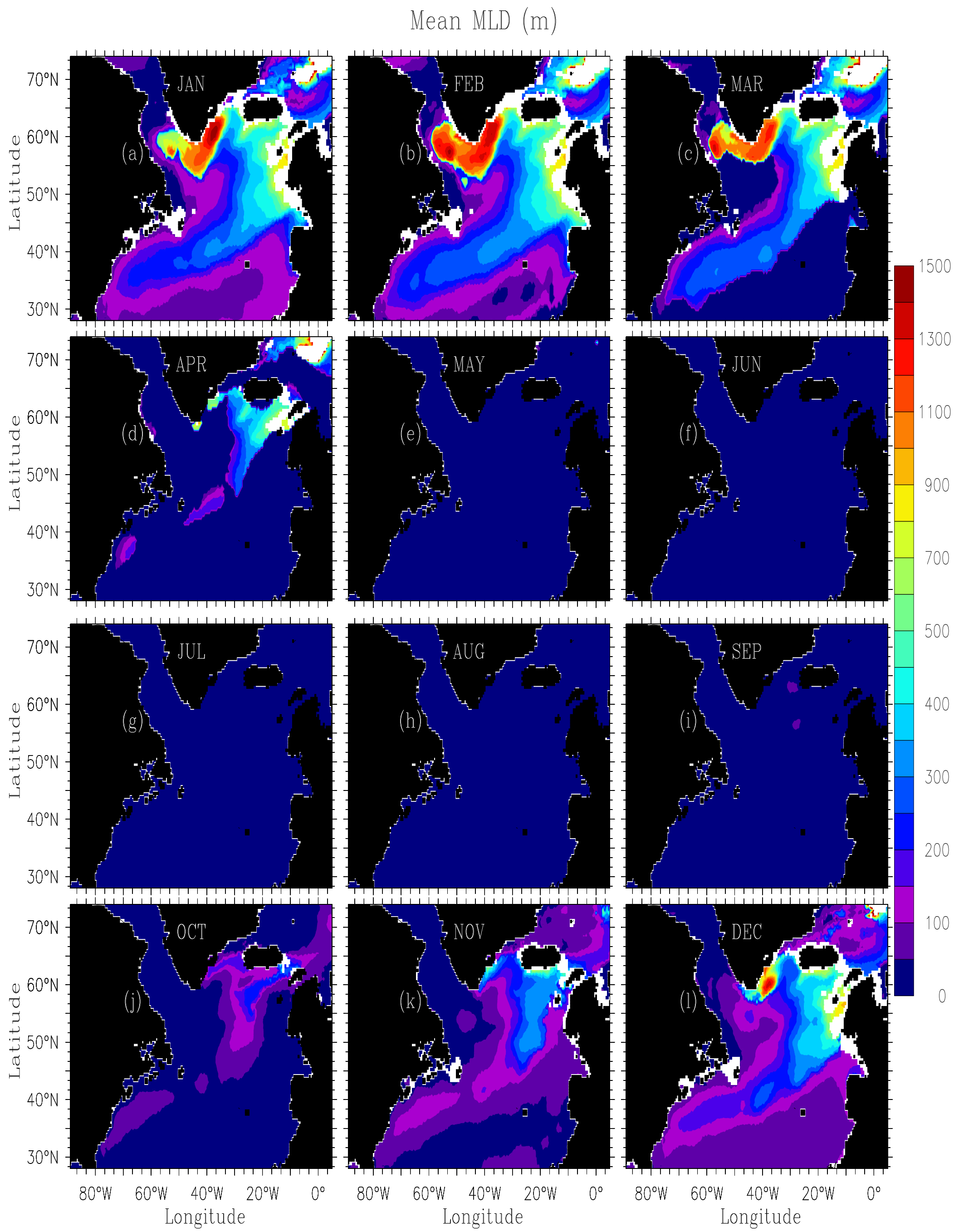

Figure 4.33: Mean monthly mixed layer depth (MLD) in meters from the 15^{th} model year of the GM_{vis} experiment

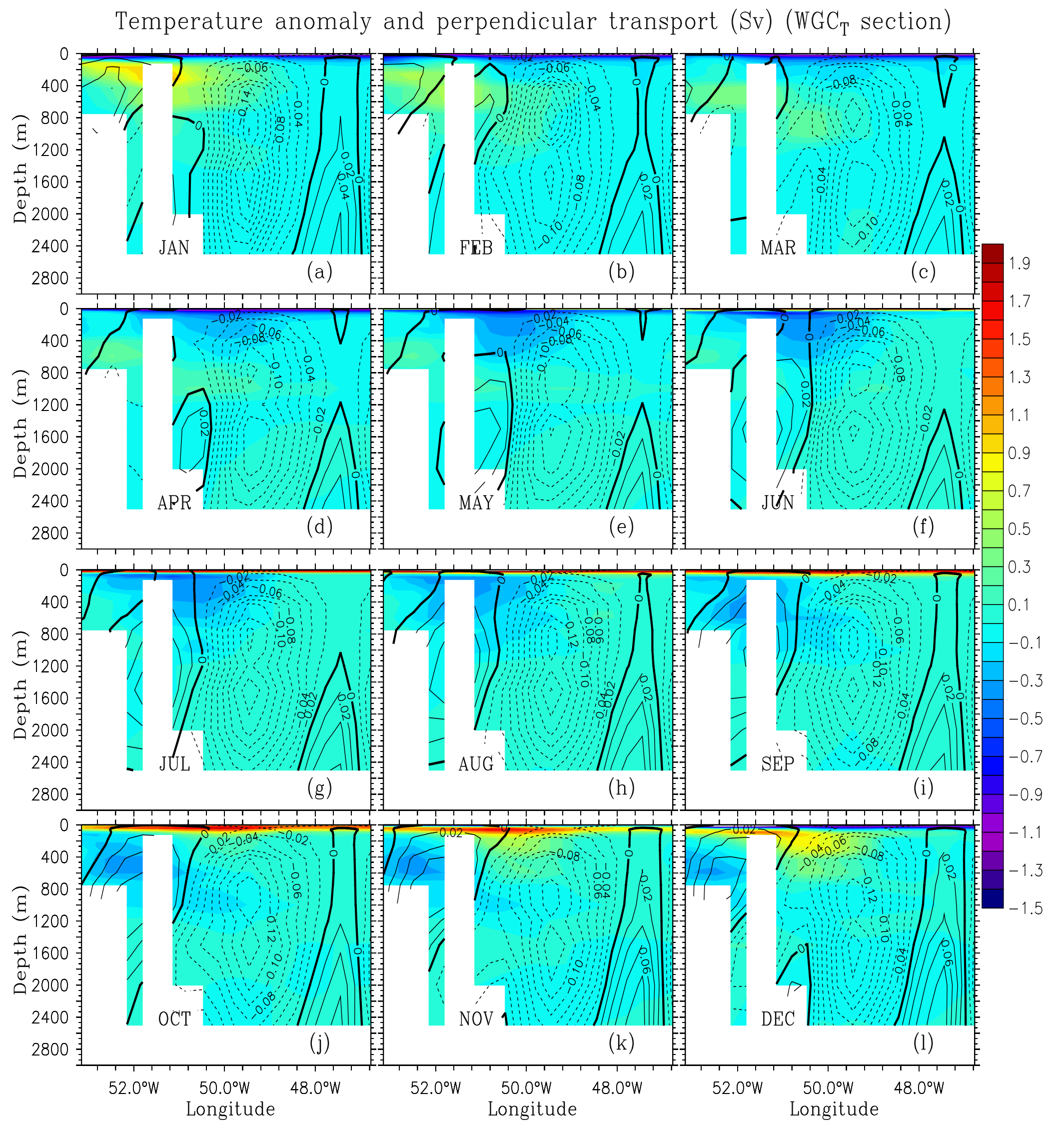

Figure 4.34: 10^{th} year Temperature anomaly and perpendicular transport (Sv) from the GM_{vis} experiment for the WGC_T section. Solid contour shows onshore (positive) and dotted offshore (negative) flow velocities

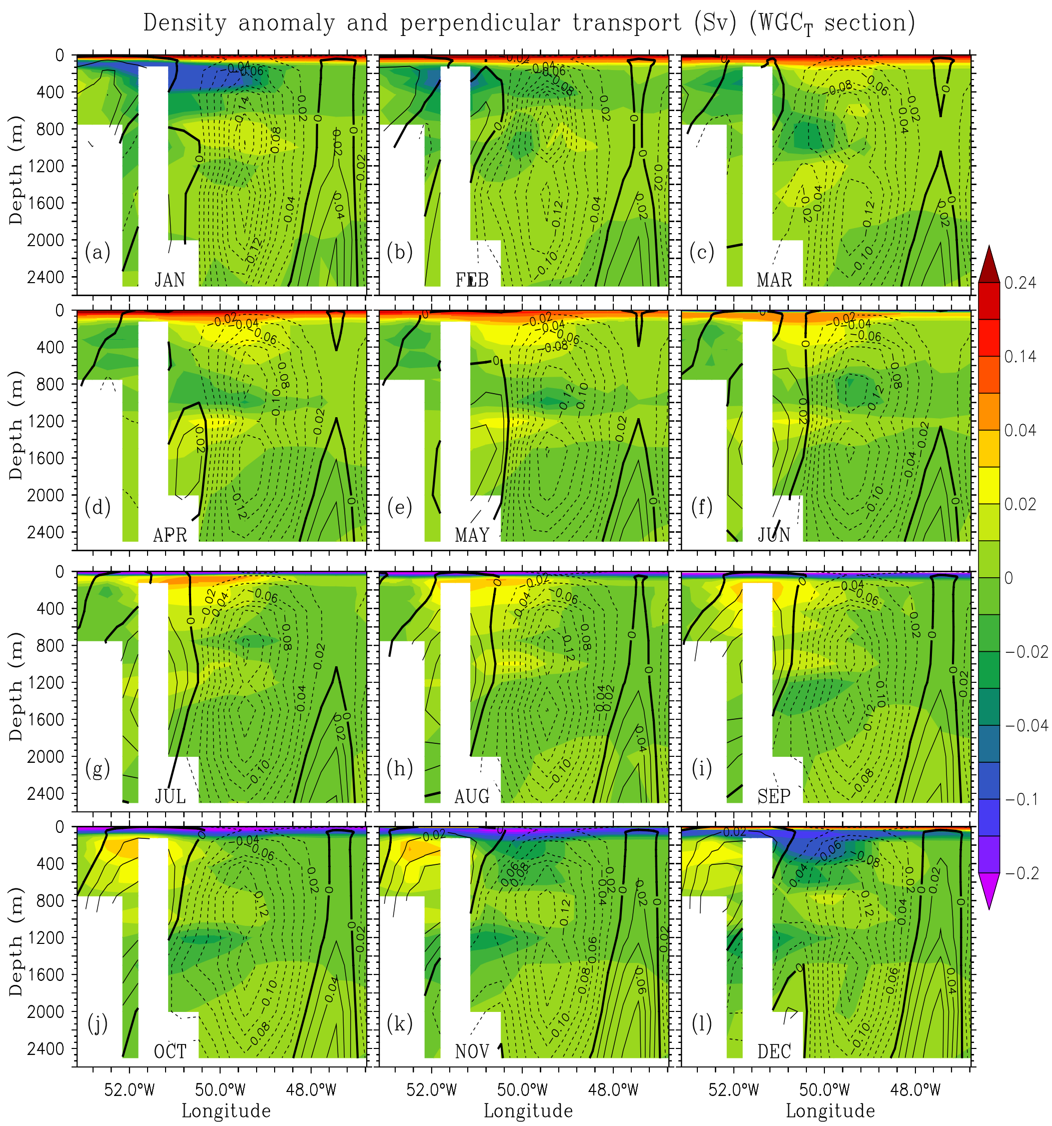

Figure 4.35: 10^{th} year density anomaly and perpendicular transport (Sv) from the GM_{vis} experiment for the WGC_T section. Solid contour shows onshore (positive) and dotted offshore (negative) flow velocities

Bibliography

Beismann, J.O. and Bernard Barnier (2004). Variability of the meridional overturning circulation of the North Atlantic: sensitivity to overflows of dense water masses. *Ocean Dynamics* **54**, 92–106.

Bracco, Annalisa and Joseph Pedlosky (2003). Vortex Generation by Topography in Locally Unstable Baroclinic Flows. *Journal of Physical Oceanography* **33**, 207–219.

Cuny, Jerome, Peter B. Rhines, Pearn P. Niller and Sheldon Bacon (2002). Labrador Sea boundary currents and the fate of the Irminger Sea Water. *J. of Phys.Ocean* **32**, 627–647.

Deacu, Daniel and Paul G. Myers (2005). Effect of a Variable Eddy Transfer Coefficient in an Eddy-Permitting Model of the Subpolar North Atlantic Ocean. *Journal of Physical Oceanography* **35**, 289–307.

Eden, Carsten and Claus Boning (2002). Sources of Eddy Kinetic Energy in the Labrador Sea. *Journal of Physical Oceanography* **32**, 3346–3363.

Eden, Carsten, Markus Jochum and Gokhan Danabasoglu (2009). Effects of different closures for thickness diffusivity. *Ocean Modelling* **26**, 47–59.

Gascard, Jean-Claude (1991). Open Ocean convection and deep water formation revisited in the Mediterranean, Labrador, Greenland and Weddell Seas. In: *Deep convection and deep water formation in the Oceans* (P.C. Chu and J.C. Gascard, Ed.). pp. 157–182. Elsevier Oceanography Series.

Gent, Peter R., Jurgen Willebrand, Trevor J. Mc Dougall and James C.

McWilliams (1995). Parameterizing eddy-induced tracer transports in ocean circulation models. *Journal of Physical Oceanography* **25**, 463–474.

Haidvogel, Dale B. and Aike Beckmann (2000). *Numerical Ocean Circulation Modeling*. Imperial College Press.

Jones, Helen and John Marshall (1997). Restratification after Deep Convection. *Journal of Physical Oceanography* **27**, 2276–2287.

Katsman, Caroline A., Michael A. Spall and Robert S. Pickart (2004). Boundary Current Eddies and Their Role in the Restratification of the Labrador Sea. *Journal of Physical Oceanography* **34**, 1967–1983.

Lazier, John (1980). Oceanographic conditions at ocean weather ship Bravo 1964-1986. *Atmosphere-Ocean* **18**, 227–238.

Lazier, John, Ross Hendry, Allyn Clarke, Igor Yashayaev and Peter B. Rhines (2002). Convection and restratification in the Labrador Sea, 1990-2000. *Deep Sea Research Part I* **49**, 1819–1835.

Lilly, Jonathan M., Peter B. Rhines, Friedrich Schott, Kara Lavender, John Lazier, Uwe Send and Eric D'Asaro (2003). Observations of the Labrador Sea eddy field. *Progress in Oceanography* **59**, 75–176.

Malone, Robert C., Richard D. Smith, Mathew E. Maltrud and Matthew W. Hecht (2003). Eddy-Resolving Ocean Modeling. *Los Alamos Science* (28), 223–231.

Myers, Paul G., Chris Donnelly and Mads H. Ribergaard (2009). Structure and Variability of the West Greenland Current in Summer derived from 6 repeat standard sections. *Progress in Oceanography* **80**, 93–112.

Prater, Mark D. (2002). Eddies in the Labrador Sea as Observed by Profiling RAFOS Floats and Remote Sensing. *Journal of Physical Oceanography* **32**, 411–427.

Schott, Friedrich A., Lothar Stramma, Benjamin S. Giese and Rainer Zantopp (2009). Labrador Sea convection and subpolar North Atlantic Deep Water export in the SODA assimilation model. *Deep-Sea Research I* **56**, 926–938.

Spall, Michael A. (2004). Boundary Currents and Watermass Transformation in Marginal Seas. *Journal of Physical Oceanography* **34**, 1197–1213.

Steffen, Elizabeth L. and Eric A. D'Asaro (2002). Deep Convection in the Labrador Sea as Observed by Lagrangian Floats. *Journal of Physical Oceanography* **32**, 475–492.

Straneo, Fiammetta (2006*a*). Heat and Freshwater Transport through the Central Labrador Sea. *Journal of Physical Oceanography* **36**, 606–628.

Straneo, Fiammetta (2006*b*). On the connection between dense water formation, overturning and poleward heat transport in a convective basin. *Journal of Physical Oceanography* **36**, 1822–1840.

Visbeck, Martin, John Marshall and Tom Haine (1997). Specification of eddy transfer coefficients in coarse-Resolution ocean circulation Models. *Journal of Physical Oceanography* **27**, 381–402.

Wright, David K. (1997). In: *A New Eddy Mixing parameterization and Ocean General Circulation Model*. pp. 27–29. Number 26. WOCE International Project Office, Southampton Oceanography Centre, UK.

Chapter 5

Conclusion and Future Work

This thesis presents a modified Finite Element Ocean Model (FEOM) for the North Atlantic Ocean. The model was successful in reproducing many features of the hydrography of the North Atlantic Ocean. This is achieved by the following additions to the model configuration.

1. Addition of a corrected heat flux as a surface boundary condition.
2. Sponge layer as an open boundary condition.
3. River flux input as a freshwater point source.
4. Tuned vertical mixing for inducing convection in the model.
5. Variable horizontal viscosity and diffusion coefficients based on mesh size, to adopt the variations in mesh resolution.
6. Spatially and temporally varying thickness diffusion coefficient (K_{gm}) for the GM parameterization based on Visbeck *et al.* (1997) and Eden *et al.* (2009).

Even though the addition of surface fluxes brought more inconsistencies into the model compared to that of the CS simulation, these were reduced to some extent by incorporating a correction to the surface net-heat flux and freshwater input flux from major rivers of the North Atlantic Ocean. However the model continued to drift in freshwater content in the Labrador Sea interior and thus led to weak Labrador Sea convection. The reason for this drift is found to be the weak exchange of tracer properties from the boundary currents, as found in the detailed boundary current analysis.

In order to represent the effects of these boundary currents and the eddies originating from them, the model is further modified to represent the unresolved sub-grid scale eddies by incorporating a modified GM parameterization scheme (Gent and McWilliams, 1990). The model is further used to study the effects of selecting various approaches for the thickness diffusion (K_{gm}) in this parameterization scheme.

The GM incorporated simulations with both spatially and temporally varying K_{gm} were able to produce a stable as well as reasonable freshwater content and convection in the Labrador Sea. Whereas this was weak when a constant and a spatially varying (K_{gm}) values were used. The simulation produced a reasonable MOC and currents for the North Atlantic Ocean with less drift in tracer properties around Gulf Stream region compared to all the flux incorporated simulations.

Even though the boundary currents in both GM_{250} and GM_{area} experiments are stronger compared to all the previous simulations, the perpendicular transport into the Labrador Sea interior was still weak leading to the continuation of the drift in the Labrador Sea interior freshwater content. This result is obtained from an analysis of the WGC system, that shows increased transport from the southern section (WGC_S) exiting through its northern section (WGC_N) without exchanging into the interior of the Labrador Sea. This weakness was resolved in the GM_{vis} experiment, where the transport into the interior became stronger irrespective of the weak transport from the southern section of WGC as detailed in Table-4.1. The freshwater content in the CFS simulation catches up with the GM_{vis} towards the 15^{th} model year (Figure-4.6). However the GM_{vis} experiment was able to contain the freshwater content through the experiment, thus producing a more stable and reliable result.

The tracer properties of the WGC closely affect the Labrador Sea interior properties and thus affect the various phases of convection, restratification and preconditioning in the Labrador Sea (Figure-4.15.d). The seasonal eddies of the WGC system reaching from 200 to 800m, also in turn played a crucial role in exchanging freshwater across the boundary current into the Labrador Sea interior and thus reducing the model's freshwater content drift. The better representation of baroclinicity in the GM_{vis} experiment were able to simulate these eddies in the model (Figure-4.31).

Winter months (December to April) are found to have more eddy activity concentrated along the coastal boundary of Greenland, whereas in summer and late summer months (April to August) they are mostly found as offshore Irminger Current eddies. This process is important in maintaining the convection depth and restratification in the Labrador Sea interior as noted in the model MLDs (Figure-4.33).

A few previous idealized basin scale studies were able to show the importance of the boundary currents and their associated seasonal eddies in setting the convection depth of the basin interior (Spall, 2004; Katsman *et al.*, 2004; Straneo, 2006). The present thesis was able to show the distinctive role of each boundary current (WGC, LC and EGC) of the subpolar gyre in setting the convection depth of the Labrador Sea interior using a more realistic ocean model. The seasonality of these eddies and the role of boundary current transports in maintaining the phases of preconditioning, convection and restratification in the Labrador Sea interior were also presented.

Overall the simulations were successful in presenting a realistic North Atlantic Ocean Model to the Ocean modelling community. The model was also successfully used to study the boundary currents and convection in the Labrador Sea.

Future applications of this model to the subpolar gyre could include the use of this model to study convection in the Irminger Sea (Pickart *et al.*, 2003), western boundary currents, deep overflow waters etc.. However a better horizontal mixing scheme (eg: biharmonic mixing) and a vertical mixing scheme (eg: K-profile parameterization) could reduce the enhanced diffusive behavior of the tracers in the Gulf Stream region. A better topography treatment (eg: partial cell, shaved cell etc..) could also improve the representation of the overflow waters in the model. The model still needs to be used for seasonal and inter-annual forcing scenarios, which can then be extended to prognostic simulations of future climate scenarios. Since the subpolar gyre of the North Atlantic Ocean includes sea ice, a coupling of the present ocean model to a sea ice model is necessary to represent the processes that can impact the ocean climate of future scenarios, which are beyond the scope of this thesis.

Bibliography

Eden, Carsten, Markus Jochum and Gokhan Danabasoglu (2009). Effects of different closures for thickness diffusivity. *Ocean Modelling* **26**, 47–59.

Gent, Peter R. and James C. McWilliams (1990). Isopycnal Mixing in Ocean Circulation Models. *Journal of Physical Oceanography* **20**, 150–155.

Katsman, Caroline A., Michael A. Spall and Robert S. Pickart (2004). Boundary Current Eddies and Their Role in the Restratification of the Labrador Sea. *Journal of Physical Oceanography* **34**, 1967–1983.

Pickart, Robert S., Michael A. Spall, Mads Hvid Ribergaard, G.W.K. Moore and Ralph F. Milliff (2003). Deep convection in the Irminger Sea forced by the Greenland tip jet. *Nature* **424**, 152–156.

Spall, Michael A. (2004). Boundary Currents and Watermass Transformation in Marginal Seas. *Journal of Physical Oceanography* **34**, 1197–1213.

Straneo, Fiammetta (2006). Heat and Freshwater Transport through the Central Labrador Sea. *Journal of Physical Oceanography* **36**, 606–628.

Visbeck, Martin, John Marshall and Tom Haine (1997). Specification of eddy transfer coefficients in coarse-Resolution ocean circulation Models. *Journal of Physical Oceanography* **27**, 381–402.

Appendix

The Hydrostatic approximation

Since vertical velocities in the ocean are very small, we can neglect the vertical acceleration, centrifugal acceleration and the Coriolis acceleration in the vertical momentum equation. These approximations lead to equation-2.3.

$$\partial_z p = -g\rho$$

The Boussinesq approximation

Density variations in the ocean are $< 1\%$ compared to the mean density (ρ_0). Hence the horizontal pressure gradient force can be approximated as in equation-2.1 given by,

$$-\frac{1}{\rho_0}\nabla P$$

and the hydrostatic balance in equation-2.3 can also be written as,

$$g' = -\frac{1}{\rho_0}\frac{\partial P}{\partial z} \tag{5.1}$$

where g' is the reduced gravity given by $g' = \frac{g\rho}{\rho_0}$ and ρ is calculated by equation-2.5. The Boussinesq approximation thus neglects the terms $\frac{\rho}{\rho_0}$ except for the buoyancy term $\frac{g\rho}{\rho_0}$. This approximation introduces only a small error in the solution.

Mass conservation and Sea surface height

The complete equation for mass conservation (no source/sink) is given by,

$$D_t\rho + \rho\left(\frac{\partial u}{\partial x} + \frac{\partial v}{\partial y} + \frac{\partial w}{\partial z}\right) = 0 \tag{5.2}$$

According to fluid dynamics, any flows slower than the sound velocity can be approximated by volume conservation, leading to equation-2.4 given as,

$$\partial_z w = -\nabla_h \cdot \mathbf{u}$$

The sea surface height equation given in equation-2.2 can be obtained by integrating equation-2.4 from the ocean bottom (-H) to the free surface (ζ) as,

$$w(\zeta) - w(-H) = -\int_{z=-H}^{z=\zeta} \nabla_h \cdot \mathbf{u}\, dz \tag{5.3}$$

Applying bottom (equation-2.11) and surface ($\partial_t \zeta + \mathbf{u} \cdot \nabla_h \zeta = w$) kinematic boundary conditions gives,

$$\partial_t \zeta + \int_{z=-H}^{z=\zeta} \nabla_h \cdot \mathbf{u}\, dz = 0$$

Mixed Layer Depth (MLD) criteria

The mixed layer depth (MLD) in this study is defined as the depth where the density increase compared to the surface equals 0.02 kgm^{-3}.

The net heat flux correction adopted from Barnier *et al.*, (1995)

The net heat flux (Q_{net}) at the ocean surface can be expressed as the sum of it's four components shown below,

$$Q_{net} = \underbrace{Q_s}_{solar} + \underbrace{Q_{IR}}_{infrared} + \underbrace{Q_H}_{sensible} + \underbrace{Q_E}_{latent}$$

Assuming the ocean surface radiates as a gray body (emissivity $\epsilon = 0.98$), the above equation in bulk formulation for a climatological ocean can be written as,

$$Q_{net} = Q_s - \epsilon\sigma(T^s_{clim})^4 + \rho_a C_P C_H U_{10}(T_A - T^s_{clim}) - \rho_a C_E L U_{10}(q_s - q_a)$$

The net heat flux correction given in equation-3.3 in Chapter 3 is obtained as,

$$\frac{dQ_{net}}{dT^s_{clim}} = \frac{d(Q_s - \epsilon\sigma(T^s_{clim})^4 + \rho_a C_P C_H U_{10}(T_A - T^s_{clim}) - \rho_a C_E L U_{10}(q_s - q_a))}{dT^s_{clim}} \tag{5.4}$$

where ρ_a is the air density in kg m $^{-3}$, T_A is the air temperature at 10 m height and q_a is the specific humidity of air.

Since the solar heat flux at the ocean surface does not depend on the model SST the first term on the R.H.S of the equation-5.4 will be zero.
The second term (infrared or long wave heat flux) on the R.H.S of the equation-5.4 becomes,

$$\frac{dQ_{IR}}{dT^s_{clim}} = -4\epsilon\sigma(T^s_{clim})^3$$

The third term (sensible heat flux) on the R.H.S of the equation-5.4 becomes,

$$\frac{dQ_H}{dT^s_{clim}} = -\rho_a C_P C_H U_{10}$$

The fourth term (latent heat flux) on the R.H.S of the equation-5.4 becomes,

$$\frac{dQ_E}{dT^s_{clim}} = -\rho_a C_E L U_{10} \frac{dq_s}{dT^s_{clim}}$$

where the q_s can be expressed in terms of the water saturation vapor pressure (e_s) as,

$$q_s = \frac{0.622}{P_A} e_s$$

further utilizing the Clausius-Clapeyron equation, the e_s can be written as,

$$e_s = 10^{(9.4051 - \frac{2353}{T^s_{clim}})}$$

applying this to the equation-5.5 gives,

$$\frac{dQ_E}{dT^s_{clim}} = -\rho_a C_E L U_{10} \times 2353\, ln(10) \times \frac{q_s}{(T^s_{clim})^2}$$

Substituting these results to the equation-5.4 yields the final correction term given in Chapter 3 as given below,

$$\frac{dQ}{dT^s_{clim}} = \underbrace{-4\epsilon\sigma(T^s_{clim})^3}_{Infrared} - \underbrace{\rho_a C_P C_H U_{10}}_{Sensible} - \underbrace{\rho_a C_E L U_{10} 2353\, ln(10) \times \left(\frac{q^s_{clim}}{(T^s_{clim})^2}\right)}_{Latent}$$

Time derivative schemes

For the ease of explanation consider the following simple equation,

$$\frac{\partial u}{\partial t} = \frac{\partial^2 u}{\partial x^2}$$

Applying a centered finite difference on the equation above gives

$$\frac{u^{n+1} - u^n}{\Delta t} = \frac{u_{i-1} - 2\, u_i + u_{i+1}}{\Delta x^2} \tag{5.5}$$

then the **Explicit Scheme** is given by,

$$u^{n+1} = u^n + \Delta t \left[\frac{u_{i-1}^n - 2\, u_i^n + u_{i+1}^n}{\Delta x^2}\right]$$

the **Implicit Scheme** is given by

$$u^n = u^{n+1} - \Delta t \left[\frac{u_{i-1}^{n+1} - 2\, u_i^{n+1} + u_{i+1}^{n+1}}{\Delta x^2}\right]$$

and the **Crank-Nicolson Scheme** is given by,

$$u^n - (1-\alpha)\Delta t \left[\frac{u_{i-1}^n - 2\, u_i^n + u_{i+1}^n}{\Delta x^2}\right] = u^{n+1} - (1-\alpha)\Delta t \left[\frac{u_{i-1}^{n+1} - 2\, u_i^{n+1} + u_{i+1}^{n+1}}{\Delta x^2}\right]$$

where the choice of the parameter α transforms the expansion into fully explicit ($\alpha = 0$), fully implicit ($\alpha = 1$) and Crank-Nicolson ($\alpha = 0.5$) method.

Coordinate transformation

The coordinate transformation used in Chapter 4 to find the velocity components across the vertical sections in the subpolar gyre (Figure-4.7) is illustrated by the diagram (Figure-5.1).
The corresponding coordinate transformation formulas are given by

$$x' = x\, \cos(\theta) + y\, \sin(\theta) \tag{5.6}$$

$$y' = -x\, \sin(\theta) + y\, \cos(\theta) \tag{5.7}$$

Mesh size dependent mixing and diffusion coefficients

The mesh size dependent A_h and K_h are given by the following condition corresponding to each element's area (Δ) and background viscosity ($Ah0 =$

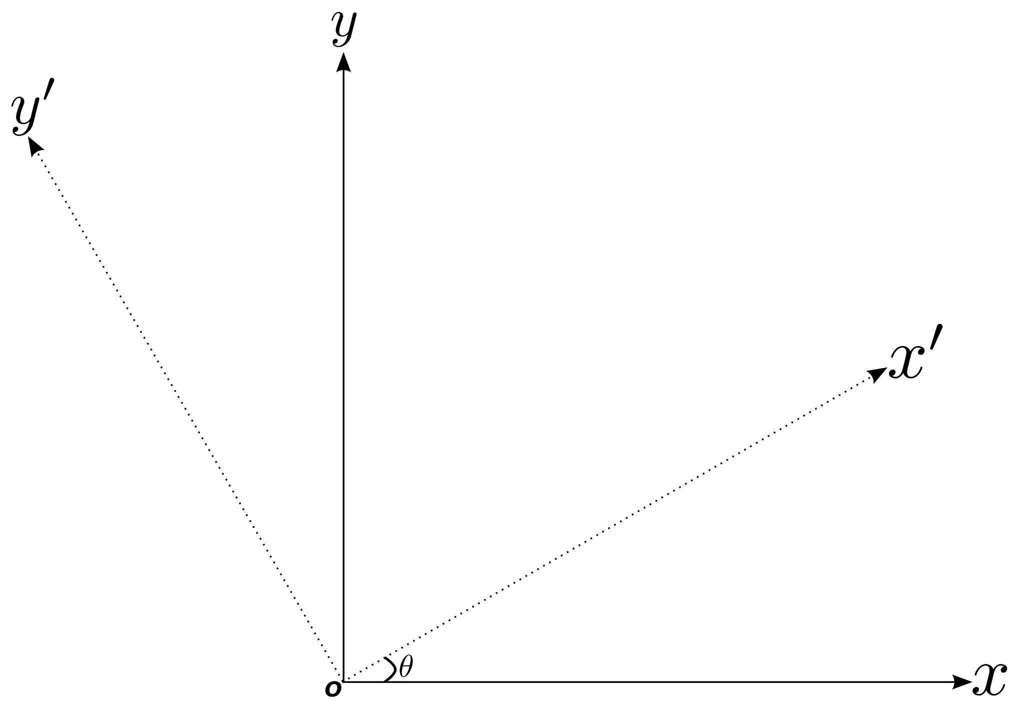

Figure 5.1: Mapping of $x - y$ coordinates to a new axis $x' - y'$ by rotating an angle of θ around the origin O

$1000\,m^2s^{-1}$) and diffusion ($Kh0 = 500\,m^2s^{-1}$) coefficients.

$$A_h = \begin{cases} \frac{Ah0}{5} & \frac{\sqrt{2\Delta}}{1000} < 5 \\ \max\left[\frac{Ah0}{5}, \frac{Ah0 \cdot \ln(\Delta))}{\max(\ln(\Delta))}\right] & \frac{\sqrt{2\Delta}}{1000} > 20 \\ \frac{Ah0}{5} & \text{otherwise} \end{cases} \tag{5.8}$$

Here $\frac{\sqrt{2\Delta}}{1000}$ gives an approximate resolution of the mesh in kilometers. A similar condition is also applied to K_h by replacing $Ah0$ with $Kh0$ in the above formula.

The GM_{area} experiment used half of Ah as the value of K_{gm} transforming it to a spatially varying, mesh size dependent thickness value.